# Block copolymer template-directed novel functional particles: synthesis, properties and applications

D i s s e r t a t i o n

zur Erlangung des akademischen Grades

d o c t o r  r e r u m  n a t u r a l i u m

(Dr. rer. nat.)

im Fach Chemie

eingereicht an der

Mathematisch-Naturwissenschaftlichen Fakultät

der Humboldt-Universität zu Berlin

von

**M. Sc. Shilin Mei**

Präsident der Humboldt-Universität zu Berlin
Prof. Dr.-Ing. Dr. Sabine Kunst

Dekan: der Mathematisch-Naturwissenschftlichen Fakultät
Prof. Dr. Elmar Kulke

Gutachter: 1. Prof. Dr. Matthias Ballauff

2. Prof. Dr. Nicola Pinna

Tag der mündlichen Prüfung: 25-04-2017

*A book is the same today as it always was and it will never change.*

*To My Family & Friends*

# Abstract

The present thesis focuses on the synthesis of novel functional materials by using block copolymer particles as soft templates. Three types of particles with complex structures have been synthesized, involving palladium@poly(styrene-*b*-2-vinylpyridine)@dodecanethiol-gold (DT-Au) (Pd@PS-P2VP@DT-Au) hybrid particles, polydopamine@gold (PDA@Au) nanoreactors with Au nanoparticles immobilized in PDA channels, and porous $Ti_4O_7$ particles with interconnected-pore structure. Their possible applications as catalyst and energy storage materials have been studied.

In the first part of the thesis, Pd@PS-P2VP@DT-Au core-shell particles, which consist of dodecanethiol-gold (DT-Au) aggregation as core and Pd coated PS-P2VP as shell, have been fabricated based on the Rayleigh instability of polymer nanotubes inside Anodic Aluminium Oxide (AAO) porous membranes. The hybrid particles show efficient catalytic activity for the reduction of 4-nitrophenol by $NaBH_4$. The catalytic activity has been compared with other reported systems.

In the second part, PDA@Au nanoreactors with interconnected channel structures have been synthesized for the first time by using porous PS-P2VP particles as soft template. Electron tomography (ET) provides direct visualization of the interconnected pore structure of the nanoreactors, inside of which Au nanoparticles are homogeneously embedded. Such PDA@Au particles have been explored as nanoreactors for kinetic studies using the reduction of 4-nitrophenol as the model reaction.

In the third part, porous $Ti_4O_7$ and carbon-coated $Ti_4O_7$ particles with interconnected-pore structure have been developed as efficient sulfur-host material for lithium-sulfur batteries by using porous PS-P2VP particles as template. The $Ti_4O_7$/S and carbon-coated $Ti_4O_7$/S composites show excellent electrochemical performance with initial capacities of 1219 mAh $g^{-1}$ and 1411 mAh $g^{-1}$, capacity retentions of 74% and 77% after 200 cycles, respectively.



Keywords: block copolymer, PS-P2VP, metal nanoparticles, polydopamine, catalyst, $Ti_4O_7$, lithium-sulfur batteries

# Zusammenfassung

Gegenstand dieser Arbeit ist die Synthese neuer funktioneller Materialien unter Zuhilfenahme von Blockcopolymerpartikeln als „soft templates“ und die Untersuchung ihrer Anwendungsmöglichkeiten als Katalysator- und Energiespeichermaterialien. Drei Arten von Kompositpartikeln mit komplexen Strukturen wurden synthetisiert: Palladium@poly(styrol-b-2-vinylpyridin)@Dodecanthiol-Gold (Pd@PS-P2VP@DT-Au) Hybridpartikel, Polydopamin@Gold (PDA@Au) Nanoreaktoren und poröse $Ti_4O_7$ Partikel mit verbundener Porenstruktur.

Im ersten Teil der Arbeit wurden Pd@PS-P2VP@Au Kern-Schale Partikel, bestehend aus DT-Au Aggregaten als Kern, umgeben von mit Palladium Nanopartikeln beschichtetem PS-P2VP als Schale hergestellt. Die auf die strukturierte P2VP Schale aufgebrachten Palladium Nanopartikel weisen im Vergleich mit anderen bekannten Systemen gute katalytische Eigenschaften für die Reduktion von 4-Nitrophenol mit $NaBH_4$ auf.

Im zweiten Teil wurden zum ersten Mal PDA@Au Nanoreaktoren mit verbundener Porenstruktur unter Verwendung einer „soft template“-Methode synthetisiert. Dabei wurden poröse PS-P2VP Partikel als Template verwendet. Mittels Elektronentomografie (ET) konnte die verbundene Porenstruktur mit den darin gleichmäßig verteilten Gold Nanopartikeln direkt abgebildet werden. Die PDA@Au Partikel wurden mithilfe der katalytischen Reduktion von 4-Nitrophenol kinetisch untersucht.

Im dritten Teil wurden poröse $Ti_4O_7$ Partikel mit verbundener Porenstruktur als neuer Typ von Schwefel Wirtsmaterial für Lithium-Schwefel Batterien unter Zuhilfenahme von porösen PS-P2VP Templatpartikeln entwickelt. Die elektrochemische Untersuchung von $Ti_4O_7$/S und kohlenstoffbeschichtetem $Ti_4O_7$/S beim Einsatz als Kathodenmaterial ergab hervorragende Leistungsdaten von 1219 $mAhg^{-1}$ bzw. 1411 $mAhg^{-1}$ für die Anfangskapazität und eine Kapazitätserhaltung von 74% bzw. 77% nach 200 Zyklen.

Stichwörter: Blockcopolymer, PS-P2VP, Metallnanopartikel, Polydopamin, Katalysator, $Ti_4O_7$, Lithium-Schwefel Batterien

## Table of Contents

# 1. Introduction

Nanomaterials with highly ordered or porous structures are of great interest in a broad range of applications including gas storage and separation materials, encapsulation agents for controlled release of drugs, catalysts, energy storage and sensors.[1] The formation of these complex structures usually relies on the availability of templates, which traditionally involve hard templates and soft templates.[2, 3] Hard templates are usually solid-state materials with particular structure and morphology. They were popular because of the precise control over size and shape of the resulting materials. However, the removal of hard templates requires harsh conditions, not only complicating the synthesis process, but also causing damage to the degradable materials, which prevent them from further development. On the contrary, soft templates generally consisting of various polymers or surfactants are much easier to be removed by means of simple extraction or evaporation. But the precise control on the morphology of the target product is hard to achieve by using traditional soft templates. Therefore, combining the advantages of traditional hard templates and soft templates is of great importance for the development of novel functional materials.

Recent advances in this area have demonstrated that block copolymer (BCP) assemblies can fulfill this need, because they can yield ordered structures in a wide range of morphologies.[4, 5] Moreover, they are soluble in many organic solvents and can be removed easily by dissolving. Thus, block copolymer assemblies become promising templates which can realize the precise control on morphology together with the ease of removing. Current studies using block copolymer as template to synthesize advanced materials mainly focus on two directions. One is the assembly of metal/metal oxide nanoparticles into ordered patterns. For example, Jin et al.[6] reported the patterned decoration of gold nanoparticles on the surface of poly(styrene-2-vinylpyridine) (PS-P2VP) particles using in situ reduction of $HAuCl_4$ in P2VP domains under UV irradiation. However, most works of this sort focus on the assembly of one type of metal nanoparticles.[7-9] No experiment has been conducted on the assembly of two different types of metal nanoparticles to BCP particles with ordered spatial distribution. Integrating specific properties from different materials usually is a practical way to maximize the functionality of the resulted materials. Thus the assembly of different types of metal nanoparticles onto block copolymer nanostructures becomes a subject of great significance.

Another direction is creating porous structures through selective etching or selective swelling of the block copolymer materials.[10, 11] Block copolymers with one chemically active component have been demonstrated to be promising precursors for the generation of ordered porous structures. For example, Wang et al.[9, 10] have studied the swelling-induced pore generation of PS-P2VP or PS-P4VP materials since 2010, they have investigated the porous structures from bulk materials to nanofibers and nanorods. Jin et al.[12] extended the porous structures to nanospheres. The corresponding applications have been demonstrated on membrane separation, antireflective coating and drug loading.[13, 14] However, the potential application as template for the formation of complex structures has not been extensively studied. Only a few reports present their attempts at exploring the porous bulk materials as templates for functional replicas. No reports have been found about the templating role of the porous particles, whereas nanoparticles with complex inner structures together with designed functional components are of great importance to develop advanced materials. Considering the nondestructive nature of the swelling strategy, the obtained porous particles provide possibilities for the synthesis of a new class of functional replicas with complex inner structures.

Therefore, the present thesis focuses on the synthesis of novel functional materials by using block copolymer nanoparticles and their porous structures as templates. Three works are presented including spatial assembly of two types of metal nanoparticles onto block copolymer nanospheres, synthesis of polydopamine@gold (PDA@Au) nanoreactors, and synthesis of porous Magnéli phase titanium sub-oxides ($Ti_4O_7$) nanoparticles. Their possible applications as catalyst and energy storing materials will be discussed in the following chapters.

## 1.1 Self-assembly of block copolymers (BCPs)

Block copolymers are molecules composed of different blocks covalently connected into one macromolecule. Minimization of free energy during microphase separation can lead to the formation of various thermodynamically-stable structures on nanometer scale.[4] With the advent of anionic polymerization, which permits the synthesis of model block copolymers with narrow molecular weight distribution, microphase separation structures of block copolymers containing amorphous blocks have been explored extensively.[15, 16] Generally, in

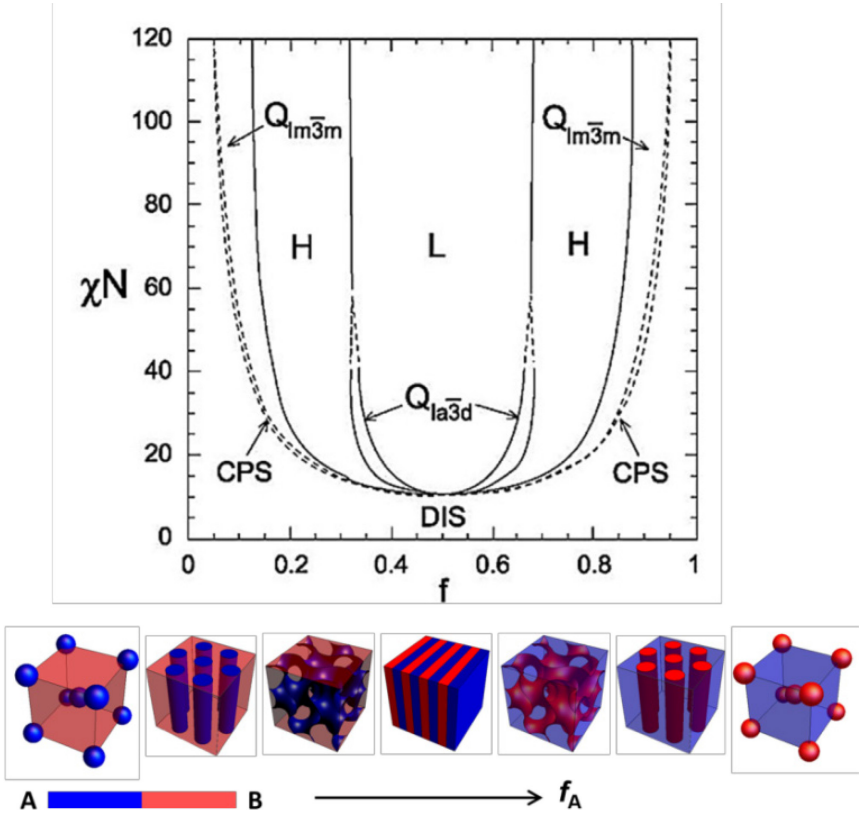


**Figure 1.1.1** Mean-field phase diagram for model diblock copolymers.[4] Phase are labeled L (lamellar), H (hexagonal cylinders), Qla3d (bicontinuous cubic gyroid), Qlm3m (BCC spheres), CPS (close-packed spheres), and DIS (homogeneous). $\chi$ : Flory-Huggins interaction parameter; $N$: the total chain length (or molecular weight); $f$ : the volume fraction of one block (for diblock copolymers, $f_A + f_B = 1$). When $\chi N$ is small, the system is homogeneous, microphase separation does not take place. If $\chi N$ is large (≥10), the system spontaneously undergoes microphase separation. The final structure is determined by $f$. Systems with approximately equal lengths of 'dislike' blocks ($f_A$=0.5) form lamellae, while highly asymmetric systems (very small $f_A$) form BCC spheres, with the short block comprising the discrete phase. Cylinders and gyroid structures form between spheres and lamellae. The characteristic spacing is determined by $N$.

bulk, block copolymers with immiscible blocks can microphase separate as a function of composition into a variety of morphologies: body-centered cubic (BCC) array of spherical domains, hexagonally packed cylinders, bicontinuous gyroid and an alternating lamellar morphology (Figure 1.1.1).[4, 17] Because these structures are resulted from block copolymer microphase separation, they are generally called microdomains. The self-assembly process is driven by an unfavorable mixing enthalpy coupled with small mixing entropy, with the covalent bond connecting the blocks preventing macroscopic phase separation.

Different from bulk materials, the microphase separation patterns of block copolymer nanoparticles are strongly affected by the spherical geometry. The spherical confinement

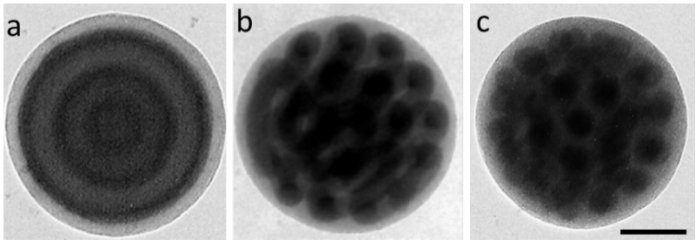


**Figure 1.1.2** TEM images of PS-PB particles with different ordered structures. (a) onion-like microphase separation structure; (b) helices structure; (c) packed spheres structure.[18]

differs from that in bulk where the principal curvature is zero. It is a three-dimensional (3D) confinement. Under the efforts of curvature, commensuration (the size of the nanospheres is integral multiple of the microdomains) and surface properties, the microphase patterns are forced to conform the geometry of the nanospheres. There are many theoretical and experimental works investigating block copolymer nanospheres with ordered structures.[19-23] Yang's group[18] has systematically studied the microphase separation structures of polystyrene-*b*-polybutadiene (PS-PB) particles with the volume fraction of PS ($f_{PS}$) for three different values. They observed that with the decrease of $f_{PS}$ from 0.4 to 0.21 and 0.04, the microdomains of lamellae, cylinders, and spheres were structured in concentric arrangements due to the spherical confinement of the particles. The generated nanostructures changed from onion-like to helices and finally packed spheres structure (Figure 1.1.2).

Apart from the dominating role of the volume fraction of the blocks, other experimental factors such as preparing method, preparing temperature and the size of spherical confinement also have great impact on the nanstructure of block copolymer particles. For example, Yabu et al.[24] studied the nanostructures of symmetrical polystyrene-*b*-polyisoprene (PS-PI) particles prepared using the self-organized precipitation method at various temperatures from 10 to 40 ˚C. They observed different microphase separation structures in the nanoparticles, including disordered, stacked lamellar and onion-like structures depending on their preparation temperature (Figure 1.1.3). Besides, the size of the spherical confinement also has influence

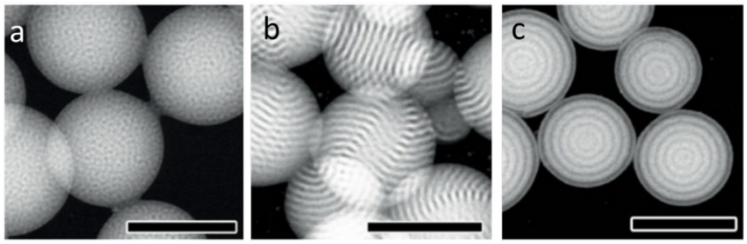


**Figure 1.1.3** STEM images (dark field) of PS-PI nanoparticles prepared at (a) 10 ˚C, (b) 25 ˚C, and (c) 40 ˚C. Scale bars indicate 300 nm. (PS-PI: $M_n$(PS) = 17800 g/mol, $M_n$(PI) = 12000 g/mol, $f_{PI}$ = 0.43).[24]

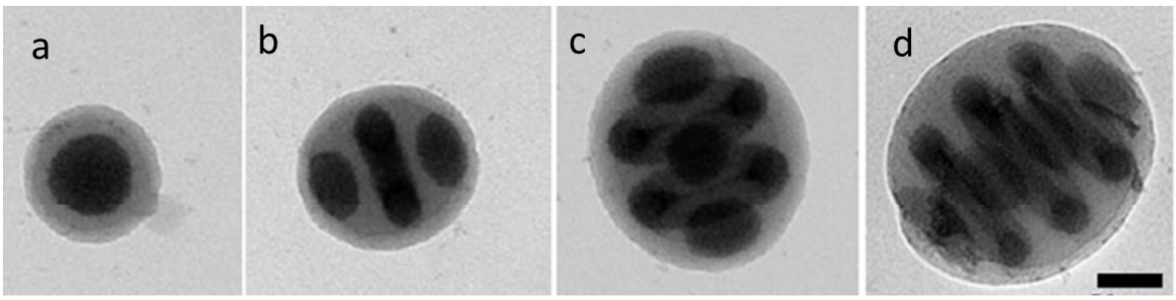


**Figure 1.1.4** TEM images (dark field) of PS-PB nanoparticles with different sizes of spherical confinement. The confinement is calculated as $D/L_0$. ($D$: diameter of the particles; $L_0$: the feature spacing of the phase-separated periodic domains) (a) $D/L_0 = 2.0$; (b) $D/L_0 = 2.5$; (c) $D/L_0 = 3.3$; (d) $D/L_0 = 4.0$. Scale bars indicate 50 nm.[18]

on the morphology of the block copolymer particles. As demonstrated by Yang et al.,[18] a small volume of the particles usually contains a few individual microdomains. Whereas a larger volume allows for more repeated microdomains, which can form ordered structures inside the particles.

These nanostructured polymer particles are of great interest due to their possible applications in nanotechnology, for example the applications in nanolithography, fabrication of nanocontainers for drug delivery, and building of photonic crystals.[25-27] In addition, block copolymer particles can serve as template for the assembly of metal nanoparticles into ordered patterns. Particles composing of degradable or swellable components offer opportunities for the synthesis of porous structures and even more complex structures. Therefore, block copolymer nanoparticles will be promising candidates to work as templates for the synthesis of complex nanostructures.

## 1.2 Block copolymer directed assembly of metal nanoparticles

Metal nanoparticles have promising applications in various optical, electronic, and sensor devices because of the extraordinary functionalities that their bulk counterparts do not have.[28] When multiple metal nanoparticles are organized at the nanometer scale, collective phenomena can be caused by the interaction among them. This strongly relies on the morphology of the assembly including the configuration of their organization and the interparticle distance.[29] For example, depending on the polarization of light, metallic nanoparticles in a one-dimensional linear array exhibit a remarkable difference in absorption spectra owing to their anisotropic configuration.[30] Moreover, the size and spacing of the arrayed nanoparticles determine the degree of surface plasmon resonance coupling.[31] Robust and feasible techniques to arrange nanoparticles with tunable assembly have been extensively

explored in the last few years.[32, 33] One such technique is direct-write lithography, which includes electron-beam lithography [31] and dip-pen nanolithography.[32] However, conventional lithographic processes show their practical and theoretical limits and make it challenging to arrange nanoparticles with single particle precision. On the contrary, block copolymer directed self-assembly approaches provide opportunities to overcome these limitations, especially to control the inter-particle ordering precisely to tailor the coupling phenomena in nanoparticle clusters.[34]

Two major strategies have been explored to generate metal nanoparticle arrays within block copolymer microdomains: in situ synthesis of metal nanoparticles, and assembly of surface modified metal nanoparticles into selected block copolymer microdomains.[35, 36] The assembly of modified nanoparticles within block copolymers relies on a delicate balance of the interactions between the ligands attached to the nanoparticles and the segments of the block copolymers, as well as the influence of the size of the nanoparticles on the chain configuration of the block copolymers.[37, 38] In addition, this method requires the functionalization of nanoparticles surfaces with small molecules or polymer brushes, which increases the complexity of the synthetic process and limits the use of the metal nanoparticles.

For in situ nanoparticle synthesis, a wide range of metal nanoparticles can be assembled into block copolymer nanostructures via reduction of metal precursors, which can be selectively coordinated with one of the blocks. The reducing methods range from chemical reduction to thermal decomposition, vapor deposition, and sputtering.[39] In aqueous solutions, metal nanoparticles are typically produced from the chemical reduction of metal ions by reducing agents such as $NaBH_4$, citric acid, or ascorbic acid. Externally supplied energy such as photoirradiation,[40] ultrasound irradiation,[41] or heating[42] can be also applied for the reduction.

Until now a big family of electron donor type block copolymers such as polyvinylpyridine (PVP)-containing polymers have been intensively studied for directing the assembly of metal nanoparticles.[43] Owing to the electronegative nitrogen in the pyridine ring, various kinds of metal ions can coordinate with the PVP-containing polymers, which can be further reduced into metal nanoparticles arranged in ordered-patterns. For instance, Buriak and co-workers[44] have fabricated catalytic stamps through a two-step procedure, in which linearly arranged Pt nanopattern is produced in the poly(styrene-2-vinylpyridine) (PS-P2VP) template via in situ reduction of $H_2PtCl_4$, followed by the transfer of the Pt nanopattern onto the

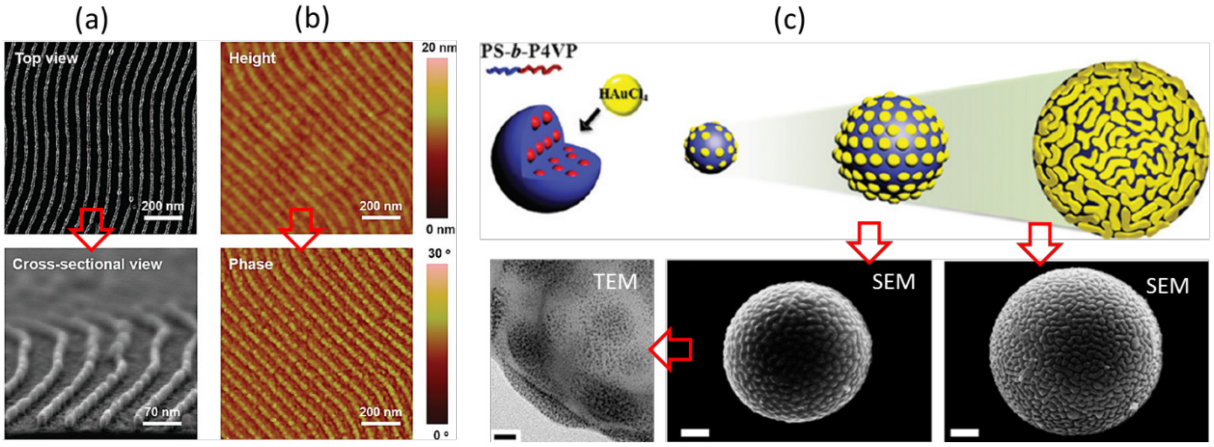


**Figure 1.2.1** SEM (a) and AFM (b) images of a Pt mask with line patterns fabricated from PS-P2VP loaded with Pt salt. [44] (c) Schematic illustration and microscopy images of metal hybrid block copolymer (Au@PS-P4VP) microspheres with controlled surface structures.[45]

poly(dimethylsiloxane) (PDMS) surface through a peel-off approach (Figure 1.2.1a, b). Kim and co-workers[45] reported the patterned decoration of gold nanoparticles on the surface of PS-P4VP particles using in situ reduction of $HAuCl_4$ in P4VP domains under UV irradiation (Figure 1.2.1 c).

Most works of this sort have only focused on the assembly of one type metal nanoparticles.[46, 47] Multifunctional materials usually require the integration of unique properties of different materials. Due to the limited chemical composition of the block copolymers, few of them exhibit selective preferences to different metal nanoparticles.[45] Thus few experiments have been conducted on the assembly of two different types of metal nanoparticles to block copolymer particles with ordered spatial distribution. In addition, there are still technical difficulties in preparing hybrid particles embedded with large amount of metal nanoparticles for practical device applications. Usually the interaction between the high-content metal nanoparticles and their favorable block of the block copolymer will increase its effective volume, resulting in breaking of the ordered structures.[43-46] In general, it is critical to control both the distribution and high loading rate of metal nanoparticles within the block copolymer particles.

Fabrication of size tunable polymer particles by swelling the short rod-like entities generated from Rayleigh instability of polymer nanotubes inside the anodic aluminum oxide (AAO) nanopores was reported recently.[48] Different from commonly used methods, this strategy allows the injection of hybrid materials such as the mixture of metal nanoparticles/polymer. In consideration of the interactions of the AAO wall with different injected materials, this

strategy provides possibilities for the generation of phase separated hybrid nanostructures, which can be promising candidates for the fabrication of BCP particles loaded with different types of metal nanoparticles. In the present thesis, I will study a novel approach for the synthesis of particles selectively loaded with two types of metal nanoparticles.

## 1.3 Mesoporous materials using block copolymers as template

### 1.3.1 Mesoporous polymeric materials

Hierarchically porous materials provide synergies between mechanical properties, transport properties, and enhanced surface area.[49] Integrating 3D continuous mesopores (diameter of 2～50 nm) with macropores (diameter > 50 nm) is of particular importance in catalytic conversions because it combines high specific surface area with high flux. Potential applications range from catalysis to batteries and bioengineering.[49] Among polymeric materials, block copolymer self-assembly is known to generate ordered structures with tunable size and morphology through control over molecular parameters, for instance block component, sequence, and molar mass.[50] Specific methods have been developed to form mesopores, including selective etching,[51, 52]and swelling with sacrificial components.[53, 54]

The selective etching method mainly takes advantage of the degradable character of block copolymers. Nanoporous polymer materials can be prepared by removal of the constituted components in block copolymers through ozonolysis,[55] UV degradation,[56] hydrothermal degradation,[57] or reactive ion etching.[58] Compared with selective etching, another distinct strategy is based on the swelling-induced morphology reconstruction of self-assembled amphiphilic block copolymers without losing any component.[53] In this methodology, pore generation is based upon the confined swelling and subsequent drying-induced collapse of separated microdomains of minority blocks. This strategy has been especially valued in recent studies for the reason of preserving their mechanical strength and chemical heterogeneity of the block copolymers. The block copolymers used in this procedure are generally amphiphilic ones with PS as nonswollen majority block, because its Tg is higher than ambient temperature. Examples include polystyrene-*b*-poly(2-vinylpyridine) (PS-P2VP), polystyrene-*b*-poly(4-vinylpyridine) (PS-P4VP), polystyrene-*b*-poly(acrylic acid) (PS-PAA), polystyrene-*b*-poly(ethylene oxide) (PS-PEO), poly(styrene-*b*-methyl methacrylate) (PS-PMMA), polystyrene-*b*-4-(perfluorooctylpropyloxy)styrene (PS-PFS), and polystyrene-*b*-poly(perfluorooctylethyl methacrylate) (PS-PFMA).[1, 59, 60] The swelling solvents are generally

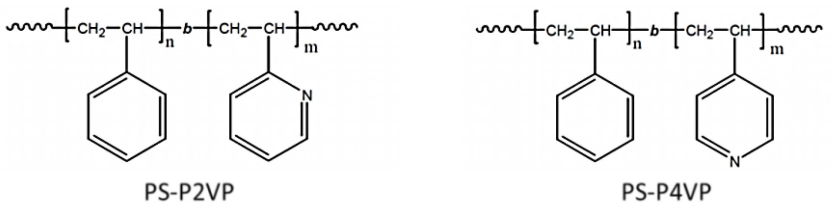


**Figure 1.3.1.1** Molecular structures of polystyrene-b-poly(2-vinylpyridine) (PS-P2VP) and polystyrene-b-poly(4-vinylpyridine) (PS-P4VP).

selective solvents for the minority block but not for the PS block, for example, ethanol for the P2VP phase in PS-P2VP, and supercritical $CO_2$ for the PFS phase in PS-PFS.[59, 60]

The selective swelling of block copolymers for pore generation can occur in nanorods or nanotubes, thin films, and nanoparticles.[12, 53, 54] The thin films with spherical or cylindrical domains are used most frequently to create porous structures. Wang et al.[61] have intensively investigated the evolution of morphology of PS-P2VP films soaked in ethanol with different temperatures and times, showing various porous structures of the thin films (Figure 1.3.1.2). Compared with numerous studies on block copolymer thin films, there are only a few reports on the selective swelling of block copolymer nanoparticles. Porous or hollow block copolymer nanospheres with large surface area and internal loading space are of great importance in medical, biological and catalytic studies. The precise control on the pore opening and closing has attracted increasing interests from researchers. For instance, Jin et al.[12] put much effort on the investigation of swelling induced mesoporous PS-P2VP nanoparticles. They demonstrated a novel way to tune the pore size and their surface arrangement through a supermolecular assembly process. Besides, they also found a pore closing strategy by swelling the porous particles in good solvent vapour to the PS matrix.

Further modification of the porous block copolymer materials will lead to well-designed functional materials. For example, Abetz et al.[62] proposed an approach to functionalize the PS-P4VP membranes with the temperature- and pH-responsive polymer, poly(N-isopropylacrylamide) (pNIPAM)-$NH_2$, leading to a double stimuli-responsive membrane (Figure 1.3.1.2). The modified porous membranes offer promising applications such as molecule separations.

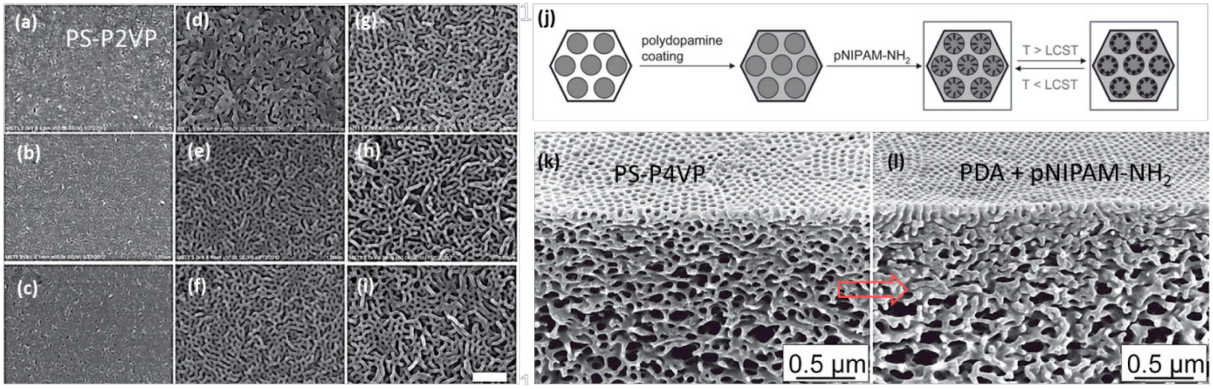


**Figure 1.3.1.2** (a-i) SEM images of porous PS-P2VP membranes prepared at different swelling temperatures and times. The swelling temperatures of (a-c), (e-f), and (g-i) were 55 ˚C, 65 ˚C, and 75 ˚C, respectively. The swelling times of (a, d, g), (b, e, h), and (c, f, i) were 6 h, 15 h, and 24 h, respectively. The scale bar is 500 nm. [61] (j-l) Double-stimuli responsive membrane obtained from functionalization of porous PS-P4VP template.[62]

Current works on porous polymer materials are mainly focusing on porous membrane, closed capsules, and particles with open porous structure.[54-57] More complex nanostructures, such as porous particles with separated chambers or confining spaces of other shapes, have not been extensively studied due to technical difficulties in synthesis. Moreover, a special class with encapsulated guest species such as metal nanoparticles in the interior, is of great interest as nanoreactors for the study of chemical reactions confined in nano-space. The well-established pore-making strategies of block copolymers provide the possibility of synthesizing the aforementioned complex nanostructures. For example, the selective swelling induced porous materials can be applied as templates, which can not only introduce functional materials to the backbones, but also be removed by dissolving, leading to complex porous and hollow structures. As far as we know, there is no report on the using of porous polymer particles as soft template for the synthesis of more complex nanostructures.

Therefore, this thesis will study the templating effect of porous PS-P2VP particles on the synthesis of polydopamine@gold nanoreactors particles with interconnected pore structure.

### 1.3.2 Mesoporous metal and metal oxide materials

Compared with porous polymeric materials, metal and metal oxides possess stronger chemical and thermal resistance. Such porous inorganic materials have exceptional properties such as low relative density ($\rho_{MNMs}/\rho_{bulk}$), enhanced plasmonic behavior, high strength-to-weight ratio, and size effect-enhanced catalytic behavior.[63] These properties are of great interest in many fields of applications including supercapacitors, high-power-density batteries, viable

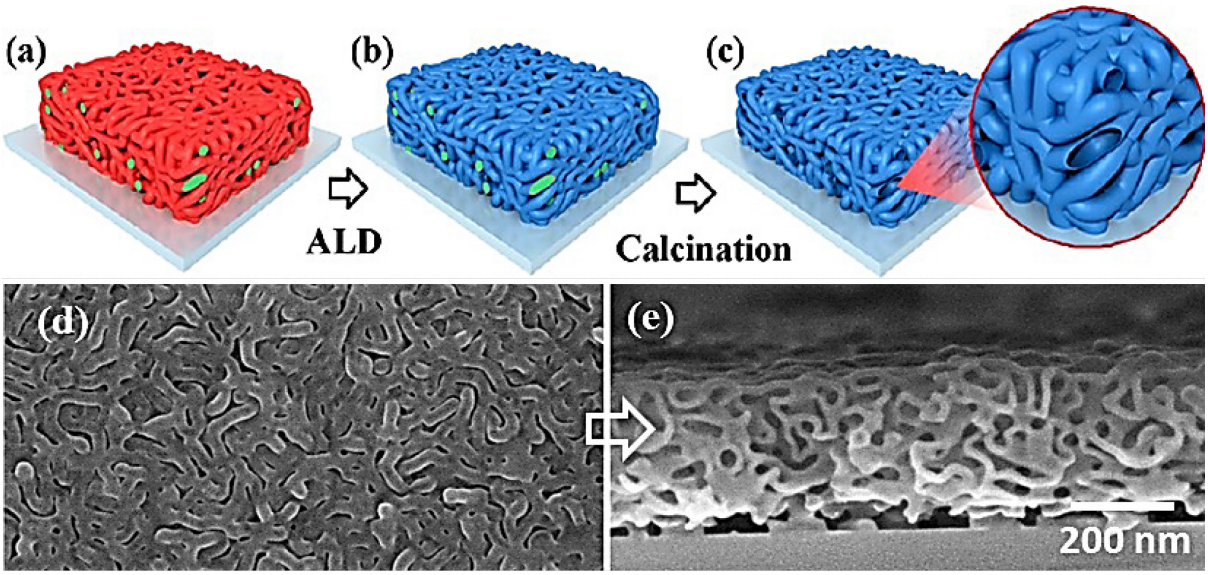


**Figure 1.3.2.1** (a-c) Schematic illustration for the preparation of alumina networks of interconnected nanotubes by ALD on swelling-induced mesoporous block copolymer templates. (d) Top view and (e) cross-sectional view of the alumina porous membrane with interconnected tube structure.[69]

hydrogen storage, and high-efficiency catalysts.[64] Porous metal or metal oxides are much more difficult to be fabricated in comparison with porous block copolymer materials. Only a few synthetic pathways have been demonstrated. For instance, by using a bottom-up approach, aerogels with metallic backbones can be obtained from direct assembly of metal nanoparticles into gels via sol-gel process.[65] In contrast, by using a top-down approach, nanoporous Au can be prepared via selective removal of Ag from a Au-Ag alloy (a process called dealloying).[66]

Apart from the conventional methods, recent studies have been focusing on the soft-template method by using porous block copolymer materials as template. A variety of approaches, such as electrochemical deposition,[67] electroless plating,[68] and atomic layer deposition (ALD)[69] have been well demonstrated for the deposition of metal and metal oxides onto block copolymer templates. Among them, atomic layer deposition offers exactly advantages in control of the synthesis at atomic level of metal oxides. The deposition onto interconnected block copolymer network is proved to be a simple strategy to prepare metal oxides with finely adjustable, interconnected pore morphologies. Wang et al.[69] have synthesized different porous metal oxides by using porous PS-P4VP membrane obtained from a selective swelling method as template, followed by the replica of different metal oxides involving $Al_2O_3$, $TiO_2$, ZnO, $V_2O_5$, $WO_3$, $MoO_3$ (Figure 1.3.2.1) through the ALD method.[69, 70]

Different from bulk or membranes, metal oxide nanoparticles can exhibit unique physical and chemical properties due to their limited size and a high density of corner or edge surface sites.[71] Although the synthesis of porous metal oxide membranes has been well developed, there are few reports on the synthesis of conductive metal oxide nanoparticles, such as $Ti_4O_7$ particles, with interconnected pores in the interior. Such kind of particles can provide polar surface, high conductivity, as well as separated confining spaces, which are highly valued as sulphur host materials for lithium-sulphur (Li-S) battery.[72, 73] Unfortunately, technical difficulties are still existing in the synthesis of such kind of porous metal oxide particles. On one hand, the commonly used deposition methods such as electroless plating and atomic layer deposition no longer fit for the nanoparticle templates, which are usually dispersed in aqueous or organic solution. On the other hand, in comparison with 2D membranes, the deposition or growth of metal oxides on the surface of block copolymer nanoparticles are more difficult due to the curvature. Thus, it remains a big challenge to develop a simple and universal method for the synthesis of conductive metal oxide nanoparticles with complex inner structure.

In my study, the swelling induced porous block copolymer particles have been applied as template to direct the deposition of metal oxide precursors (titanium isopropoxide), followed by the hydrolysis and calcination. The block copolymer templates can be removed by calcination, leading to the porous $Ti_4O_7$ particles. This thesis will demonstrate the obtained porous $Ti_4O_7$ particles can work efficiently as cathode materials for Li-S batteries.

## 1.4 Objectives

The main objective of this thesis is to synthesize novel functional materials with complex structures by using block copolymer nanoparticles as soft templates. Their possible applications as efficient catalyst and cathode material for Li-S batteries will be investigated. PS-P2VP particles and their porous structures induced from a selective swelling process have been used as templates.

First, PS-P2VP dense particles with ordered phase-separation structures can be applied to direct the assembly of metal nanoparticles into ordered patterns. The main interest of this work is to assemble two different types of metal nanoparticles onto one polymer particle. The control over the types of metal nanoparticles and their separated spatial distribution is a big challenge that has not been realized before this work. The investigation is carried out as follows:

- In order to realize the assembly of Pd and Au nanoparticles onto PS-P2VP nanospheres with separated distribution, a synthesis route has been designed by combining the Rayleigh instability of polymer nanotubes inside AAO membrane with a swelling process in toluene/water emulsion.
- To follow the morphology transformation of the target particles from the beginning, TEM characterization has been applied at different steps of the synthesis procedure. The influences of the concentrations of PS-P2VP and Au nanoparticles on the morphology of the resulting particles have been studied.
- To study the optical properties of the target particles, UV-vis absorption has been measured for the particles with different core sizes. The catalytic activity of the particles has been investigated with a model reaction, the reduction of 4-nitrophenl by $NaBH_4$.

The second work aims at synthesizing the PDA@Au nanoreactors with interconnected channel structure by using porous PS-P2VP particles obtained from a selective swelling process. The influence of the complex structure on the catalytic reaction of 4-nitrophenol has been studied. The investigation has been conducted as follows:

- In order to generate a new type of nanoreactors with interconnected channel structure, porous PS-P2VP particles obtained from a selective swelling process, which consists of interconnected networks of micellar nanofibers, have been used as templates.
- The control over the thickness of the PDA layer has been studied by tuning the polymerization time. The morphology of the product has been characterized by TEM. The formation of PDA and Au nanoparticles has been demonstrated by FTIR and XRD spectra.
- To get the 3D structures of the template and the product, a direct visualization method, Electron tomography (ET), has been applied for both the porous PS-P2VP template and the resulted PDA@Au nanoreactors, inside of which Au nanoparticles are embedded separately in the channels.
- Additionally, the full kinetics of the reduction of 4-nitrophenol has been studied by using the PDA@Au particles as catalytic nanoreactors. Different concentrations of 4-nitrophenol and sodium borohydride have been used for the experimental and theoretical study. A comparison has been made between the catalytic system in this work and those reported in literatures, including Au nanoparticles immobilized in spherical polyelectrolyte brush (SPB) and ligand-free Au nanoparticles.

The third work aims at synthesizing porous $Ti_4O_7$ particles with high surface area and interconnected pores, which can provide both polar surface and valid confining volume for polysulfides in Li-S batteries.

- PS-P2VP templates with different porosities have been applied to generate the $Ti_4O_7$ particles. To optimize the experimental conditions, a series of hydrolysis ratios ($Ti/H_2O$ molar ratio) have been studied.
- To obtain the $Ti_4O_7$ crystal structure, calcination in a tubular furnace at 900 ˚C under Ar atmosphere has been carried out to reduce the insulating $TiO_2$ into Magnéli phase titanium sub-oxides ($Ti_4O_7$). To reveal the porous structure of the $Ti_4O_7$ particles, SEM, TEM and BET measurements have been conducted on the porous particles. A layer of carbon has further been coated on the surface of the $Ti_4O_7$ particles to improve the conductivity of the particles.
- To evaluate the electrochemical properties of the $Ti_4O_7$/S and carbon coated $Ti_4O_7$/S composite, 2032-type coin cells have been fabricated with thick coated electrode films, in which the mass loading of sulphur has been controlled to be approximately 1.0~1.2 mg per electrode. The CV profiles, rate capabilities and cycling performance have been investigated and compared with the $TiO_2$/S cathode.

# 2. Theory

## 2.1 Formation of block copolymer nanoparticles

Block copolymer nanoparticles are widely used in various applications in the fields of photonics, electronics, and biotechnology.[21] There are many preparation methods for the synthesis of such kind of nanoparticles, including milling of bulk materials, emulsion polymerization, and reprecipitation.[74] However, it has not been achieved to combine tunable size of the particles together with highly ordered nanostructure derived from the microphase separation using the aforementioned methods. This is because the size and shape of the polymer precipitates are largely dependent on physical conditions such as the speed of mixing and evaporation. The highly ordered nanostructure is strictly dependent on a narrow distribution of the molecular weight, which is difficult to achieve in emulsion polymerization.

Very recently, a novel synthesis strategy based on the Rayleigh instability of polymer nanotubes confined in anodic aluminum oxide (AAO) nanopores has been reported by Jin et al.[48] In the demonstrated model, PS-P2VP particles with tunable size and highly ordered nanostructures can be obtained by using commercial block copolymers with a narrow polydispersity index (PDI) value. In this thesis, these PS-P2VP particles with well-defined morphology have been applied as soft templates for the assembly of metal nanoparticles. In addition, the swelling induced porous PS-P2VP particles have been used as templates for the synthesis of more complex structures, including polydopamine@gold particles and $Ti_4O_7$ particles with interconnected porous hierarchy.

### 2.1.1 Formation of block copolymer nanospheres based on Rayleigh instability

Lord Rayleigh (1878) examined a common experience: a thin jet of liquid is unstable and breaks into droplets.[75] When a jet is thin enough, the effect of gravity is negligible compared to surface energy. The jet changes its shape to reduce the total surface energy. This phenomenon is named as the Plateau-Rayleigh instability, often just called the Rayleigh instability.[76, 77]

The driving force of the Rayleigh instability is that liquids, by virtue of their surface tensions, tend to minimize their surface area. Srolovitz and Safran (1986) gave a simple geometric argument.[79] Assume that the surface energy density is isotropic, and the free energy of the

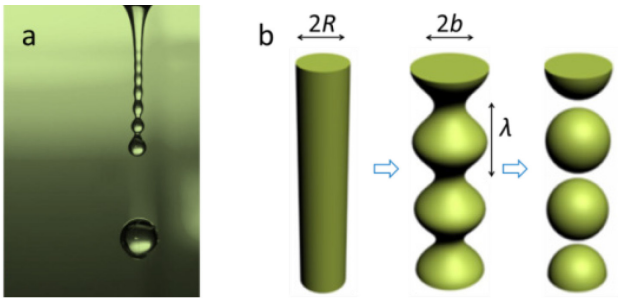


**Figure 2.1.1.1** Graphical illustration of the Rayleigh instability. A liquid cylinder undulates and transforms into a chain of spheres. (a) Real water flow and (b) graphical model.[78]

system is the surface area ($S$) times the surface tension ($\gamma$). One has to show that the cylinder has a larger surface area than the row of spheres. Consider a long cylinder with radius $R$, and a row of droplets with radius $b$. Imagine that the cylinder evolves to the droplets by first perturb the surface with a wavelength $\lambda$. The volume per wavelength of the cylinder equals the volume of each droplet, so that the droplet radius is given by $b = (\frac{3\lambda R^2}{4})^{\frac{1}{3}}$. The free energy per wavelength of the cylinder is $2\pi R\lambda\gamma$. The free energy per droplet is $4\pi b^2\gamma$. The free energy of cylinder is larger than the row of droplets if $\lambda > \frac{9R}{2}$. From this geometric (energetic) consideration, one can expect that a thin liquid flow will evolve to a row of spheres with large enough radius.

The Rayleigh instabilities also occur when a liquid film is coated onto the wall of a capillary tube. For a thin liquid film with a thickness $e$, and a tube with a pore radius $b$, when $e \ll b$, the film undergoes an undulation process to minimize the surface energy. As the amplitude of undulation grows with time, crests may merge to form bridges across the capillary tube, producing a rod with periodic encapsulated holes.[80-82] The transformation process of polymer nanostructures is shown in Figure 2.1.1.2. There are four states in the transformation process, including (A) nanotubes, (B) undulated structures, (C) Rayleigh-instability-induced structures, and (D) nanorods.

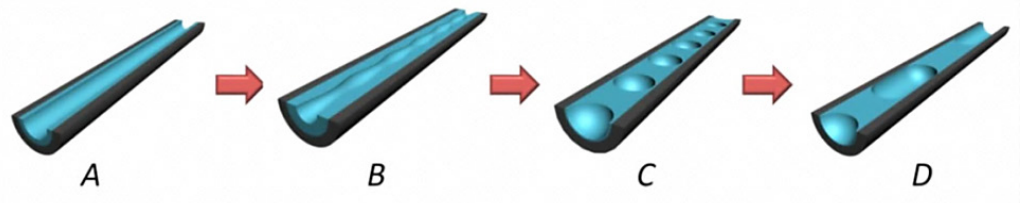


**Figure 2.1.1.2** Schematic mechanism of the transformation process by thermally annealing polymer nanotubes confined in the nanopores of AAO templates. The polymer nanotubes (A) are transformed to undulated structures (B), Rayleigh instability-induced structures (C), and finally nanorods (D).[78]

According to the theory of the Rayleigh instability, the relationship between the wavelength of the undulation and the diameter of the cylinder can be shown as the following: [79]

$$\lambda = (2\pi\sqrt{2})b \qquad (1)$$

This indicates the length of the rod like structures ($\lambda$) can be directly controlled by tuning the capillary pore size ($b$). Theories also predict how fast the structure transformation occurs:

$$\tau_M = \frac{12\eta b^4}{\gamma e^3} \qquad (2)$$

Where $\tau_M$ is the characteristic time, $\eta$ is the viscosity, $b$ is the pore radius, $\gamma$ is surface tension of liquid, and $e$ is the initial film thickness. According to the formula, $\tau_M$ is proportional to the viscosity of the liquid. In the case of polymer melt, the viscosity changes with temperature and molecular weight. The morphology diagrams of the transformed structures of polystyrene (PS) at different annealing temperatures and times are constructed based on experiment results, showing the kinetic pathway of the structure transformation.[78] From the morphology diagrams (Figure 2.1.1.3), it can be observed that the initial instability structure region occurs at shorter times when the annealing temperature is higher. For example, initial instability PS ($M_n$ = 24 kg/mol) structure region is ~18 h when the annealing temperature is 110 °C (Figure 2.1.1.3a), which is reduced to ~1 h when the annealing temperature is increased to 130 °C. Therefore, the time required to transform from the tube structures to the instability structures at 130 °C is shorter than that at 110 °C. In addition, the instability structure region is larger at lower annealing temperatures. Similar tendency in the morphology diagram can be observed for PS with higher molecular weight ($M_n$ = 100 kg/mol), as shown in Figure 2.1.1.3b.

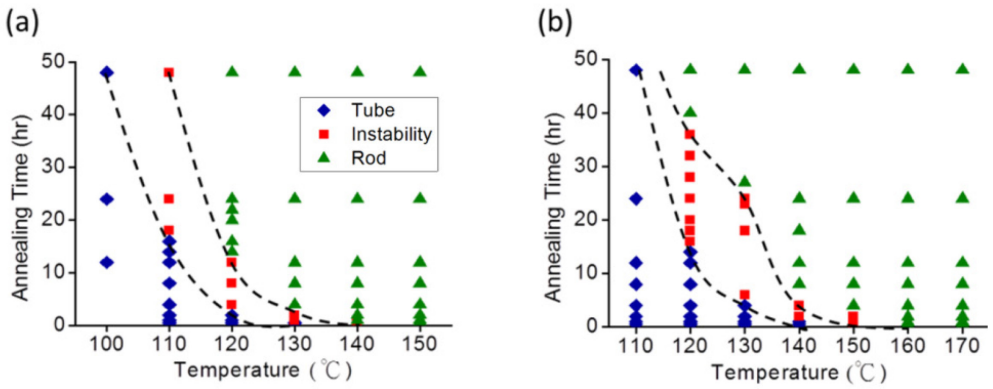


**Figure 2.1.1.3** Morphology diagrams of polymer nanostructures from PS with two different molecular weights: (a) $M_n$ = 24 kg/mol and (b) $M_n$ = 100 kg/mol. The solid blue diamonds indicate the nanotube structures. The solid red squares indicate the instability structures. The solid green triangles indicate the nanorod structures.[78]

The polymer nanorods with periodic holes are demonstrated to be easily broken during morphology characterizations.[83] This inspires Jin et al.[48] to cut the nanorods at the weak part to generate nanoblocks with similar length. After swelling in toluene/water emulsion followed by evaporation of toluene, the nanoblocks transformed into nanospheres. A mechanism for the structural transformations induced by swelling-deswelling process has been proposed (Figure 2.1.1.4). Toluene is a good solvent for polymers and is slightly soluble in water. As it diffuses into the polymer blocks, they swell and the solid blocks become liquid droplets.[84] The swollen blocks adjust their shapes into spherical droplets in order to minimize the interfacial energy. Without surfactant, the swollen particles coalesce. When surfactant is present, they remain stable. The toluene can be removed by steam stripping or thermal annealing, which are common methods for removing organic solvents from polymer dispersions.[85] Because toluene and water have a large miscibility gap, this procedure removes nearly all the toluene.

Current studies of this sort have only demonstrated the synthesis of pure polymer particles. The generation of hybrid particles by using the method based on Rayleigh instabilities has not been approved. Wetting the AAO channels with hybrid melt such as the mixture of block copolymer/metal nanoparticles will provide opportunities for the study of the instability of

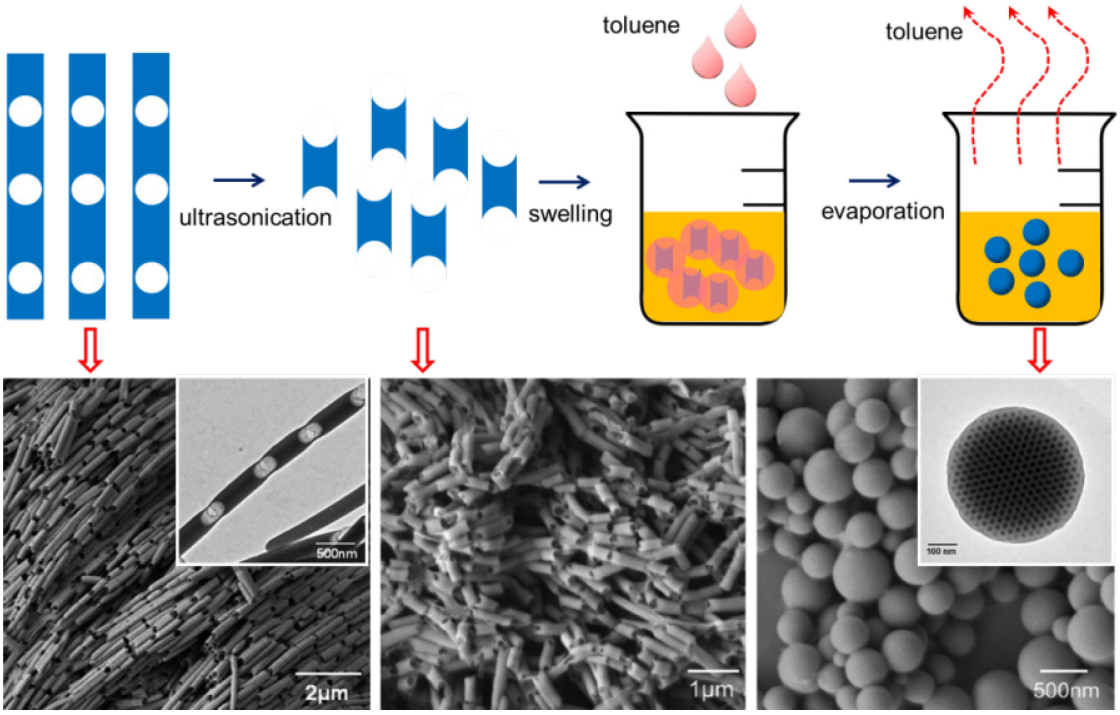


**Figure 2.1.1.4** Synthesis process of polymer nanospheres from short nanorods obtained from Rayleigh instability (upper panel) and corresponding SEM and TEM images of the PS-P2VP nanostructures (lower panel).[48]

heterogeneous phase. The instability and the phase behaviors inside the AAO channels are of great interest, which will greatly affect the morphology of the resulting hybrid particles. The location of the injected metal nanoparticles and their influence on the surface pattern of the resulted hybrid particles are needed to be revealed.

In this thesis, I use the mixture of PS-P2VP/gold nanoparticles for the first time as the wetting materials. The instability of the hybrid melt inside the AAO channels and the morphology of the resulting hybrid particles have been studied. The assembly of a second type of metal nanoparticles onto the hybrid particles is also attempted, aiming at exploring a novel synthesis of multifunctional materials.

### 2.1.2 Selective swelling induced porous block copolymer nanoparticles

#### 2.1.2.1 Mechanistic understanding of the pore formation process

The selective swelling-induced pore generation process can be described as three steps:
(1) Uptake of the selective solvent
(2) Swelling of the minor block
(3) Drying by solvent evaporation
We take PS-P2VP as an example. Upon immersion of the block copolymer in ethanol, which is a solvent selective for the PVP phases, ethanol diffuses into the film and is preferentially enriched in the PVP microdomains because of the much stronger affinity of ethanol toward PVP than toward PS. The PVP microdomains are consequently swollen and expanded, leading to the progressive accumulation of osmotic pressure. It was found that the glass transition temperature (Tg) of PS homopolymers was decreased from 100 °C in the dried state to 82 °C when immersed in ethanol,[86] revealing the moderate plasticization/swelling effect of ethanol toward PS. Considering that the swelling process is performed at elevated temperatures (typically at 60-75 °C) that are slightly lower than the Tg of PS in ethanol, plastic deformation of the PS matrix will occur, driven by the accumulated osmotic pressure in the PVP microdomains. Upon drying, the swelling PVP chains collapse with the evaporation of ethanol. However, the spaces initially occupied by the expanding PVP microdomains are fixed because the PS matrix accommodating these spaces loses its mobility in the absence of ethanol and a driving force for recovery. Consequently, pores are created in

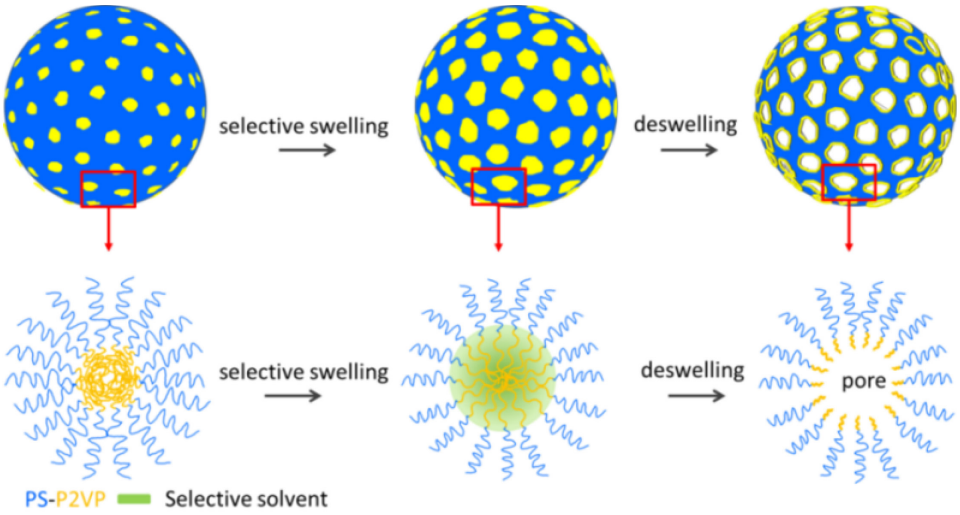


**Figure 2.1.2.1.1** Schematic mechanism of the pore formation process. The model polymer is PS-P2VP, the selective solvent is ethanol.

these spaces with the collapsed PVP chains lying along the pore wall (Figure 2.1.2.1.1). Under stronger swelling conditions, the PVP microdomains are highly swollen. Consequently, the adjacent PVP domains contact and then merge to form a continuous phase of swelling PVP chains, correspondingly resulting in an interconnected porosity in the subsequent drying process. Experiments show that the drying step does not noticeably influence the pore sizes.[87] This is because for a given BCP film the pore size is determined by the amount of the swelling solvent taken up by the PVP microdomains. Once the solvent is completely evaporated, the pores will be fixed to the same size regardless of how fast the polymer is dried.

Both block copolymer compositions and swelling conditions, including swelling agents, temperature and duration, influence the swelling behaviors and consequently the morphologies of the obtained porous materials. According to the phase diagram,[88] for PS-PVP with PS as the majority block, the PVP phases in the morphology of spheres,[89] cylinders, [14] and gyroids[91] are suitable to be converted into the nanoporous structures through this swelling mechanism. Therefore, block copolymers with volume fractions ($f$) of the minority in the 5% - 38% range can be converted to porous structures, while those with $f$ > 38% may be directly dissolved in the selective solvent.

### 2.1.2.2 Interaction between selective solvents and block copolymers

The morphology of the swollen materials is affected by several factors including the volume fraction of the swollen block, the chemical properties of solvents, and the corresponding block-block and block-solvent $\chi$-parameters (the Flory-Huggins parameter).[91] $\chi$ can be

roughly estimated by analyzing the difference between the solubility parameter ($\delta$) of each component. The solubility parameter can be calculated from the sum of the squares of the Hansen dispersive ($d$), polar ($p$), and H-bond ($H$) components:

$$\delta = \sqrt{(\delta^d)^2 + (\delta^p)^2 + (\delta^H)^2} \quad (3)$$

When the solubility parameters of the polymer and the solvent are similar, dissolution of polymer is optimal. As these values diverge, the polymer coils in diluted solutions contract.[92, 93] For block copolymers, the solubility of each block in the selective solvent will determine which block is preferentially swollen.

As discussed above, we take PS-P2VP as the model block copolymer. Table 2.1.2.2.1 lists the dispersive ($\delta^d$), polar ($\delta^p$) and H-bond ($\delta^H$) contributions of the single solvent ethanol and two blocks of PS-P2VP. The interaction between the blocks and the solvent can be indicated from the calculated value of $(\delta_{solvent} - \delta_{block})^2$. Relatively larger value indicates poorer interactions. If a solvent mixture is applied, the solubility parameter as well as the porous morphology can be tuned by changing the solvent composition. As shown in table 2.1.2.2.1, compared with PS, P2VP block is more polar and easy forming H-bond with ethanol. Differences in the solubility parameters are much larger between PS and ethanol than they are between P2VP and ethanol. Experiment results also demonstrate that the PS block almost has no contact with ethanol.[87]

**Table 2.1.2.2.1** Hansen solubility parameter [a] contributions for the solvent and copolymer blocks, and the interactions between solvent and different blocks.

| compound | $\delta^d$ (MPa$^{1/2}$) | $\delta^p$ (MPa$^{1/2}$) | $\delta^H$ (MPa$^{1/2}$) | $\delta$ (MPa$^{1/2}$) |
|---|---|---|---|---|
| Polystyrene | 18.6 | 1.0 | 4.1 | 19.0 |
| Poly(2-vinylpyridine) | 19.0 | 8.8 | 5.9 | 21.8 |
| ethanol | 15.8 | 8.8 | 19.4 | 26.5 |
| $(\delta_{ethanol} - \delta_{PS})^2$ | 7.8 | 60.8 | 234.1 | 56.3 |
| $(\delta_{ethanol} - \delta_{P2VP})^2$ | 10.2 | 0 | 182.3 | 22.1 |

[a] C. M. Hansen, Hansen solubility parameters: a user's handbook, CRC Press, 1999.

Porous polymers have been extensively studied with increasing interests, a broad range of applications have been reported in gas storage materials, supports for catalysts, precursors of nanostructured carbon materials, filtration/separation membranes, proton exchange membranes, packing materials in chromatography and in many other fields.[1, 94] However, there are very few reports on the using of porous polymers as soft template for the synthesis of more complex nanostructures. Porous structures produced by selective etching usually lose their active component of the block copolymers, resulting in big limitation in the application as soft template. On the contrary, the selective swelling induced porous structures preserve their mechanical strength and chemical heterogeneity of the block copolymers. These materials provide both geometric confinement and active sites for further functionalization, thus can be perceived as potential soft templates for the synthesis of more complex structures.

Therefore, this thesis will study the templating effect of porous PS-P2VP particles on the synthesis of polydopamine@gold nanoreactors and $Ti_4O_7$ particles with interconnected porous structure.

## 2.2 Morphology study of the polymer-based nanoparticles by electron tomography

Deeper research on the polymer-based materials requires specific powerful tools to characterize their properties and complex morphologies. Microphase-separated structures and mesoporous structures are becoming increasingly complicated with advances in precision synthesis. Characterization of such complex morphologies becomes more problematic.

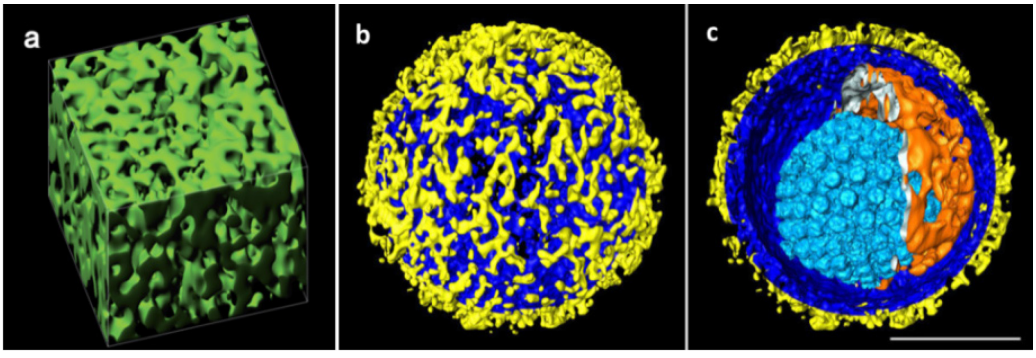


**Figure 2.2.1** Reconstructed 3D images of the PAMAM dendrimer in a PEG network (a),[95] and 3D structure of a herpes virus (b, c),[96] including the layers that make up its shell: as its innermost layer, the capsid (light blue) - a protein shell with icosahedral symmetry - encloses the viral DNA. This layer is surrounded by the so-called tegument (orange), which is enclosed by the envelope (dark blue). Within the envelope, the tegument, a network of various proteins, is arranged asymmetrically around the capsid.

Micrographs taken by conventional microscopy, e.g., TEM, are often inconclusive. This makes the interpretation of the accompanying scattering data quite difficult. The conventional microscopes take two-dimensional (2D) (transmitted or surface) images of three-dimensional (3D) objects. The more complicated the morphologies, the less convincing the 2D images become. It is quite natural to develop new microscopes capable of obtaining 3D images.

The development of electron tomographic (ET) method provides a way to determine the 3D architecture.[97, 98] Current studies have shown its powerful capability of revealing complex structures such as cells and porous polymer materials (Figure 2.2.1). There is also considerable excitement about the prospect of applying ET method, especially for the analysis of dynamic macromolecular assemblies that are not easily studied by methods such as Scanning electron microscopy (SEM), Transmission electron microscopy (TEM), X-ray crystallography, and NMR spectroscopy.[99] In this thesis, ET is applied to investigate the 3D structure of the synthesized porous polydopamine@gold nanoreactors.

### 2.2.1 Electron tomography process: data acquisition

Electron tomography (ET) is a method for generating 3D images on the basis of multiple 2D projection images of a 3D object, obtained over a wide range of viewing directions (Figure 2.2.1.1).[100] The 3D image is generated in a computer by back-projecting each 2D image with appropriate weighting.

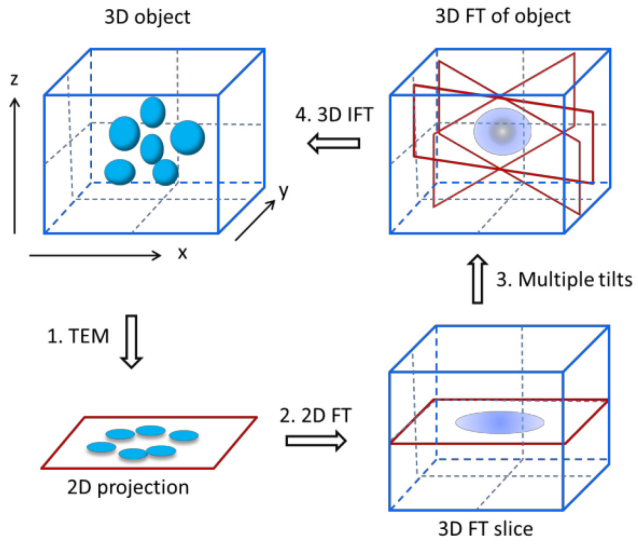


**Figure 2.2.1.1** Schematic of a tomographic reconstruction in recipical space: (1) acquisition of projecion images; (2) Fourier transorm; (3) combination of Fourier transform at different tilt-angles, and (4) inverse Fourier transform (IFT) to reconstruction original shape.[100]

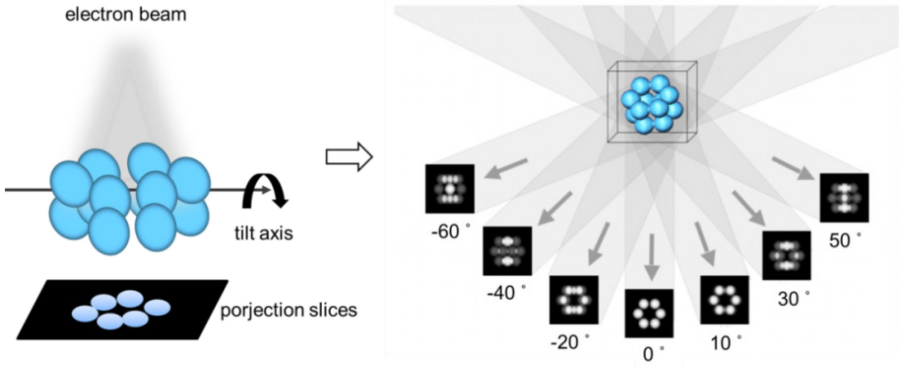


**Figure 2.2.1.2** Single-tilt axis data acquisition geometry. The specimen is imaged in the microscope by tilting it over a range of typically ± 60 or 70 degrees in small tilt increments. As a result, a set of projection images (tilt series) needed for tomographic reconstruction is collected.[102]

The principle of ET is the 3D reconstruction of a specimen from a series of projection images taken with a transmission electron microscope. In ET, a single individual sample is introduced in the electron microscope and a series of images (called tilt series) are recorded by tilting the sample around a single-tilt axis at different angles, typically over a tilt range of ± 60 or 70 degrees and at small increments of 1-2 degrees (Figure 2.2.1.2). Typical ET data sets then range from 60 to 280 images. Due to the resolution requirements, the image size typically is 2048 x 2048, 4096 x 4096, or even 8192 x 8192 pixels.

Computer-automated data collection has been crucial for the advent of ET as a structural technique in cellular biology.[101] It allows automated tracking, focusing and recording of images under low electron-dose conditions by dividing the maximum tolerable dose over the total number of images. This preserves the specimen from radiation damage. But, as a consequence, the images exhibit a poor signal-to-noise ratio (SNR) around 0.1. During acquisition, the imperfections of the mechanical tilt system and the electron optics produce shifts in the images. The larger component of these shifts is compensated by the automated tracking procedure. However, a more accurate alignment of the images is needed afterwards by computational procedures.

### 2.2.2 Electron tomography process: tomographic reconstruction

The mathematical principles of tomographic reconstruction are based upon the central section theorem, which states that the Fourier transform (FT) of a 2D projection of a 3D object is a central section of the 3D FT of the object. [102] Therefore, the 3D FT of the specimen can be computed by assembling the 2D FTs of the images in the tilt series, which yields the 3D structure of the specimen by an inverse FT.

The standard method for tomographic reconstruction is Weighted Backprojection (WBP), which essentially is equivalent to the Fourier approach just described but working in real space.[102] WBP assumes that the projection images represent the amount of mass density encountered by imaging rays. The method simply distributes the known specimen mass present in projection images evenly over computed backprojection rays. This way, the specimen mass is projected back into a reconstruction volume (backprojected, Figure 2.2.2.1a). When this process is repeated for all the projection images in the tilt series, backprojection rays from the different images intersect and reinforce each other at the points where mass is found in the original structure. Therefore, the 3D mass of the specimen is reconstructed from a series of 2D projection images.

The limited tilt range in ET results in a region empty of information in the Fourier space of the 3D reconstruction (missing wedge, Figure 2.2.2.1b). The resolution of the reconstruction is thus anisotropic (direction-dependent). In real space, it produces artefacts as blurring of the spatial features in the beam direction, making some features appear as elongated in that direction (there is a significant loss of resolution in the Z-direction), features oriented perpendicular to the tilt axis tend to fade from view, and others are not resolved at all. A ± 70 tilt range involves that 22% of the information is missing. The use of double-tilt axis acquisition geometry significantly reduces the missing information (down to 7% in the case of ± 70 tilt range). The angular sampling, that is, the interval between successive tilt images, is another point affecting the resolution of the reconstruction. The more projection images, the better the angular sampling, and as a consequence the better the resolution.

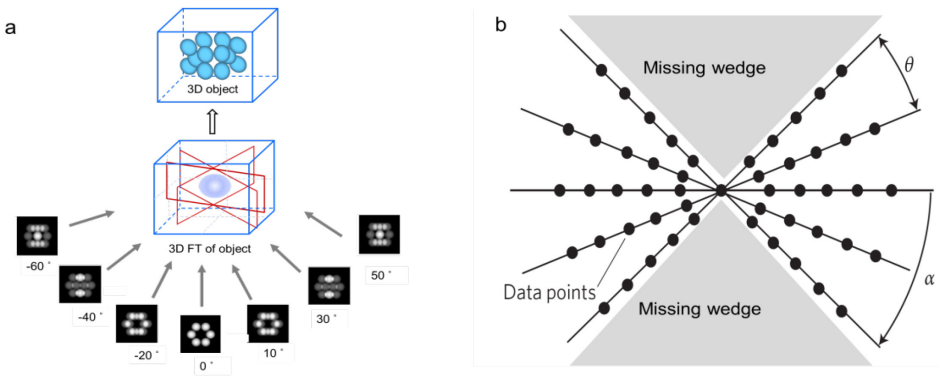


**Figure 2.2.2.1** Three-dimensional reconstruction from projections. (a) shows that in the backprojection, the images in the tilt-series are projected back into the volume to be reconstructed. (b) shows the missing wedge results from the limited tilt range.[102]

Although electron tomography has been applied in materials science since the late 1980s, its popularity has still been limited in the characterization of polymer materials. The limiting factors are beam damage, low resolution and the difficulties in image processing and reconstruction.[103] The last two factors are strongly dependent on the quality of the samples, but the beam damage is the limiting factor for most of the polymer materials. Therefore only the polymers which are stable enough under the electron beam processing are possible for ET. In addition, because electrons interact strongly with samples, the resolution is limited by the density and the thickness of the samples. Usually samples should be less than ~500 nm thick to achieve high resolution. Further more, many hybrid materials which have similar contrasts between the different components are not favorable for ET. For this reason, most hybrid samples of this kind have to be selectively stained with heavy metal or other crosslinkers. This usually becomes an obstacle to reveal the initial structures.

In this thesis, we utilize electron tomography method to study the inner structure of the polydopamine@gold nanoreactors. The chemically and physically stable properties of polydopamine allow the utilization of this method. Moreover, the low resolution, which is usually caused by the big size ( hundreds of nanometers) of the dense samples, can be avoided because of the highly porous structure as well as the different contrasts between polydopamine and gold. For these reasons, the study on the inner structure of the polydopamine@gold nanoreactors is highly valued.

## 2.3 Kinetic study of the reduction of 4-nitrophenol using metal nanoparticles as catalyst

The assemblies of metal nanoparticles with block copolymer (BCP) matrices are considered as novel functional hybrid materials with applications in catalysis, sensors, optics and electronic devices.[104-107] The presence of well-ordered, high-content nanoparticles within BCP matrices may offer the composite materials with enhanced collective properties.[108] One of the most important applications of noble metal nanoparticles such as silver, gold, palladium, and platinum nanoparticles, is using them as highly effective catalysts.[109] To determine the catalytic activity of different metal nanoparticles as well as the influence of the carrier system on the catalytic reactions, a model reaction is necessary. This model reaction should proceed without side reactions in the presence of nanoparticles and should not take place without the catalyst.[110] The reaction should be easy to monitor in order to obtain a complete kinetic analysis. Furthermore, the reaction should take place under mild conditions to ascertain that

the particles keep their initial structure. It is crucial that no degradation or transformation of the nanoparticles occurs within the measured environment. Such a model reaction allows the direct comparison of the catalytic activity of various metallic nanoparticles and a wide range of different carrier systems.

### 2.3.1 Catalytic reduction of 4-nitrophenol as model reaction

Previous research demonstrates that the reduction of 4-nitrophenol by sodium borohydride in the presence of metal nanoparticles can meet all the requirements discussed above as a model reaction (Figure 2.3.1.1).[111-115] This reaction is easily followed by UV-vis spectroscopy due to the fact that 4-nitrophenol shows a distinctive absorption peak at 400 nm in alkaline solution. The product, 4-aminophenol, exhibits a weak absorption peak at around 300 nm. In Figure 2.3.1.1 the UV-vis spectra of the reaction is shown. Several isosbestic points confirm that there are no side reactions and only one product is formed. Without the catalyst the reduction of 4-nitrophenol does not proceed. From the vanishing intensity of the absorption at 400 nm, the reaction rate can be calculated by a pseudo first order reaction, if an excess of sodium borohydride is used.[116, 117]

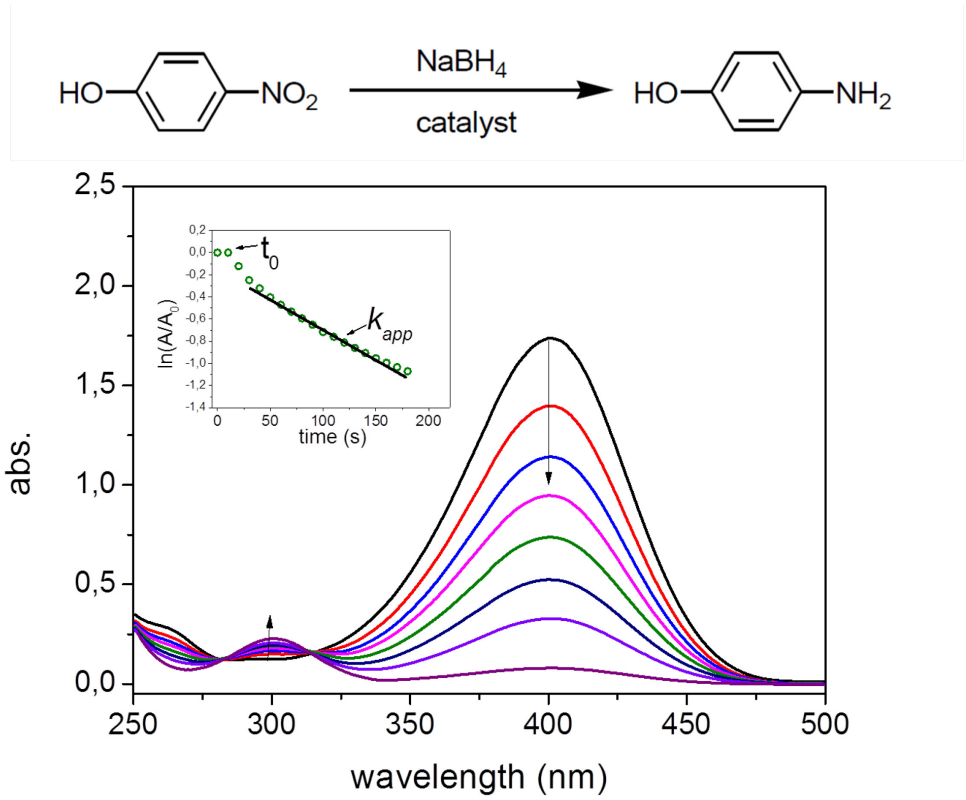


**Figure 2.3.1.1** UV-vis spectra of the reduction of 4-nitrophenol by sodium borohydride in the presence of metal nanoparticles. The inset shows the typical time trace of the absorption of 4-nitrophenolate ions at 400 nm.

### 2.3.2 Kinetics of the model reaction

As discussed above, 4-nitrophenol has an absorption peak at 400 nm in the UV-vis spectrum, which is reduced with the time due to the conversion of 4-nitrophenol. The end product is 4-aminophenol which has an absorption peak at 300 nm. In Figure 2.3.2.1 the reaction pathway of 4-nitrophenol to 4-aminophenol is shown.

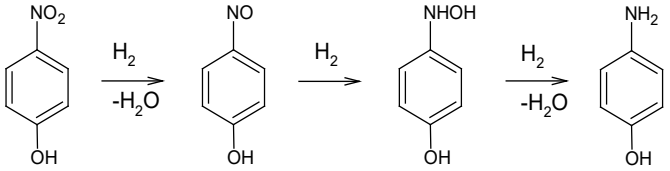


**Figure 2.3.2.1** Proposed mechanism of the reduction of nitrophenol by metallic nanoparticles. All intermediates remain adsorbed during the reaction. The reduction of nitrosophenol is fast but the subsequent reduction of 4-hydroxyaminophenol to aniline is slow and rate-determining.[118, 119]

As shown in Figure 2.3.2.1, two intermediates named 4-nitrosophenol and 4-hydroxylamine may be identified. The first stable intermediate is the hydroxyaminophenol. Investigations clearly reveal that all steps of the reduction reaction proceed on the surface, that is, only adsorbed molecules react.[118-120] Thus, there are three compounds adsorb and desorb during the reaction cycle, namely 4-nitrophenol, 4-hydroxyaminophenol and aminophenol.

The actual concentrations of 4-nitrophenol, 4-hydroxyaminophenol, and 4-aminophenol can be presented as $c_{Nip}$, $c_{Hx}$, and $c_{Amp}$, respectively. The surface coverage $\theta_{Nip}$ of 4-nitrophenol can be modeled in terms of a Langmuir-Freundlich isotherm. Hence, we have

$$\theta_{Nip} = \frac{(K_{Nip}c_{Nip})^n}{1+(K_{Nip}c_{Nip})^n + K_{Hx}c_{Hx}+K_{BH4}c_{BH4}} \qquad (2.3.2.1)$$

where $K_{Nip}$, $K_{Hx}$, and $K_{BH4}$ are the Langmuir adsorption constants of the respective compounds, and $n$ is the Langmuir-Freundlich exponent. In reference[121, 122] $n$ was found to be 0.6. Based on the assumption[121, 122] that only adsorbed compounds can react, the reaction proceeds in two steps termed *A* and *B*: First nitrophenol is reduced to hydroxyaminophenol in step *A*. The reduction of the latter compound is done in step *B*. Hence, the rate of reaction of 4-nitrophenol follows as

$$-\frac{dc_{Nip}}{dt} = k_{app}c_{Nip} = k_A S\theta_{Nip}\theta_{BH4} = \frac{dC_{Hx}}{dt} \qquad (2.3.2.2)$$

where *S* denotes the total surface of all nanoparticles in the solution. This equation follows directly from the fact that $S\theta_{Nip}$ is proportional to the number of all adsorbed molecules in the system while $\theta_{BH4}$ denotes the conditional probability to find an adsorbed surface hydrogen atom near to an adsorbed nitrophenol molecule. As a tacit assumption in the entire LH-kinetics, the total number of adsorbed molecules is much smaller than the total number of molecules of a given species in solution, that is, adsorption on the surface of the catalyst does not shift the concentration in the system in a detectable way. Moreover, it is assumed that the equilibrium between the solution and the surface of the catalyst is established quickly.

Given these assumptions and prerequisites, the reaction rate for step A follows as

$$-\frac{dc_{Nip}}{dt} = k_A S \frac{(K_{Nip}c_{Nip})^n K_{BH4}c_{BH4}}{\left[1+(K_{Nip}c_{Nip})^n + K_{Hx}c_{Hx}+K_{BH4}c_{BH4}\right]^2} = \frac{dc_{Hx}}{dt} \qquad (2.3.2.3)$$

The intermediate 4-hydroxyaminophenol thus generated is further reduced to the final product 4-aminophenol in step B and its rate of decay may be formulated through

$$-\frac{dc_{Hx}}{dt} = k_B S \frac{K_{Hx}c_{Hx} K_{BH4}c_{BH4}}{\left[1+(K_{Nip}c_{Nip})^n + K_{Hx}c_{Hx}+K_{BH4}c_{BH4}\right]^2} = \frac{dc_{amp}}{dt} \qquad (2.3.2.4)$$

A brief qualitative discussion of these equations can be conducted as follows: First of all, it is demonstrated in references[121, 122] that $k_A >> k_B$. Hence, 4-hydroxyaminophenol is formed rather quickly but its further reduction in step *B* is much slower. When its concentration rises quickly in the early stage of the reaction, it will more and more compete with nitrophenol for the surface places of the nanoparticles and thus slow down the rate of reaction.

The full rate equation for the intermediate hydroxyaminophenol can be obtained by simultaneous numerical solution of Eqs. (2.3.2.3) and (2.3.2.4) with

$$\frac{dc_{Hx}}{dt} = k_A S \frac{(K_{Nip}c_{Nip})^n K_{BH4}c_{BH4}}{\left[1+(K_{Nip}c_{Nip})^n + K_{Hx}c_{Hx}+K_{BH4}c_{BH4}\right]^2} - k_B S \frac{K_{Hx}c_{Hx} K_{BH4}c_{BH4}}{\left[1+(K_{Nip}c_{Nip})^n + K_{Hx}c_{Hx}+K_{BH4}c_{BH4}\right]^2}$$

(2.3.2.5)

This procedure leads to the concentration of nitrophenol $c_{Nip}$ as a function of time that can be directly compared with the experimental data.

This analysis has been successfully applied to the reduction of 4-nitrophenol in different catalytic systems, including spherical polyelectrolyte brushes (SPB) stabilized Au, Pd nanoparticles[112] and Au/Pd nanoalloys,[113] as well as the ligand free Au nanoparticles.[114]

However, the full kinetics has not been studied with the reaction catalyzed in complex nanoreactors. The influence of the complicated structures on the reaction is of great interest. This thesis will for the first time study the kinetics of the reduction of 4-nitrophenol catalyzed in the polydopamine@gold nanoreactors with interconnected pore structure. The data obtained can be compared to the reported systems as mentioned.

## 2.4 Metal oxide particles as cathode materials for lithium-sulfur (Li-S) batteries

Metal oxide nanoparticles play a very important role in materials science. [123] They can adopt a number of structural geometries with an electronic structure, which can exhibit metallic, semiconductor or insulator character.[124] Using block copolymer as soft template to direct the synthesis of metal oxide materials is a major strategy for many researchers. For example, Wiesner et al.[125] have demonstrated a versatile approach using the soft template method to structure-direct transition metal oxides nanostructures. So far, they have synthesized different energy materials, including fuel cell electrodes, titanium dioxide electrodes for dye-sensitized solar cells, and titanium dioxide/carbon composite anode materials for lithium batteries.[126, 127]

For energy applications, high interfacial surface areas with controllable mesoscale pore size distributions are desirable in almost every energy conversion and storage device. Metal oxide nanoparticles with special porous structures are attracting growing interests. Using them as cathode host materials for lithium-sulfur battery is one of the most promising applications. Compared with commonly used porous carbon materials, which suffer significant decay upon long term cycling due to the weak interaction between (poly)sulfides and carbon,[128] metal oxide particles such as $TiO_x$, $SiO_2$ or $MoO_x$ with an internal void space were reported to exhibit prolonged cycling life owing to better sulfur confinement.[129-131]

### 2.4.1 Principles of the Lithium-Sulfur (Li-S) batteries

Sulfur is a promising positive electrode material for lithium batteries due to its high theoretical specific capacity of approximately 1675 mA h $g^{-1}$. The Gibbs energy of the Li/S reaction is ~2600 Whkg$^{-1}$, which is five times higher than the theoretical energy of a Li-ion system.[132, 133] Moreover, elemental sulfur possesses advantages such as natural abundance, low cost, excellent safety due to its intrinsic protection mechanism from overcharge, and its non-toxicity.[134-136] Thus, Li-S batteries have been considered as a promising candidate for next-generation electrochemical energy-storage technologies.

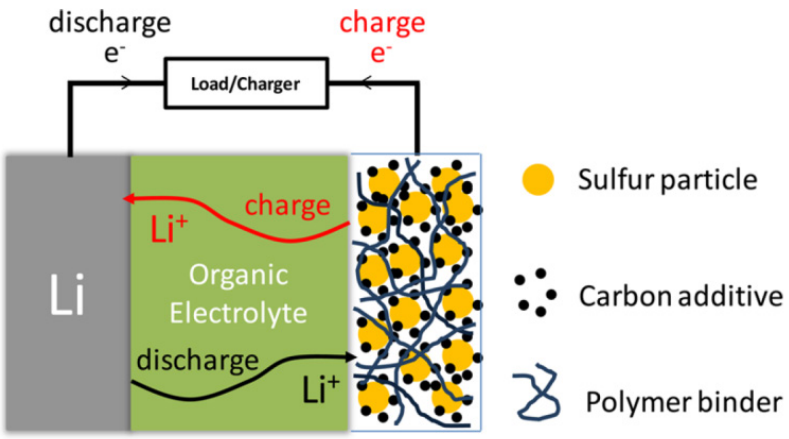


**Figure 2.4.1.1** Schematic diagram of a Li−S cell with its charge/discharge operations. [137]

A Li−S cell is an electrochemical storage device through which electrical energy can be stored in sulfur electrodes. Scheme 2.4.1.1 illustrates the components of a single Li−S cell and its operation (charge and discharge). A conventional Li−S cell consists of a lithium metal anode, an organic electrolyte, and a sulfur composite cathode. During the discharge reaction, lithium metal is oxidized at the negative electrode to produce lithium ions and electrons. The lithium ions produced move to the positive electrode through the electrolyte internally while the electrons travel to the positive electrode through the external electrical circuit, and thereby an electrical current is generated. Sulfur is reduced to produce lithium sulfide by accepting the lithium ions and electrons at the positive electrode.

Reduction of sulfur in a Li-S battery is a multistep electrochemical process that can be composed of different intermediate species. In general, lithium metal reacts with sulfur ($S_8$) to produce lithium polysulphides with a formula of $Li_2S_n$. Long chain polysulphides are produced first, such as $Li_2S_8$ and $Li_2S_6$, which are shortened during further reduction of sulfur. The final product of discharge is lithium sulfide ($Li_2S$) and the overall reaction is given by Eq. 2.4.1.1.[138]

$$16\,Li + S_8 \rightarrow 8Li_2S \quad (2.4.1.1)$$

In this process, sulfur accepts electrons from an open-circuit voltage (OCV) to 2.1 V, forming lithium polysulphide and then lithium polysulphide is reduced. From the viewpoint of phase transitions, the discharge can be divided into four stages, as follows:

I: Reaction of elemental sulfur with Li is given by:

$$S_8 + 2Li^+ + 2e^- \rightarrow Li_2S_8 \quad (2.4.1.2)$$

II: A reaction between dissolved $Li_2S_8$ and lithium is described as:

$$Li_2S_8 + 2Li^+ + 2e^- \rightarrow 2Li_2S_4 \quad (2.4.1.3)$$

III: A transition from the dissolved $Li_2S_4$ to insoluble $Li_2S_2$ or $Li_2S$ by the coexistence of Eqs. (2.4.1.4) and (2.4.1.5):

$$Li_2S_4 + 2Li^+ + 2e^- \rightarrow 2Li_2S_2 \quad (2.4.1.4)$$

$$Li_2S_4 + 6Li^+ + 6e^- \rightarrow 4Li_2S \quad (2.4.1.5)$$

IV: An equilibrium reaction of insoluble $Li_2S_2$ and $Li_2S$ is described as:

$$Li_2S_2 + 2Li^+ + 2e^- \rightarrow 2Li_2S \quad (2.4.1.6)$$

The theoretical capacities of lithium and sulfur are 3.861 and 1.672 $Ahg^{-1}$, respectively, which leads to a theoretical cell capacity of 1.167 $Ahg^{-1}$. The discharge reaction has an average cell voltage of 2.15 V. Hence, the theoretical gravimetric energy density for a Li–S cell is 2.51 $Whg^{-1}$.[140-144]

Eq. (2.4.1.3) is the most complicated reaction in the four stages. It is affected by both the solubility of the polysulphides and the chemical equilibrium in the electrolyte. Therefore, this reaction is affected strongly by the type of electrolyte solvents. The outcome of stage III depends on the competition of Eqs. (2.4.1.4) and (2.4.1.5). The final discharge products are mainly a mixture of $Li_2S_2$ and $Li_2S$. Eq. (2.4.1.5) shows the predominant reaction, the Li-S

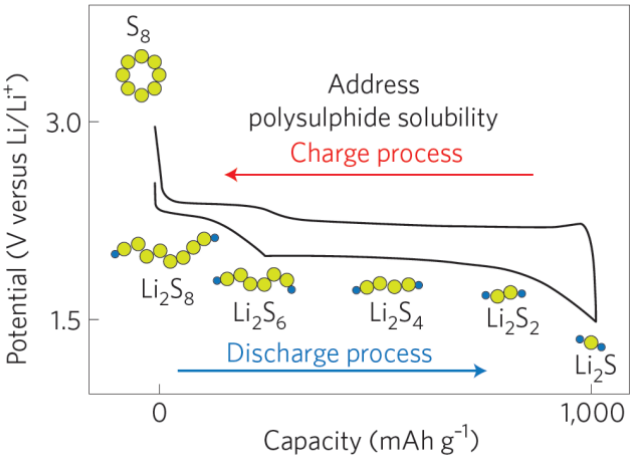


**Figure 2.4.1.2** Voltage profiles of a Li–S cell. Different stages of the reaction are illustrated corresponding to the discharge process.[139]

cell has high capacity with slightly lower discharge voltages. Stage IV is kinetically slow and suffers from high polarization because of the non-conductive nature of $Li_2S_2$ and $Li_2S$. Figure 2.4.1.2 shows the voltage profile of the discharge of a Li-S cell.[139]

### 2.4.2 Technical challenges

The Li−S technology is facing challenges both in materials and in the system. First of all, the high resistance of sulfur ($\sim 10^{-30}$ $Scm^{-1}$) and the intermediate products (lithium polysulfides $Li_2S_x$) formed during cycling along with their structural and morphological changes are formidable challenges, resulting in unstable electrochemical contact within sulfur electrodes. In addition, the dissolved polysulfides shuttle between the anode and cathode during cycling, reacting with both the lithium metal anode and the sulfur cathode.[145]Moreover, the electrochemical conversion of sulfur to lithium sulfide involves structural and morphological changes as well as repetitive dissolution and deposition of reactive species, which tend to passivate both the electrodes, leading to a significant increase in impedance. These issues result in a low utilization of the active material, poor cycle life, and low system efficiency.

As a result, the following issues need to be overcome to make Li−S batteries feasible:

(1) Capacity fading due to degradation of cell components in the harsh environment of the Li-S cell containing organic electrolytes, lithium metal anodes and reactive intermediates.[146, 147]

(2) The shuttle phenomenon where long-chain polysulfides diffuse to the anode and react to form shorter polysulfides, which diffuse back to the cathode (Figure 2.4.2.1). This polysulfide shuttle corrodes the lithium anode and contributes to self-discharge and low coulombic efficiency.[148, 149]

(3) Limited solubility of active species leads to variable internal resistance and increased parasitic mass in cell construction from binders. Both sulfur and its reduction product, lithium sulfide, are insulating and insoluble, resulting in chemical precipitation and dissolution towards the end of both charge (sulfur) and discharge (lithium sulfide) depending on voltage (Figure 2.4.2.1). During cycling this results in the losing of active material.[150]

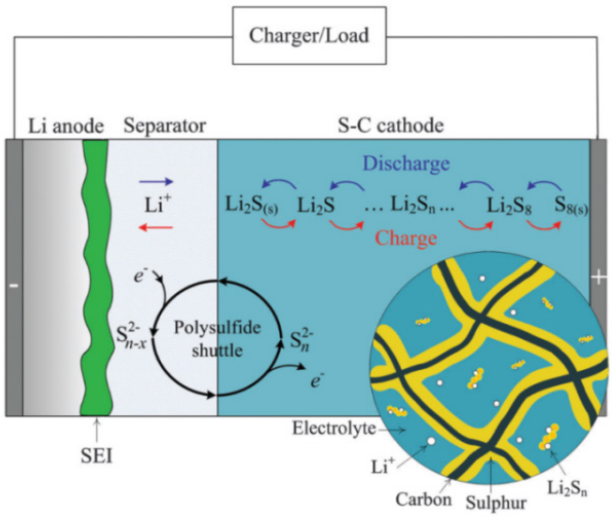


**Figure 2.4.2.1** Summary of the effects of polysulfide dissolution, shuttle phenomenon, effect on the cathode, insoluble products upon charge and discharge.[148]

Extensive attempts have been made to address the challenges highlighted in (1-3), including designing novel cathode architectures, use of solid-state electrolyte or polymer electrolyte to suppress polysulfide diffusion/migration, and the optimization of organic electrolytes.[151-155] The major efforts have been focused on the development of advanced sulfur cathodes including mesoporous carbon-sulfur composites, graphene-sulfur composites, conductive polymer-sulfur composites, metal sulfides-sulfur composites, and metal oxides-sulfur composites.[156-162]

Carbonaceous materials are the most widely used cathode materials. They are believed to confine sulfur and polysulfides within the pores or layers by physical interactions.[161] Although these carbon/sulfur composite cathodes exhibit high specific capacities during the initial cycles, they usually decay rapidly in the subsequent cycles. This problem is often attributed to the dissolution of the reaction intermediate polysulfides in the organic electrolyte. In fact, the weak physical adsorptions provided by the nonpolar carbon substrates could not efficiently suppress the dissolution of polar polysulfides during the whole charge-discharge cycling process.[73]

In contrast, it has been discovered that some metal oxides/sulfides with polar surfaces can form strong chemical bonds with the lithium polysulfide species. Metal oxides such as $TiO_2$, $SiO_2$, $Al_2O_3$ have been utilized as both adsorbents and coatings to hinder the diffusion of polysulfides by chemical interactions.[163-166] However, most metal oxides are not conductive

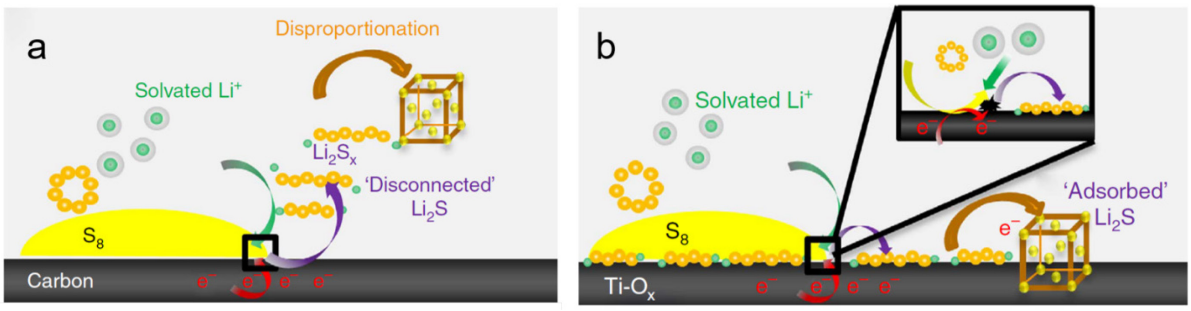


**Figure 2.4.2.2** Diagram illustrating surface-mediated reduction of $Li_2S$ from lithium polysulfides on $Ti_4O_7$. [73] (a) In reduction of $S_8$ on a carbon host, lithium polysulfides desorb from the surface and undergo solution-mediated reactions leading to broadly distributed precipitation of $Li_2S$. (b) In reduction of $S_8$ on the metallic polar $Ti_4O_7$, LiPSs adsorb on the surface and are reduced to $Li_2S$ via surface-mediated reduction at the interface.

and ultimately impede electron transport pathways, thus leading to low sulfur utilization and rate capability.

A practical way is to explore multifunctional sulfur host material that could combine the inherent metallic conductivity with the ability to chemically bind polysulfides. According to Nazar's pioneer work,[73, 167] a Magnéli phase titanium sub-oxides ($Ti_4O_7$) is demonstrated to fulfill this need. $Ti_4O_7$ is a member of the $Ti_nO_{2n-1}$ Magnéli phases, substoichiometric compositions of metallic titanium oxides that form a homologous series between the end members $TiO_2$ and $Ti_2O_3$.[168] $Ti_4O_7$ has been utilized as a Pt catalyst support for fuel cells because of its high electrical conductivity (>$10^3$ S $cm^{-1}$ at room temperature).[169, 170] Besides, $Ti_4O_7$ contains polar O-Ti-O units that have a high affinity for polysulfides, which is essential for retarding the dissolution of polysulfide.[73] Compared with typical carbon supports (Figure 2.4.2.2a), which do not adsorb the hydrophilic polysulphide intermediates or adhere well to $Li_2S$, the strong surface interactions play a larger role in inhibiting sulphide dissolution and deposition, rather than confinement that relies on physical barriers (Figure 2.4.2.2b). This will be particularly important for catholyte cells that will benefit from spatially controlled precipitation of sulphides and lowered charge potentials on charge.

Generally, $Ti_4O_7$ has been synthesized by thermal reduction of $TiO_2$ at about 1000 ˚C with inert gas and carbon.[171] This method in turn causes random growth of the particles, making it difficult to obtain complex nanostructures with high surface area. However, considering the high volume ratio of sulfur and polysulfides in the electrolyte, the commonly used anchoring powder would not be able to provide sufficient interfaces to fix all sulfide species. Addressing this limitation is a key point to obtain better electrochemical performance. The use of block

copolymer particles as template opens a new path for the synthesis of porous metal oxide particles with high surface area as well as complex inner structures. Owing to the ability of coordinating with different precursors of metal and metal oxides, the porous PS-P2VP particles are considered to be promising template for the synthesis of porous $Ti_4O_7$ particles. Reports of this kind have not been found yet.

In this thesis, I make efforts on exploring highly porous $Ti_4O_7$ nanoparticles as sulfur host materials. As discussed in chapter 1.3.2, the swelling induced porous block copolymer particles can be used as soft templates to direct the deposition of $Ti_4O_7$ precursors. Porous $Ti_4O_7$ particles with interconnected pores are expected to be generated by this approach, which will be tested as cathode materials for Li-S batteries.

# 3. Assembly of Palladium (Pd) and Dodecanethiol-gold (DT-Au) nanoparticles onto Poly(styrene-b-2-vinylpyridine) (PS-P2VP) nanospheres with ordered spatial distribution

The assemblies of metal nanoparticles with block copolymer (BCP) matrices have been intensively studied due to their potential applications in catalysis, sensors, optics and electronic devices.[172-177] The presence of well-ordered, high-content nanoparticles within BCP matrices offers the hybrid materials with enhanced collective properties, which do not present in their individual state.[178] For example, the assembly of plasmonic nanoparticles into secondary structures may create "hot spots" for surface-enhanced Raman scattering (SERS) due to the plasmon coupling between adjacent particles.[179] Different strategies have been developed for target-loading of metal nanoparticles into BCP nanostructures, including solution precipitation,[180-182] interfacial instabilities of emulsion droplets,[183] heating-cooling processing,[184] and directed supramolecular assembly.[185] However, most works of this sort have been reported on the assembly of one type of metal nanoparticles.[186-188] This is due to the limitation that few of block copolymers exhibit selective preferences to different metal nanoparticles.[181, 182] No report has been found on the assembly of two or more different types of metal nanoparticles to BCP particles with ordered spatial distribution. In addition to the types of metal nanoparticles, it is of great importance to control the loading efficiency of metal nanoparticles for practical device applications. Usually the interaction between the high-content metal nanoparticles and their favorable block of the BCP will increase its effective volume, resulting in breaking of the microphase separation structure.

In this chapter, a novel strategy based on the Rayleigh instability of polymer nanotubes confined in anodic aluminum oxide (AAO) nanopores has been applied to assemble two different types of metal nanoparticles onto block copolymer nanospheres with ordered distribution.[48] AAO with high density arrays of parallel nanopores has been widely used as template for the fabrication of one-dimensional (1D) nanostructures, such as nanotubes and nanorods.[189, 190] Rayleigh instability is used to describe the undulating phenomenon of liquid cylinders due to surface tension.[75] The Rayleigh instability of polymer melt inside AAO pores can generate short polymer rods, which can be applied as building blocks for the synthesis of block copolymer nanospheres with ordered nanostructure. When the mixture such as metal nanoparticles@polymer is injected into the AAO pores, short hybrid rods will be obtained due to the Rayleigh instability. Swelling of these short rods will result in hybrid nanospheres,

which can be used as spherical templates for the assembly of another type of metal nanoparticles.

In this part, I will demonstrate the assembly of two types of metal nanoparticles onto BCP nanoshperes with ordered distribution. The synthesis procedure of Pd@PS-P2VP@DT-Au nanospheres is illustrated in Scheme 3.1. Pre-synthesized Dodecanethiol-gold (DT-Au) nanoparticles[191] are first mixed with PS-P2VP and injected into the AAO nanopores to fabricate metal-polymer hybrid nanotubes (scheme 3.1, step 1). After drying, a thermal annealing induced Rayleigh Instability is applied to generate hybrid nanorods (scheme 3.1, step 2). These nanorods are released from the AAO membranes by dissolving in NaOH aqueous solution (scheme 3.1, step 3), and then cut into small segments through ultrasonication (scheme 3.1, step 4), followed by a swelling process to transform the short nanorods to nanospheres (scheme 3.1, step 5, 6). The P2VP domains of the nanospheres have the ability to form complexes with various metal ions. In the present study, $PdCl_4^{2-}$ ions are anchored in the P2VP domains and reduced to Pd nanoparticles (scheme 3.1, step 7).[192-194]

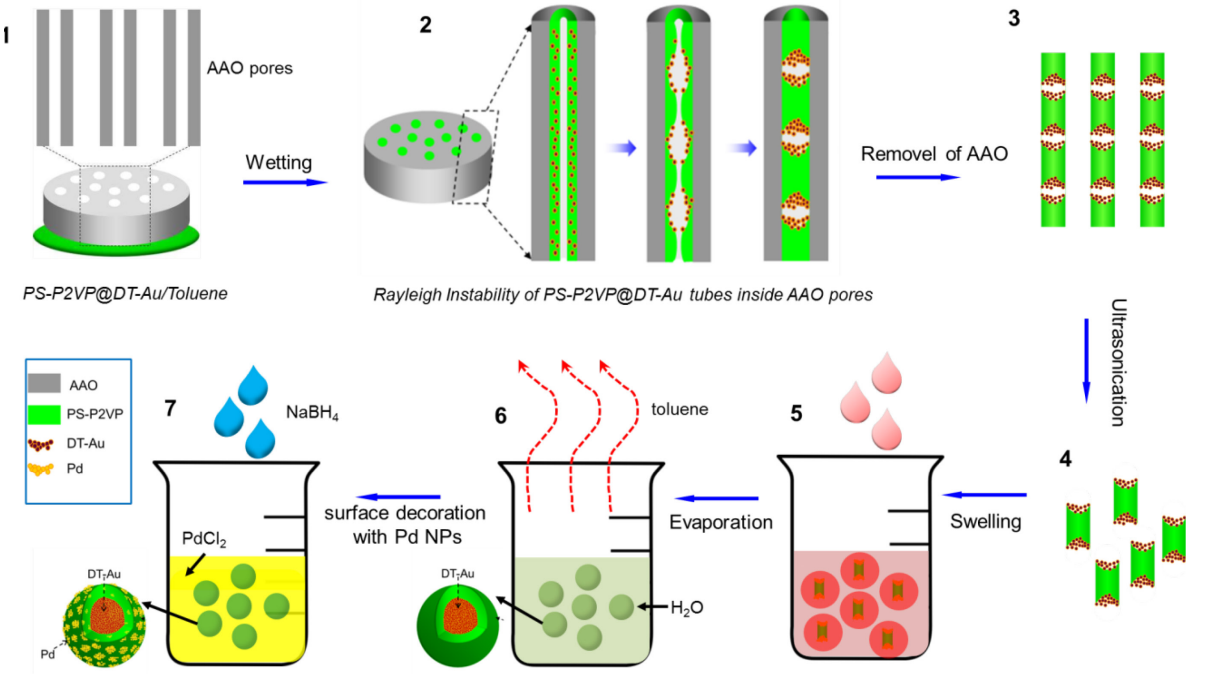


**Scheme 3.1** Procedure for the preparation of Pd@PS-P2VP@DT-Au particles based on Rayleigh Instability phenomenon of hybrid nanotubes in AAO capillary channels. (1) Wetting of AAO channels with PS-P2VP@DT-Au mixed solution. The molecular weight of the polymer is: $M_n$ (PS) = 50000 g/mol; $M_n$ (P2VP) = 16500 g/mol; $M_n/M_n$ = 1.06. (2) Rayleigh instability inside AAO channels accompanied with phase separation of PS-P2VP@DT-Au. (3) Dissolving of AAO template by NaOH aqueous solution. (4) Cutting the nanorods into short segments through ultrasonication. (5) Swelling by toluene in aqueous emulsion. (6) Evaporation of toluene. (7) Surface decoration of the core-shell particles with Pd nanoparticles.

## 3.1 Synthesis of DT-Au nanoparticles

In this work, Dodecanethiol modified gold (DT-Au) nanoparticles have been used for the assembly. Dodecanethiol has a hydrophobic alkyl chain and a -SH group (Figure 3.1.1), which makes it soluble in organic solvents and easy to be anchored to metal surface. The DT-Au nanoparticles with an average diameter of 4.1 nm are synthesized by a two-phase reaction procedure.[191] Figure 3.1.1shows the TEM image (Figure 3.1.1a) and the ultraviolet-visible (UV-vis) spectrum (Figure 3.1.1b) of the obtained DT-Au nanoparticles. The UV-vis spectrum shows a slight surface plasmon absorption at 497 nm, indicating the formation of quite small particles.[191] They have a mean diameter of 4.1 nm with a narrow size distribution (Figure 3.1.1c) according to the TEM image. In addition, no aggregation is found in the TEM image, indicating the protection of DT ligands at the surface of the Au nanoparticles, which prevents the growing of adjacent nanoparticles. The small size of the DT-Au nanoparticles is crucial for the injection of the mixture with PS-P2VP into the AAO channels. Because the mean diameter of the AAO pores is 200 nm, the pores can be easily blocked by bigger particles and their polymeric mixture.

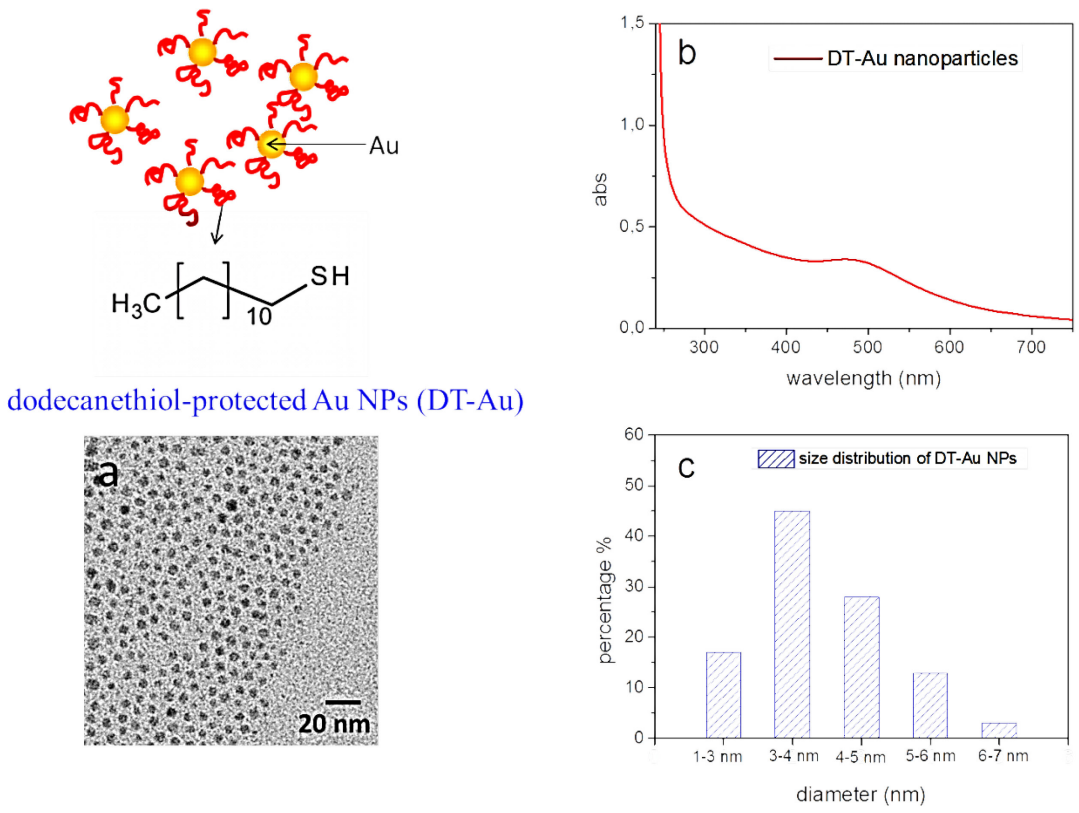


**Figure 3.1.1** TEM image (a), UV-vis absorption spectrum (b), and size distribution of the DT-Au nanoparticles (c).

## 3.2 Synthesis of PS-P2VP@DT-Au core-shell particles

Figure 3.2.1 illustrates the morphological evolution of the hybrid structures from PS-P2VP@DT-Au nanotubes to core-shell particles. Figure 3.2.1a is the TEM image of the PS-P2VP@DT-Au hybrid nanotube after removal of the AAO membrane. Two different contrasts can be observed between the outer and inner layer of the nanotube. The outer layer with low contrast is PS-P2VP due to the preferential interaction between the P2VP component and the hydrophilic AAO surface. The inner layer with high contrast is the DT-Au aggregation, which contains hydrophobic alky chains on the surface of Au nanoparticles. The hydrophobic DT-Au particles have poor interactions with the hydrophilic surface of the AAO wall, resulting in the phase separation to keep lower interfacial energy. The hybrid nanotubes confined in AAO channels are then thermally annealed above the glass transition temperature ($T_g$) of PS-P2VP to induce the Rayleigh instability. As shown in Figure 3.2.1b, nanorod structure with periodical encapsulated holes has been formed after thermal annealing, which is resulted from the undulation of the polymer tubes inside the AAO channels.

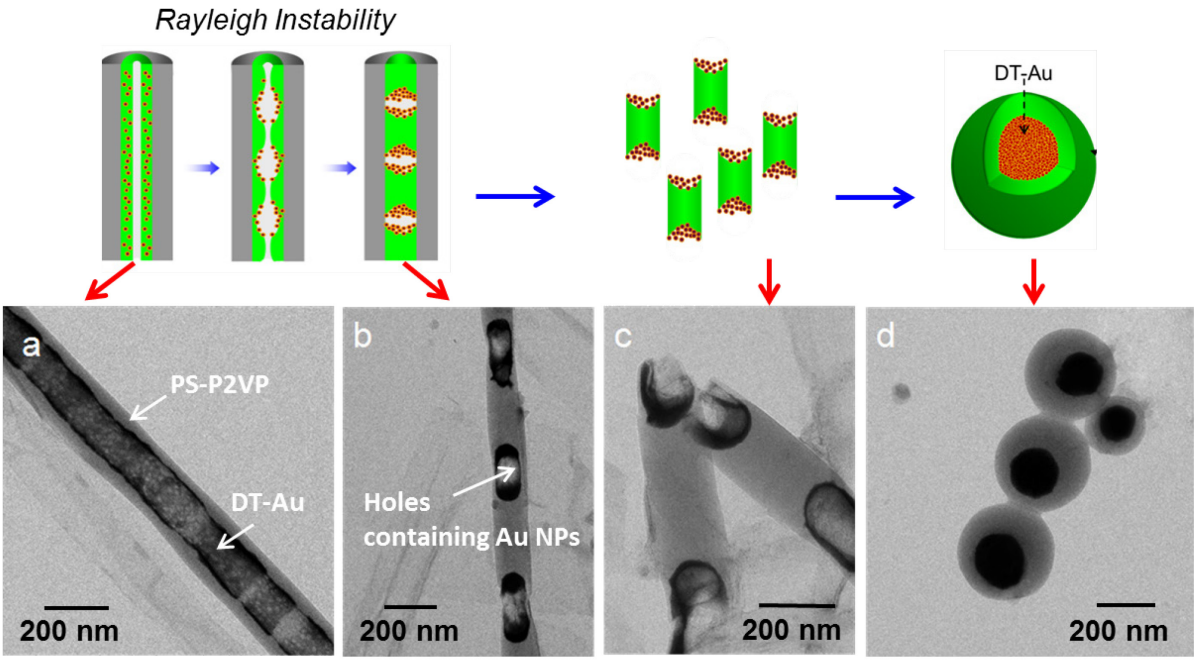


**Figure 3.2.1** Morphological evolution of the core-shell PS-P2VP@DT-Au particles from PS-P2VP@DT-Au hybrid nanotubes. (a) TEM images of PS-P2VP@DT-Au hybrid nanotubes after removal of the AAO membrane. (b) PS-P2VP@DT-Au nanorods with periodical encapsulated holes. (c) PS-P2VP@DT-Au nanoblocks obtained from ultrasonication of (b). (d) core-shell PS-P2VP@DT-Au particles after swelling of (c). The dark part is the aggregation of the DT-Au nanoparticles.

During the undulation of the tubes, the DT-Au nanoparticles tend to segregate to the trough and form periodic aggregations. This change of location caused by phase separation upon thermal annealing is led by the incompatibility of the PS-P2VP melt with the DT-Au nanoparticles. DT ($C_{12}SH$) is a short ligand compared with the $PS_{50000}P2VP_{16500}$ matrix. Densely packed $C_{12}SH$ ligands can be considered to form a relatively hard organic shell around the Au nanoparticles. These hard-spheres of DT-Au particles have unfavorable interaction with the PS-P2VP chains. Thus, the Au nanoparticles tend to be segregate to the trough, leading to the phase separation.

Figure 3.2.1c shows the broken segments of PS-P2VP@DT-Au, which are obtained from ultrasonication of the nanorods for 30 min. Here SDS (1 mg/ml) is added to form a stable aqueous dispersion. From the TEM images, PS-P2VP nanoblocks with DT-Au nanoparticles loaded at both ends (dark region) can be clearly observed. These blocks with a certain amount of DT-Au particles undergo a morphology evolution from anisotropic structure to isotropic core-shell spheres after being swollen by toluene, as shown in Figure 3.2.1d. During this swollen procedure, small amount of toluene is added into water under sonication and an oil-water emulsion is formed with SDS as surfactant. The hydrophobic DT-Au nanoparticles tend to be encapsulated by PS-P2VP due to the relatively stronger interactions between the P2VP blocks and water (the solubility parameters of P2VP, n-Dodecane and $H_2O$ are 21.7 $MPa^{1/2}$,[195] 16.0 $MPa^{1/2}$ and 48.0 $MPa^{1/2}$,[196] respectively). As discussed in chapter 2.1.2, the interaction between the blocks and the solvent can be indicated from the calculated value of $(\delta_{solvent} - \delta_{block})^2$. Relatively smaller value indicates stronger interactions.

This adjustment driven by the lowering of interfacial energy results in the core-shell structure with the aggregation of DT-Au nanoparticles as the core (Figure 3.2.1d) and the PS-P2VP layer as the shell. The final evaporation of toluene solidifies the core-shell structure of the PS-P2VP@DT-Au particles in aqueous solution.

Moreover, the size of the DT-Au nanoparticles before and after the morphology evolution has been studied. Miyake et al.[191] reported that DT protected Au nanoparticles underwent a size growing induced by thermal annealing. They showed that annealing at 150 °C for 30 min led Au nanoparticles grow from 1.5 nm to 3.4 nm in diameter. In our experiment, almost no change has been observed for the Au particle size before and after the annealing. As shown in Figure 3.2.2b, separated DT-Au particles can be clearly distinguished in the thermal annealed aggregation. This is because that the aggregated DT-Au nanoparticles are encapsulated in the

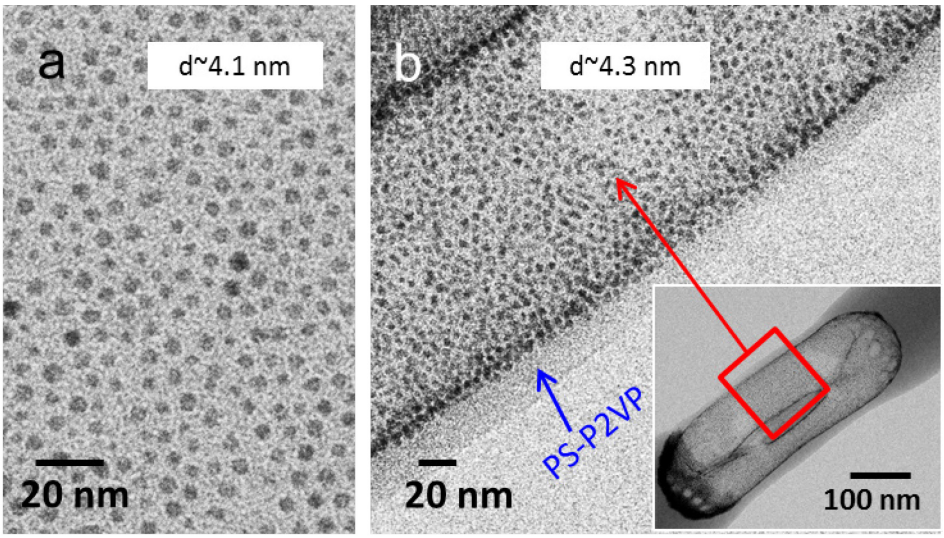


**Figure 3.2.2** DT-Au nanoparticles before (a) and after (b) the thermal annealing at 140 ℃ for 2 h. Inset: DT-Au nanoparticles trapped in PS-P2VP nanorods.

polymer phase and protected by the dodecanethiol groups, which effectively stabilize the Au nanoparticles and prevent the growing of the particles.

## 3.3 Tunable loading of different amounts of DT-Au nanoparticles

Until now, different methods have succeeded in loading metal nanoparticles to polymer nanostructures.[6, 45] However, it is still critical to control both the distribution and the loading content of the metal nanoparticles within the target polymer domains. In our study, the effect of DT-Au content on the morphology of the hybrid particles has been investigated. Different amount of DT-Au nanoparticles has been applied by keeping the BCP concentration constant.

Figure 3.3.1 displays the morphologies of the particles prepared with different amounts of DT-Au keeping the PS-P2VP amount constant (60 mg/ml). When 5 mg/ml of the DT-Au is mixed with the PS-P2VP, a thin layer of DT-Au nanoparticles can be found at the holes of the rod-like segments (Figure 3.3.1a). With the increase of the DT-Au content, larger aggregations of the DT-Au nanoparticles can be found at the holes of the rod-like structures. When the DT-Au content increases from 5 mg/ml to 20, 30 and 40 mg/ml, the corresponding radius of the DT-Au cores in the final spheres increases from 41 nm to 65, 115 and 180 nm, respectively (Figure 3.3.1 i-l). As shown in Figure 3.3.1l, when 40 mg/ml of the DT-Au nanoparticles is used, the DT-Au nanoparticles occupy most space of the polymer spheres and a very thin layer of polymer shell can be observed.

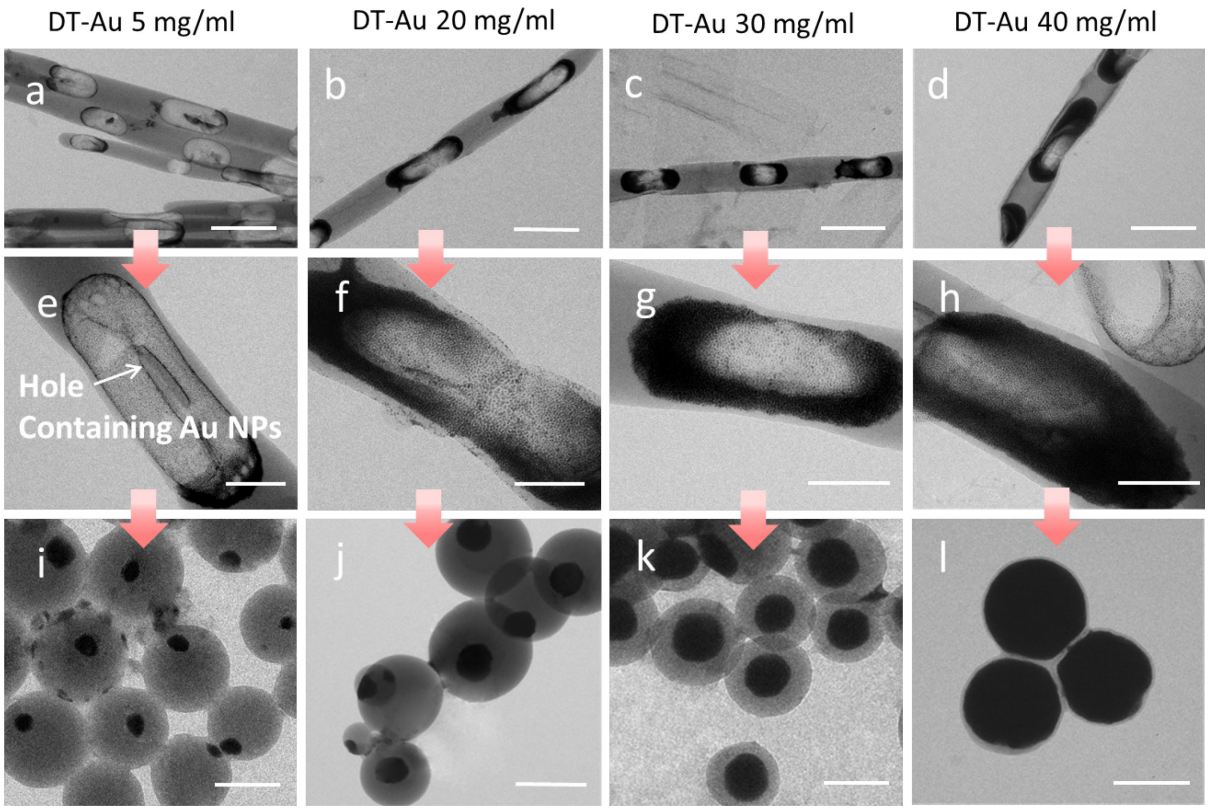


**Figure 3.3.1** TEM images of the PS-P2VP@DT-Au nanospheres with different DT-Au contents. (a-d) show the hybrid nanorods with periodic DT-Au aggregations inside, (e-h) are the images at high magnification. (i-l) show the final structure of the core-shell particles. The applied concentration of PS-P2VP is 60mg/ml, that of DT-Au nanoparticles is 5 mg/ml (a, e, i), 20 mg/ml (b, f, j), 30 mg/ml (c, g, k), and 40 mg/ml (d, h, l), respectively. Scale bars: (a-d, i-l) 300 nm; (e-h) 100 nm.

To make a quantitative analysis, the core size as well as the whole particle size are measured based on the TEM images. Figure 3.3.2a shows the change of the core size as a function of the DT-Au content, from which a clearly increasing trend of the core size with increased DT-Au content can be observed. Meanwhile, the size of the whole composite particle rarely changed for all samples. This is because of the confinement of the AAO channels where the Rayleigh instability occurs. As discussed in chapter 2.1.1, the size of the polymer short block is determined by the wavelength of the instability, which is proportional to the pore diameter of the channel confinement. In our experiment, the pore diameter is kept constant, thus the whole particle size shows no evident change upon the increase of the DT-Au content.

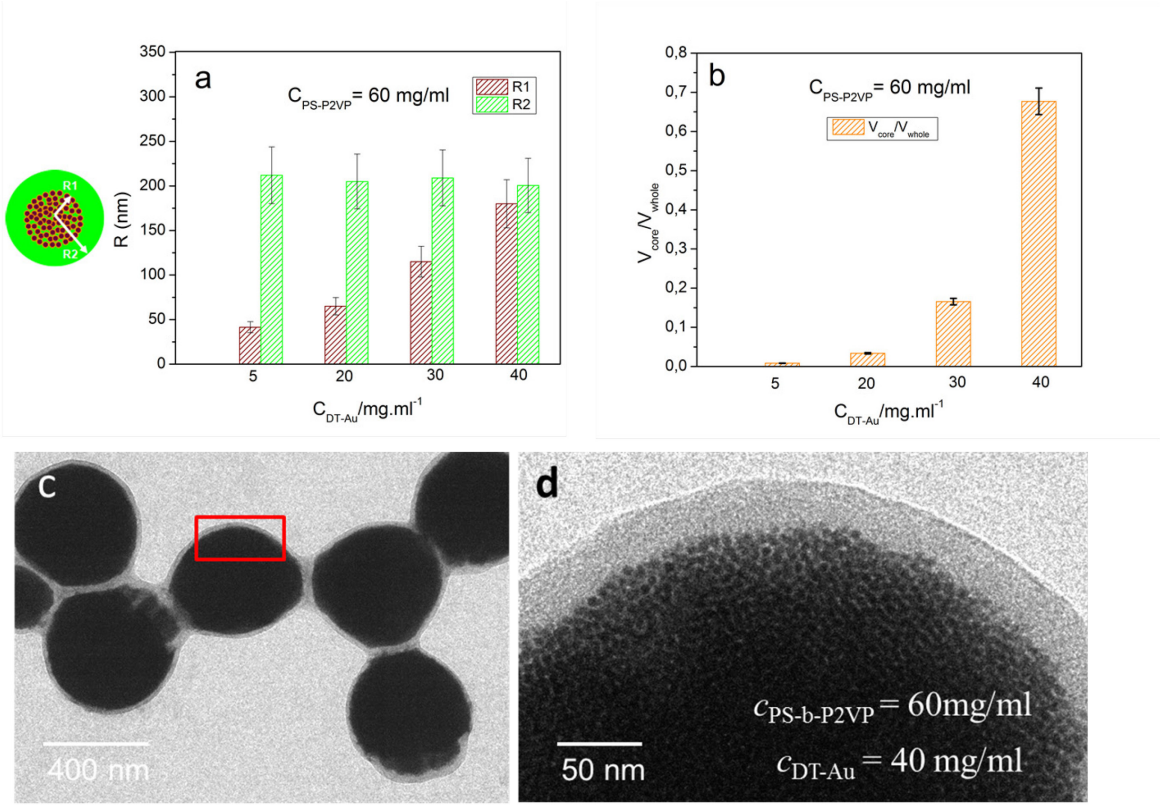


**Figure 3.3.2** (a) Average radius of DT-Au cores (R1) and polymer shells (R2) for samples prepared with different amounts of DT-Au nanoparticles. (b) Volume fraction of the DT-Au nanoparticles. (c) TEM images of PS-P2VP@DT-Au particles with a volume fraction of 0.73. (d) The single Au particle can be seen clearly in the PS-P2VP@DT-Au core-shell spheres at high loading ratio.

In order to directly present the loading effect, the volume fraction of the DT-Au nanoparticles in single hybrid nanosphere is calculated based on the core size and the whole particle size. For this calculation, the cores and the hybrid particles are assumed as spheres. The volume fraction can be obtained through the formula: $f_{DT-Au} = \frac{V_{core}}{V_{whole}} = (\frac{R1}{R2})^3$. Figure 3.3.2b shows that the volume fraction increases dramatically with the increase of the DT-Au content. A volume fraction of 0.73 is generated when 40 mg/ml of DT-Au is applied. It is worth noting that even at high loading ratio (0.73) the DT-Au nanoparticles remain keeping individual, no merging is found in the TEM images (Figure 3.3.2c, d).

## 3.4 The influence of the polymer concentration

The influence of the polymer concentration has been also investigated by keeping the DT-Au amount constant (20 mg/ml). As shown in Figure 3.4.1, an increase in the polymer concentration from 40 mg/ml to 60 and 90 mg/ml leads to a decrease in the core radius from

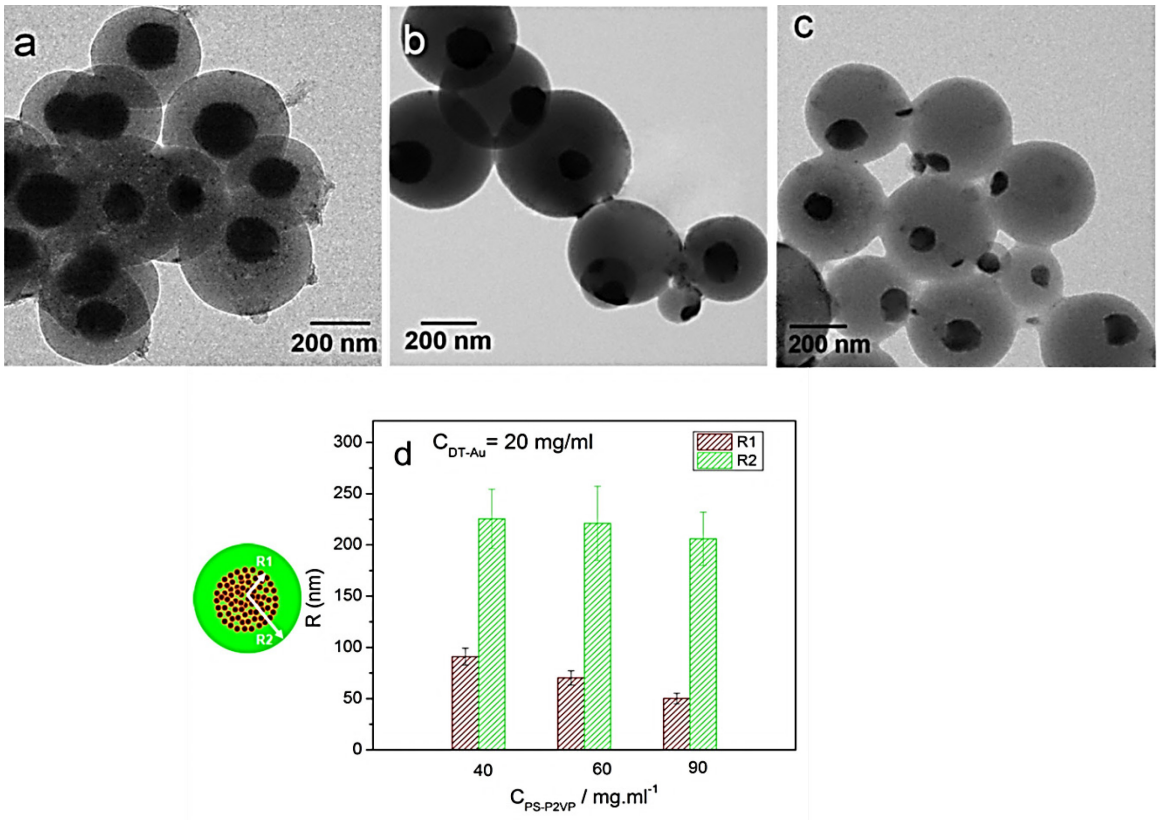


**Figure 3.4.1** TEM images of the PS-P2VP@DT-Au core-shell particles with different concentrations of polymer but constant concentration of DT-Au (20 mg/ml). $c_{PS\text{-}P2VP}$ = 40 mg/ml (a), 60 mg/ml (b) and 90 mg/ml (c), respectively. (d) Average radius of the DT-Au cores and the polymer shells for samples prepared with different concentrations of PS-P2VP.

83 nm to 70 and 51 nm, respectively. Because the volume of the wetting solution (PS-P2VP@DT-Au) and the quantity of the AAO membranes used in the experiment are the same, nanotubes with thicker walls have been produced at higher concentration of the polymers. During the undulation of the polymer film, smaller amplitude can lead to a bridge by the crest across the AAO channel. Thus, more polymer blocks can be generated, resulting in increasing of the total particle number after swollen in the toluene-water emulsion. In this way, the amount of DT-Au particles per nanosphere is reduced, exhibiting smaller core size.

## 3.5 Optical properties of PS-P2VP@DT-Au particles with different core sizes

With the increase of the DT-Au nanoparticles content, larger aggregations are formed in the core part. This process accompanies with a visible color change of the samples from gray pink to dark brown (Figure 3.5.1a). The surface plasmon resonance (SPR) absorption of the composite particles with different DT-Au core sizes is shown in Figure 3.5.1b. Compared

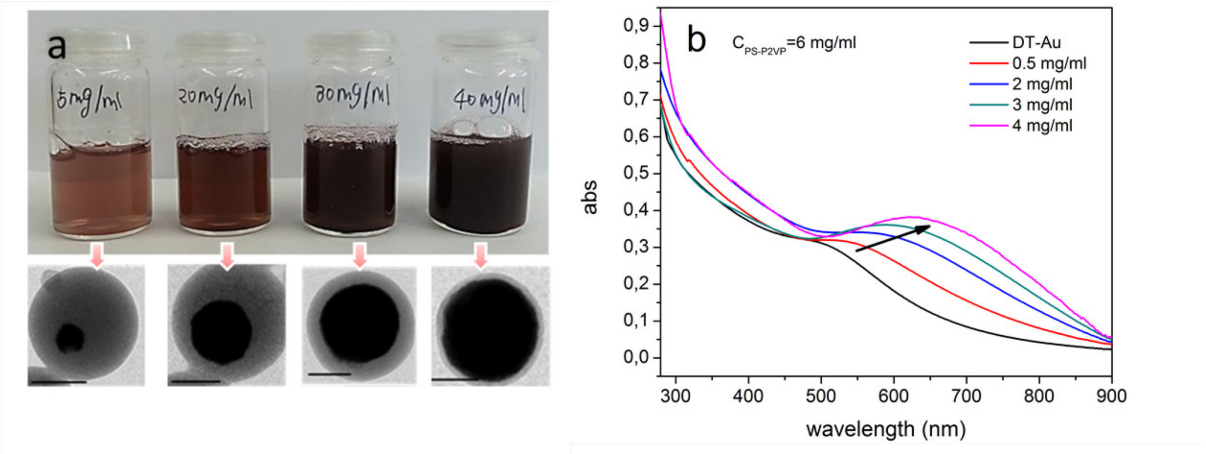


**Figure 3.5.1** (a) Color change of the PS-P2VP@DT-Au nanospheres with increasing core sizes. (b) UV-vis spectrum of the samples with constant amount of polymer but different amount of DT-Au nanoparticles. Scale bar in TEM images: 200 nm.

with the DT-Au nanoparticles (4.1 nm in diameter) which have the absorption band at 497 nm, a significant broadening and red-shift of the absorption band has been found for the PS-P2VP@DT-Ausamples. With the increase of the DT-Au core size from 41 nm to 65, 115 and 180 nm in radius, the surface plasmon absorption peak red shifts from 530 nm to 580, 600 and 630 nm, respectively. This is due to the reason that the aggregation of encapsulated Au nanoparticles leads to a decrease in the interparticle spacing, resulting in the occurrence of plasmonic couplings and therefore a red shift in the SPR peak.[197] Consequently, the plasmon absorption band is at relatively longer wavelengths for larger Au aggregate sizes with closely spaced nanoparticles.[198]

## 3.6 Decoration of the PS-P2VP@DT-Au core-shell particles with Pd nanoparticles

These core-shell structured PS-P2VP@DT-Au particles are good candidates for spatial organization of a second type of metal nanoparticles due to the ordered micropahse-separated structure of the polymer shell. Without staining of P2VP, no microphase structure can be seen in the core-shell PS-P2VP@DT-Au particles (Figure 3.6.1a). After staining with $I_2$, the ordered microphase separation structure can be obviously observed (spherical, Figure 3.6.1b). This indicates that the introduction of DT-Au nanoparticles into polymer solution has no influence on the microphase separation of PS-P2VP. Because the PS-P2VP shell contains pyridine units, various types of metal precursors (i.e. $HPt_2Cl_6{\cdot}6H_2O$, $AgNO_3$ and $H_2PtCl_4$) can be coordinated with them, which leads to the assembly of a second metal nanoparticles by an *in-*

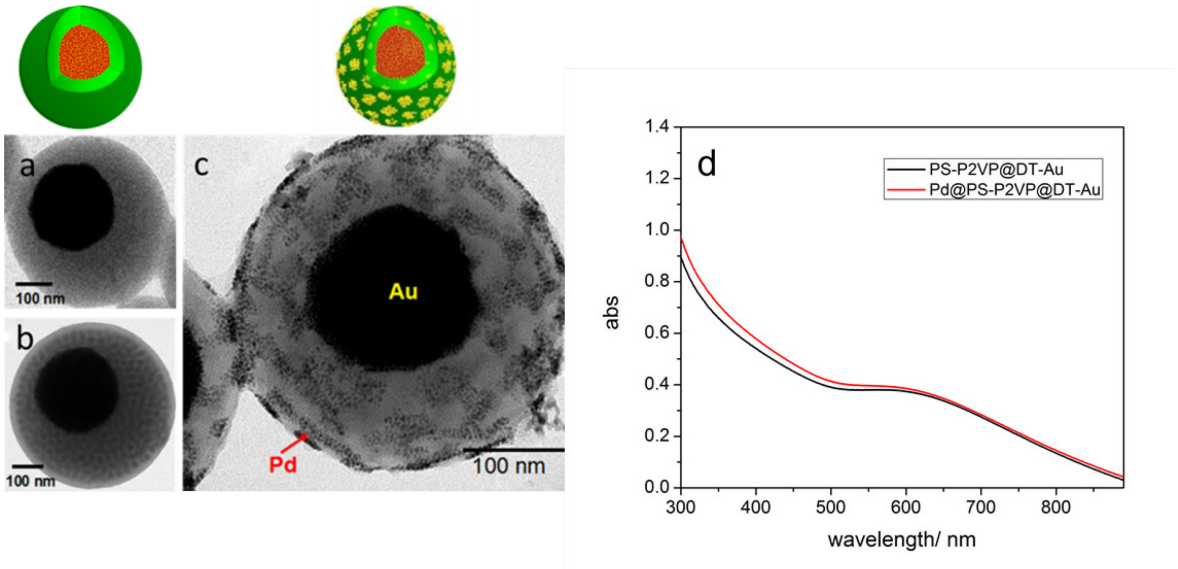


**Figure 3.6.1** TEM images of the PS-P2VP@DT-Au particles (a, b) before (a) and after (b) staining. The darker dots are P2VP domains which are stained with $I_2$ vapor. (c) Pd decorated core-shell PS-P2VP@DT-Au spheres. (d) UV-vis spectrum of PS-P2VP@DT-Au and Pd@ PS-P2VP@DT-Au particles.

*situ* reduction process. As shown in Figure 3.6.1c, Pd nanoparticles with diameter of 3 nm have been selectively distributed in the P2VP domains. The regular spaces between the adjacent Pd domains should be the PS phase. As a result, the DT-Au aggregations and the ordered Pd nanoparticles were selectively assembled at the core part and the shell part of the composite particles, respectively. Moreover, no shift was found in the UV-vis spectrum after Pd deposition (Figure 3.6.1d), indicating that further loading of Pd nanoparticles did not affect the characteristic absorption of the PS-P2VP@DT-Au particles.

## 3.7 Reduction of 4-nitrophenol using the Pd@PS-P2VP@DT-Au particles as catalyst

Pd nanoparticles are well-known as catalysts for reduction or coupling reactions. [109] In our study, the obtained Pd@PS-P2VP@DT-Au particles are further used as catalyst for the reduction of 4-nitrophenol by sodium borohydride. Figure 3.7.1 shows the UV-vis spectrum and kinetic analysis of the reduction of 4-nitrophenol. When Pd@PS-P2VP@DT-Au particles are used as catalyst, the characteristic absorption at 400 nm reduces with time due to the conversion of 4-nitrophenol. Another characteristic absorption at 300 nm appears and increases with time due to the generation of the end product, aminophenol (Figure 3.7.1a). In order to test which metal particle in the Pd@PS-P2VP@DT-Au composite particles contributes to the catalysis, the PS-P2VP@DT-Au particles have been also used as catalyst. In this case, no catalytic effect is found in the experimental time range (Figure 3.7.1b),

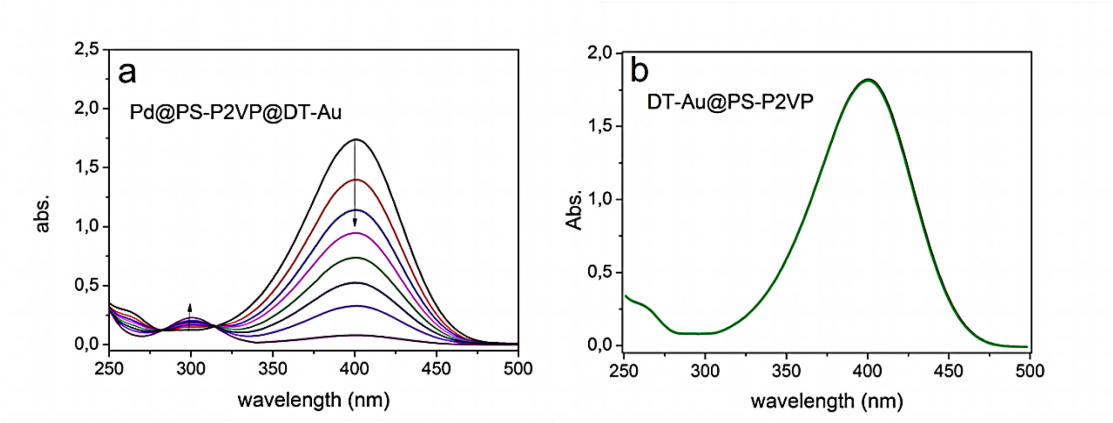


**Figure 3.7.1** UV-vis spectrum of the reduction of 4-nitrophenol using Pd@PS-P2VP@DT-Au (a) and PS-P2VP@DT-Au (b) as catalyst.

which demonstrates that the catalytic capability of the Pd@PS-P2VP@DT-Au particles arises only from the Pd nanoparticles. This is because that the DT-Au aggregations are encapsulated in the polymer shell, which blocks the diffusion of 4-nitrophenol to the metal surface. In addition, the DT ligands capped on the Au nanoparticles will also hinder the active site and weaken the catalytic activity.

As discussed in chapter 2.3, the reduction of 4-nitrophenol follows a pseudo-first order kinetic due to the excess of borohydride. The apparent rate constant $k_{app}$ is defined as: $\frac{-dc_t}{\mathrm{dt}} = k_{app}c_t$, where $c_t$ is the concentration of 4-nitrophenol at time $t$. Thus the apparent rate constant can be directly obtained from the curve of $\ln(A/A_0)$ versus time by a linear fit. As shown in Figure 3.7.2, a linear dependence of $\ln(A/A_0)$ on the reaction time can be observed when using Pd@PS-P2VP@DT-Au particles as the catalyst. The slope of this linear section leads to the apparent reaction rate ($k_{app}$), which is $1.72\times10^{-3}$ $s^{-1}$.

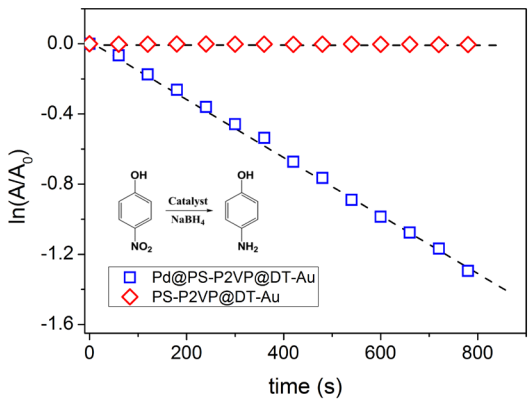


**Figure 3.7.2** Kinetic analysis of the reaction with Pd@PS-P2VP@DT-Au(squares) and PS-P2VP@DT-

Au(diamonds) as catalysts.

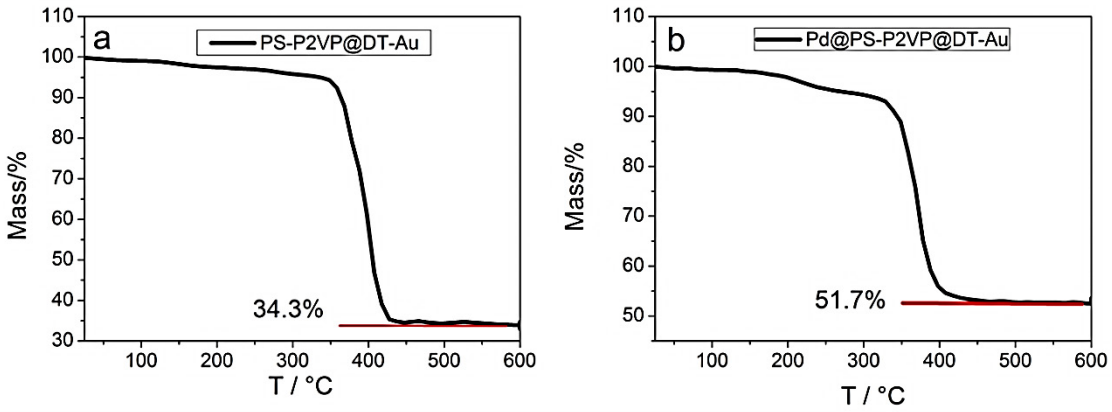


**Figure 3.7. 3** (a, b) TGA results of PS-P2VP@DT-Au, Pd@PS-P2VP@DT-Au (with 17.4 wt% Pd).

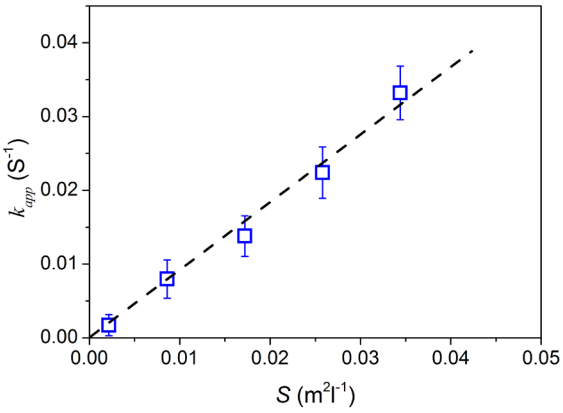


**Figure 3.7. 4** Apparent rate constant $\boldsymbol{k_{app}}$ as a function of the total surface area *S* of the Pd nanoparticles.

Based on the assumption that the reaction proceeds on the surface of the metal nanoparticles, $k_{app}$ should be proportional to the total surface *S* of the Pd nanoparticles present in the system:[109] $k_{app} = k_1 S$, where $k_1$ is the rate constant normalized to *S*. The total surface of the Pd nanoparticles *S* was estimated from the TGA results (Figure 3.7.3a, b) and the nanoparticles size was obtained from the TEM images. For this calculation, the Pd nanoparticles were assumed as spheres. From the linear fit we obtain $k_1$= 0.080 $s^{-1} \cdot m^{-2} \cdot L$ as shown in Figure 3.7.4.

Table 3.7.1 summarizes the catalytic activity of some reported Pd nanocatalysts with similar size for the reduction of 4-nitrophenol. Here the surface area-normalized rate constant, $k_1$, is applied for direct comparison. In general, the Pd@PS-P2VP@DT-Au composite particles show quite high catalytic activity compared to other reported systems. For example, it is higher than that of peptide,[199] protein,[200] and PAMAM dendrimer[201] stabilized Pd nanocatalyst

systems, but smaller than that of spherical polymer brushes (SPB) system.[111, 115] In addition, it is found that for the metal nanoparticles with similar size, the carrier system can have a strong influence on the rate constant of the immobilized nanoparticles. The present PS-P2VP block copolymer nanospheres act as efficient carrier systems for the immobilization of catalytic active Pd nanoparticles.

**Table 3.7.1** Catalytic activity of the metal nanoparticles for the reduction of 4-nitrophenol.

| Sample | Carrier system | Metal | D[a] (nm) | T [°C] | $k_1$[b] ($s^{-1}m^{-2}l$) |
|---|---|---|---|---|---|
| Pd@PS-P2VP@DT-Au[c] | PS-P2VP@DT-Au | Pd | 3.1±0.2 | 20 | 0.08 |
| Yuan 2012[115] | PS-PIL brushes | Pd | 2.1±0.2 | 20 | 0.58 |
| Mei 2007[111] | Cationic SPB | Pd | 2.4±0.5 | 15 | 1.1 |
| Esumi 2004[201] | PAMAM dendrimer | Pd | 1.8±0.4 | 15 | $3.07\times10^{-3}$ |
| Behrens 2009[200] | Protein | Pd | 2.8±0.5 | 22 | 0.048 |
| Bhandari 2011[199] | Petide | Pd | 2.6±0.5 | 20 | $1.67\times10^{-2}$ |

[a] D: Diameter of the metal nanoparticles
[b] $k_1$: Rate constant normalized to the surface of the particles in the system
[c] Pd@PS-P2VP@DT-Au: composite particles with 17.4 wt% Pd

In this work, we demonstrate a novel route to assemble two types of metal nanoparticles onto block copolymer nanospheres with ordered spatial distribution. PS-P2VP@DT-Au core-shell particles are first fabricated by swelling the short polymer rods containing periodic DT-Au aggregations, which are derived from Rayleigh instability of bilayered PS-P2VP@DT-Au nanotubes confined in AAO cylindrical pores. By using different amount of DT-Au nanoparticles, the core size can be adjusted directly. Moreover, the composite particles with larger DT-Au cores exhibit a red shift of the surface plasmon absorption band in the UV-vis spectrum. Because the PS-P2VP shell has highly ordered microphase separation structure, a second metal, Pd nanoparticles, have been successfully coated on the shell with patterned distribution, which can work efficiently as catalyst for the reduction of 4-nitrophenol. This study not only provides an effective approach for the sufficient location of different metal nanoparticles into polymer particles, but also demonstrates the functionalization of the polymer particles with optical and catalytic properties derived from two different metal NPs, respectively. Such multi-component nanomaterials will have potential applications in high-performance catalysis, bioengineering and medical therapy.

# 4. Polydopamine@gold (PDA@Au) nanoreactors with interconnected channel structure

Porous and hollow nanoparticles have been widely exploited in many applications, including catalytic support,[202] controlled release,[203, 204] confined synthesis,[205] optics and electronics,[206, 207] owing to their properties of low density, high surface areas, and interstitial hollow spaces.[208, 209] Extensive studies on porous nanoparticles have been conducted ranging from organic to inorganic materials.[210-214] Among them, nature inspired polymer nanoparticles stand out as competing candidates which exhibit better biocompatible and permeable properties in comparison with commonly used polymers.[215]

As a major pigment of naturally occurring melanin, PDA has received increasing attention due to its striking properties of naturally occurring melanin in optics, electricity and magnetics.[62, 216] In addition, because of its functional groups such as catechol, amine and imine, it can serve not only as the starting substrates for covalent modification with desired molecules but also as the anchors for the loading of transition metal ions, which can be applied for the synthesis of diverse hybrid materials.[217, 218] Compared with commonly used polymers, PDA presents better stability in organic solvents and aqueous solution. It has been demonstrated that PDA is stable between pH of 2-11 and in a large temperature range, as well as in many organic solvents, such as acetone, tetrahydrofuran (THF).[217, 218] Most importantly, PDA layers can be easily coated on virtually all types of inorganic and organic substrates with controllable thickness.[217, 218] Thus, PDA has opened a new route for the modification of various templates, which makes the soft-templating strategy extremely promising for the synthesis of PDA based nanoreactors.

Current studies on PDA nanoparticles have mainly yielded solid particles and closed capsules with limited functionality.[219, 220] Whereas complex nanostructures such as porous particles with separated nano-chambers in the interior have not been reported. In addition, a special class with encapsulated guest species such as metal nanoparticles has attracted tremendous interests as nanoreactors in recent years.[221-224] Reactions or behaviors of small molecules in nano-space are of great interest due to the templating and confining effects.[225]

As discussed in chaper 2 and chaper 3, block copolymer of PS-P2VP is a promising candidate for the soft template owing to its highly-ordered microphase separation structures. By choosing the appropriate molecular weight, porous PS-P2VP nanoparticles with tunable pore

sizes can be obtained through a selective swelling method.[12] Besides, P2VP has demonstrated good reducing ability for metal ions under UV irradiation,[45] which can be applied for the synthesis of metal nanoparticle for catalytic reactions.[226]

In this chapter, I will demonstrate a template-directed synthesis of PDA@Au nanoreactors with interconnected channel structure. Scheme 4.1 illustrates the synthesis procedure. PS-P2VP nanoparticles with ordered microphase structure are synthesized by an emulsion method, as stated in chapter 3. The porous templates can be prepared by a selective swelling process in ethanol (Scheme 4.1, step 1), after which Au nanoparticles are assembled onto the BCP framework through the *in situ* reduction of gold ions under UV irradiation (Scheme 4.1, step 2). Under alkaline condition (tris buffer, pH=8.5), a layer of polydopamine can be formed on the surface of the Au@PS-P2VP particles (Scheme 4.1, step 3). Owing to the permeable property of the PDA layer, the PS-P2VP template can be removed by THF, leading to the interconnected channel structure of the porous particles (Scheme 4.1, step 4). Electron tomography (ET) provides direct visualization of the complex inner structure, where Au

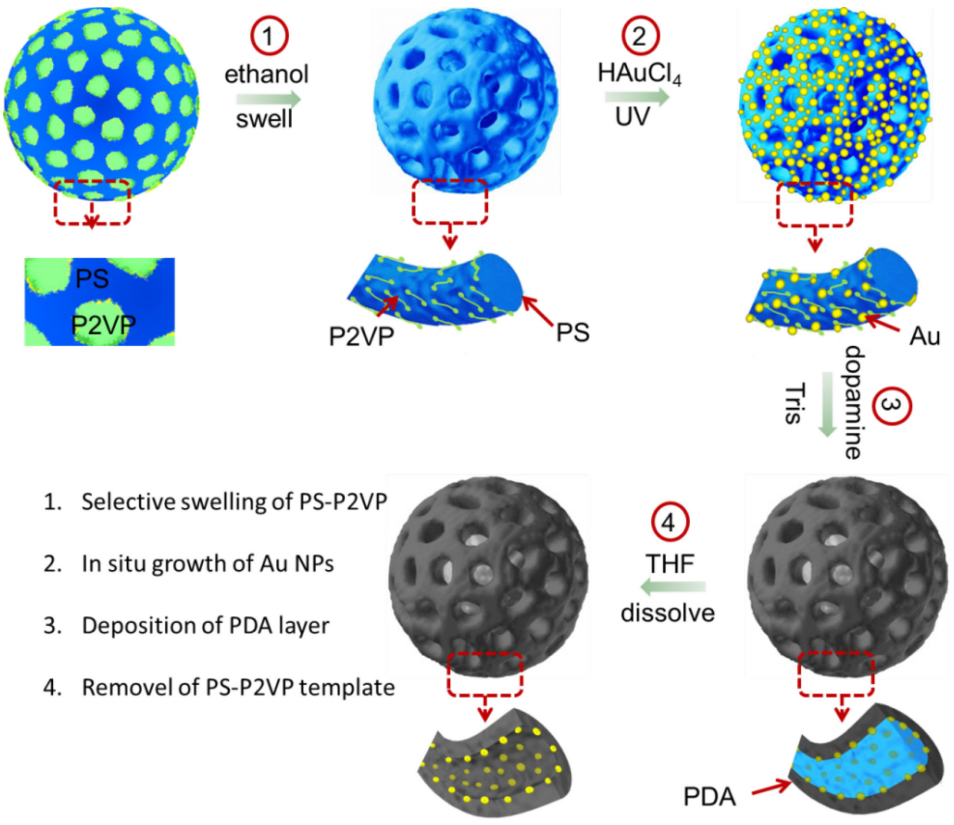


**Scheme 4.1** Synthesis of PDA@Au nanoreactors. (1) Selective swelling of PS-P2VP nanospheres into porous structures. (2) *In situ* growth of gold nanoparticles through UV irradiation. (3) Deposition of PDA layer onto the porous templates. (4) Removal of the PS-P2VP templates by dissolving in THF.

nanoparticles are homogeneously embedded. The obtained PDA@Au particles have been used as nanoreactors for the catalytic reduction of 4-nitrophenol. The kinetic data is simulated using a MatLab program and compared with other reported catalytic systems in detail. To the best of our knowledge, this is the first report on the synthesis of PDA@Au nanoreactors with interconnect channel structures.

## 4.1 Preparation of porous PS-P2VP nanoparticles as soft templates

PS-P2VP consists of swellable minority component P2VP and non-swellable majority component PS. Selective Swelling induced morphology reconstruction of PS-P2VP at temperatures below the Tg of PS (~100 ℃) will yield porous nanostructures, which can be used as soft templates for the synthesis of porous PDA nanoreactors. In this work, ethanol is used as swelling solvent because it is good solvent for P2VP but poor solvent for PS. Serving as soft templates, the particles are required to possess stable framework and open porous structure. Thus, PS-P2VP with different swelling ratios ($M_n$ (P2VP)/$M_n$ (PS)) is studied. It is found that perfect porous structure can be obtained when a moderate swelling ratio is applied ($M_n$ (P2VP) = 16500 g/mol, $M_n$ (PS) = 50000 g/mol, $\frac{\boldsymbol{M_{n\,(P2VP)}}}{\boldsymbol{M_{n\,(PS)}}} = \mathbf{0.33}$). As shown in Figure 4.1.1a, a nanosphere with porous network architecture is obtained. These particles not only keep the spherical shape but also exhibit open porous structure. Increasing the swelling ratio ($M_n$ (P2VP) = 10400 g/mol, $M_n$ (PS) = 23600 g/mol, $\frac{\boldsymbol{M_{n\,(P2VP)}}}{\boldsymbol{M_{n\,(PS)}}} = \mathbf{0.44}$), the resulted porous structure is fragile and easily collapsed (Figure 4.1.1b). While a relatively low

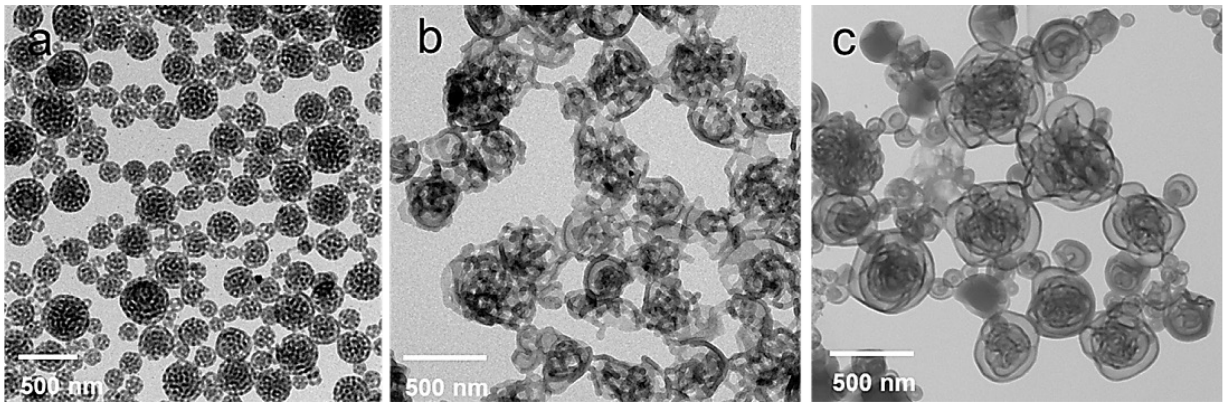


**Figure 4.1.1** Porous PS-P2VP particles with different swelling ratios (a) $M_n$ (P2VP) = 16500 g/mol, $M_n$ (PS) = 50000 g/mol; (b) $M_n$ (P2VP) = 10400 g/mol, $M_n$ (PS) = 23600 g/mol; (c) $M_n$ (P2VP) = 4800 g/mol, $M_n$ (PS) = 26000 g/mol.

swelling ratio ($M_n$ (P2VP) = 4800 g/mol, $M_n$ (PS) = 26000 g/mol, $\frac{M_{n\,(\mathrm{P2VP})}}{M_{n\,(\mathrm{PS})}} = 0.18$) results in closed multi-layer structures, which will block the functionalization of the inner part (Figure 4.1.1c). Thus $PS_{16500}$-$P2VP_{50000}$ has been chosen as the model polymer to produce the porous templates.

## 4.2 In situ growth of Au nanoparticles on PS-P2VP porous templates

PS-P2VP framework contains pyridine units, the N atoms with lone pair electrons can serve as electron donators. Various types of metal precursors can be coordinated with them, which can be further reduced to metal nanoparticles. In this work, PS-P2VP porous particles are dispersed in $HAuCl_4$/ethanol solution at room temperature to allow the coordination of the $AuCl_4^-$ ions with the protonated pyridine rings of P2VP through complexation. In order to avoid the formation of excess gold nanoparticles in the solution, the coordinated complex is separated from the free $AuCl_4^-$ ions by centrifugation. The adsorbed gold ions can be reduced into gold nanoparticles by exposing the composites under UV light irradiation for 4h. Figure 4.1.2a and b show the fully loading of gold nanoparticles onto the porous PS-P2VP templates. Further characterization by XRD demonstrates the formation of gold nanoparticles. As shown in Figure 4.1.2c, four diffraction peaks at 38.2°, 43.0°, 64.6° and 78.1° are assigned to the (111), (200), (220) and (311) planes of the face-centered cubic (fcc) Au, respectively.

### 4.3 Generation of PDA@Au nanoreactors

The primary advantage of PDA is that, which is similar with mussels, it can be easily deposited on both inorganic and organic substrates, including superhydrophobic surface. Catechol has been postulated to play an important role in this adhesion.[226] This adherence is

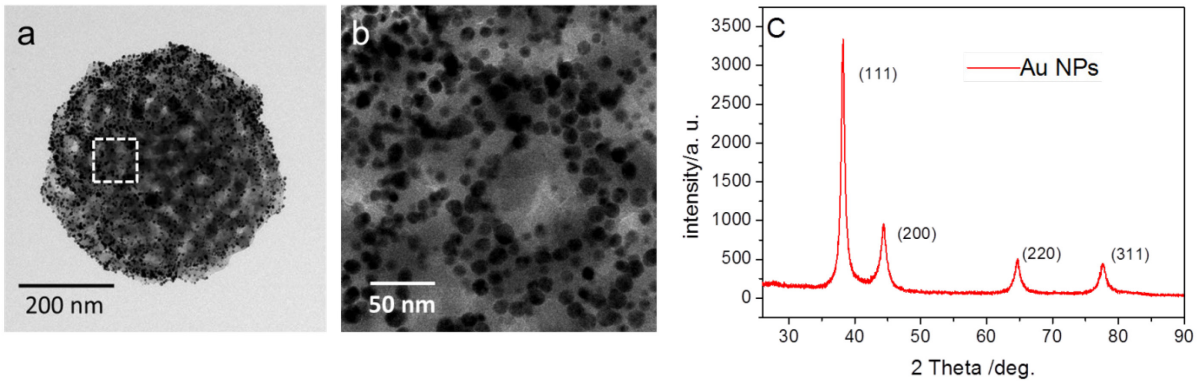


**Figure 4.2.1** (a) TEM images of the Au@PS-P2VP particles. (b) Selected area from image (a). (c) XRD spectra of the Au@PS-P2VP porous particles.

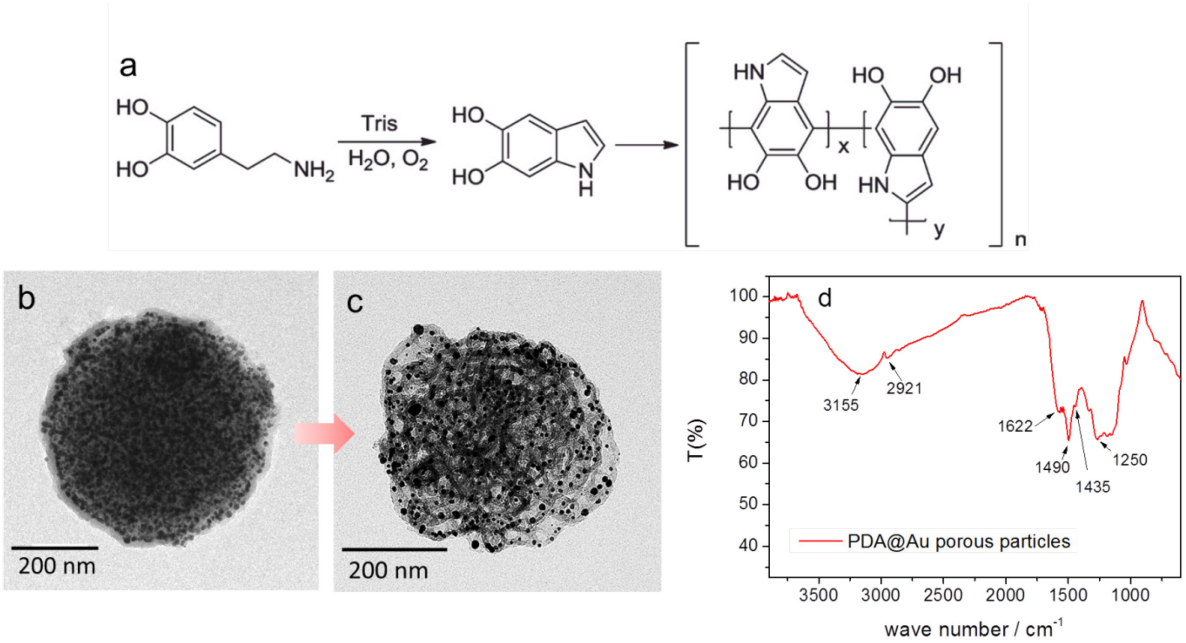


**Figure 4.3.1** (a) Synthesis and structure of PDA as proposed by Messersmith et al. [227] (b) TEM images of PDA@Au@PS-P2VP particles. (c) PDA@Au particles with interconnected channel structure after the removal of the PS-P2VP template. (d) FTIR spectra of the PDA@Au particles.

especially important for the trapping of Au nanoparticles, which is difficult for other polymers without introducing additional interactions. Another advantage is that dopamine can self-polymerize under weakly alkaline condition at room temperature (Figure 4.3.1a).[227] This mild condition successfully protects the porous structure of the PS-P2VP templates, which can be easily destroyed in organic solvents, acid solution, or temperature over 60 ˚C.

When dopamine monomers are added into an alkaline solution, the polymerization of dopamine monomers immediately occurs, coupled with a color change from colorless to pale brown, and finally turning to deep brown with reaction time. Figure 4.3.1b shows the PDA coated Au@PS-P2VP particles. We find the porous structure is no longer obvious. This is because PDA has the similar contrast with PS-P2VP, and the porous space is almost filled by the PDA layer. The final product of the PDA can be preliminarily verified by FTIR analysis. As shown in Figure 4.3.1d, the characteristic peaks located at 1490, 1435 and 1250 $cm^{-1}$ indicate the formation of polyphenoles structure.[228] The peak at 1622 $cm^{-1}$ is assigned to the stretching of aromatic C-C bonds of indole.

Figure 4.3.1c shows clearly that interconnected channel structure of PDA are generated after the removal of PS-P2VP. The gold nanoparticles originally formed on the PS-P2VP framework are fully trapped into the PDA channels. No aggregation of the gold nanoparticles

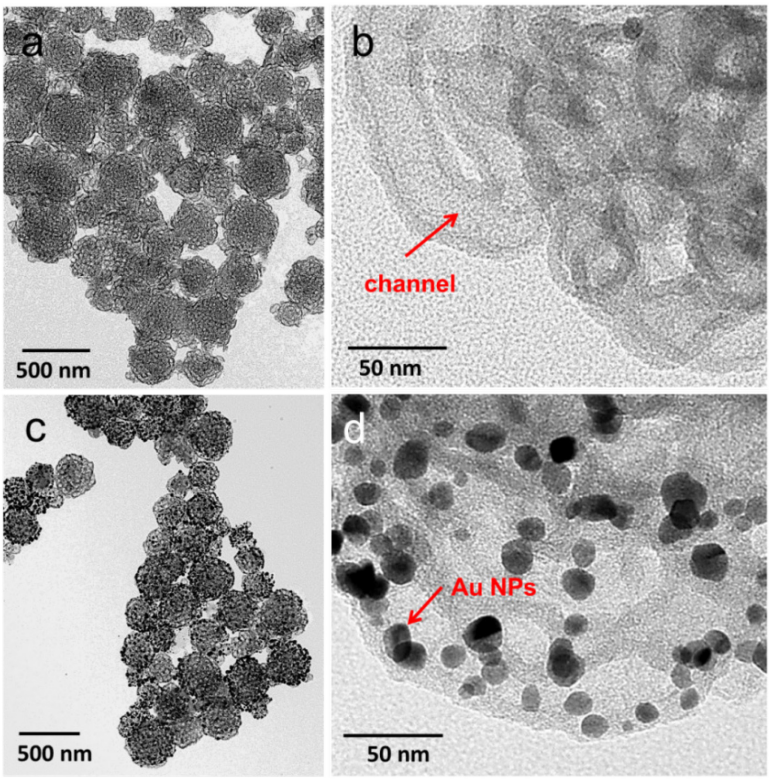


**Figure 4.3. 2** TEM images of the PDA particles without (a, b) and with (c, d) Au nanoparticles in the interior.

is found in the TEM picture, indicating that the PDA supporting layer can effectively avoid the merging of the Au nanoparticles.

Figure 4.3.2 shows the comparison of PDA porous spheres without (Figure 4.3.2a, b) and with gold nanoparticles (Figure 4.3.2c, d). The PDA channel structure can be clearly seen in Figure 4.3.2b, which is due to the replication of PDA from the PS-P2VP porous particles. In Figure 4.3.2d, gold nanoparticles with an average diameter of 10 nm can be observed in the hollow PDA channels. Owing to the good affinity of PDA to both organic and inorganic materials, the gold nanoparticles are totally embedded inside the channels.

## 4.4 Tuning the thickness of PDA layers

The physical stability of the PDA@Au scaffolds is especially important when they are applied as reusable nanoreactors, which is influenced by the thickness of the PDA layer. In my study, the thickness of the PDA layer can be controlled effectively by polymerization time. Different reaction times have been applied for the PDA coating process by keeping the PDA concentration constant (0.3 mg/ml). We found that PDA porous particles produced from reaction time of less than 4 h are fragile and significantly distorted upon centrifugation and sonication. Longer reaction time leads to the formation of PDA@Au porous particles with

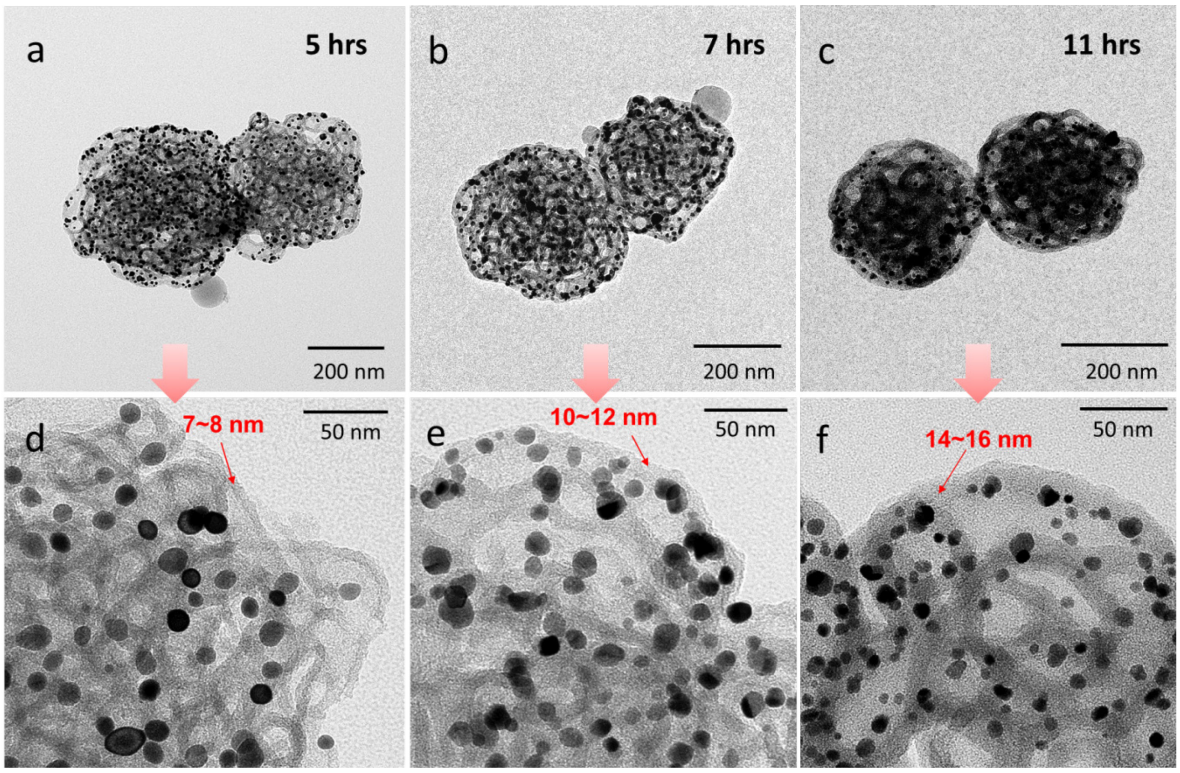


**Figure 4.4.1** PDA@Au porous particles with different thicknesses of the PDA layer by adjusting the reaction time. TEM images of the PDA porous particles produced from reaction time of 5 h (a, d), 7 h (b, e) and 11 h (c, f).

different wall thicknesses. As shown in Figure 4.4.1, increasing the polymerization time from 5 h, 7 h, to 11 h leads to the increase of PDA thicknesses from 7~8 nm, 10~12 nm to 15~18 nm. From TEM images with high magnification (Figure 4.4.1d, e, f), the uniform PDA layers can be clearly seen after removal of the PS-P2VP template, confirming the structural integrity of the porous particles.

## 4.5 Three dimensional (3D) visualization of the PDA@Au particles

To directly observe the 3D structure of the PDA@Au particles, a detailed structural analysis has been carried out by electron tomography (ET). ET is a powerful 3D visualization method for investigating the internal structure of the composite particles. In the tomographic acquisition, a set of projection images is recorded at different spatial orientations. The projections are subsequently computationally merged into a 3D image. A conventional TEM image (Figure 4.5.1a) shows the porous structure of the PS-P2VP template. Figure 4.5.1b is a gallery of selected XY slices through the tomographic reconstruction of the particle in Figure 4.5.1a. 3D surface renderings of the particle present both the surface and the internal structure

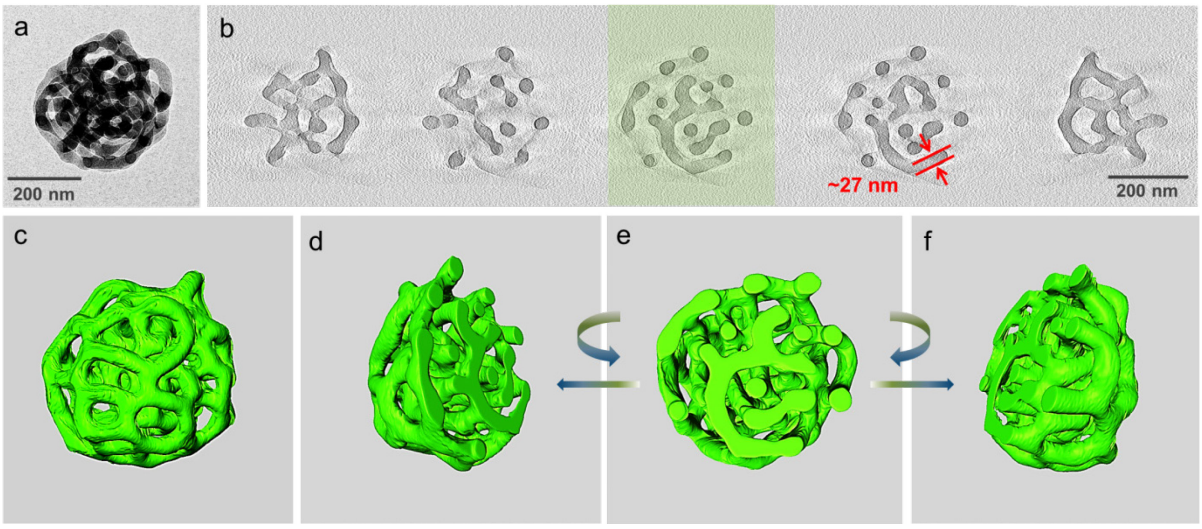


**Figure 4.5.1** TEM analysis of the PS-P2VP templates: (a) conventional TEM image and (b) selected XY slices through the tomographic reconstruction of an individual PS-P2VP porous particle. The slice in (b) highlighted in green corresponds to the central slice. (c-f) Particle 3D surface renderings without (c) and with interior views (d-f), using a cutting plane through the central XY slice (PS-P2VP shown in green).

of the PS-P2VP template (Figure 4.5.1c-e), where PS-P2VP micellar fibers (27 nm in width, measured in Figure 4.5.1b) form an interconnected network. Such highly porous structure provides super large surface for the deposition of PDA, which finally leads to interconnected channels after the removal of the template.

Figure 4.5.2a and 4.5.2b show the normal TEM image and selected XY slices through the tomographic reconstruction of the PDA@Au particles, respectively. The channel in Figure 4.5.2b is measured as 27 nm in width, which is the same as that of the PS-P2VP micellar fibers (Fig 4.5.1b). The channels are confirmed to be continuous inside the particles, which is attributed to the precise copy of the interconnected network of PS-P2VP micellar fibers by PDA and the subsequent removal of the template. Figure 4.5.2c shows the branches of the PDA channels. Au nanoparticles can not be observed from the surface view, while the cutting plane views (Figure 4.5.2d1-4, h, i) and the semitransparent views (Figure 4.5.2e-g) show that Au nanoparticles distribute all over the inner space of the particles, which demonstrates that Au nanoparticles are fully trapped in the PDA channels and distribute separately without obvious aggregation. Furthermore, Figure 4.5.2d2 and 4.5.2d4 clearly present the spatial distribution of the Au nanoparticles along the PDA channels. Enlarged views of selected regions (Figure 4.5.2j1, j2) clearly show the encapsulated Au nanoparticles inside the PDA channels. The 3D images are crucial in revealing the structural features of the particles which are not easy identified from normal TEM images which provide only 2D visualization.

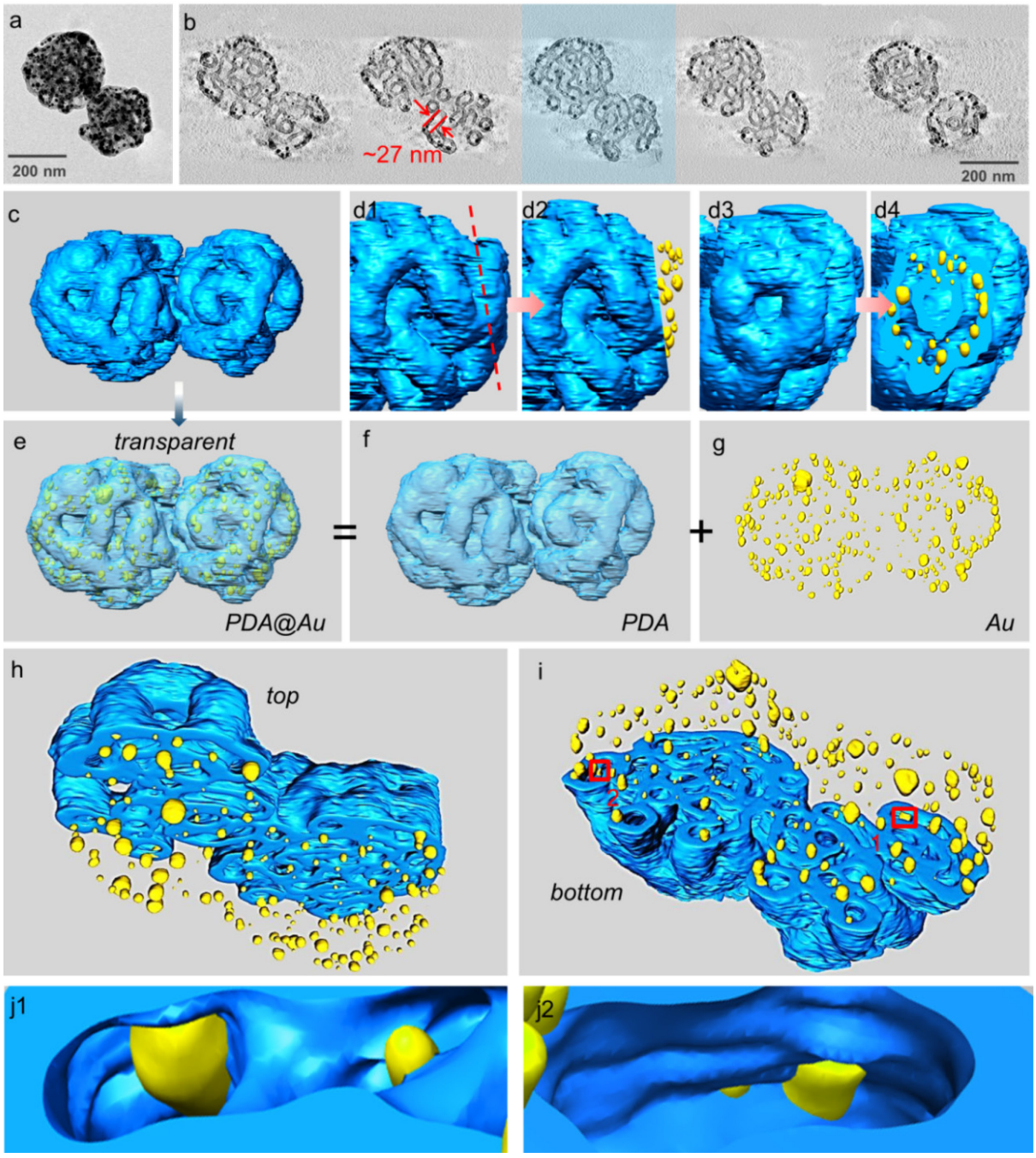


**Figure 4.5.2** TEM analysis of the PDA@Au particles: (a) conventional TEM image and (b) selected XY slices through the tomographic reconstruction of two adjacent PDA@Au particles. (c-i) 3D surface renderings of the particles (PDA shown in blue and Au shown in yellow): (c) surface view (d1, d2) subregion including cutaway view to highlight gold nanoparticles interior distribution in PDA. (d3, d4) rotated view of d1, d2 respectively. (e) as c but with semitransparent PDA layer to show internal structure. (f, g) as e but components shown separately. (h, i) as c but with a cutting plane through the central XY slice of PDA. (j1, j2) magnified views of selected marked regions in h.

## 4.6 Kinetic study of the reduction of 4-nitrophenol using PDA@Au particles as catalytic nanoreactors

### 4.6.1 Catalytic reduction of 4-nitrophenol in PDA@Au particles nanoreactors

The obtained PDA@Au particles have been used as nanoreactors for the kinetics study of reduction reactions. Apart from confining reactions into nanoscale volumes, PDA layers can also protect the encapsulated Au nanoparticles from aggregation, being poisoned or degraded by agents outside the containers, which is especially important for the reuse of the catalytic nanoreactors.

The catalytic reduction of 4-Nip by $NaBH_4$ is used as model system. The PDA@Au particles with PDA thickness about 8 nm are applied as catalytic nanoreactors (Figure 4.6.1.1). The size of the gold nanoparticles are measured based on the TEM images before and after coating with PDA (Figure 4.6.1.1a, b). No big change of the particle size is found in the size

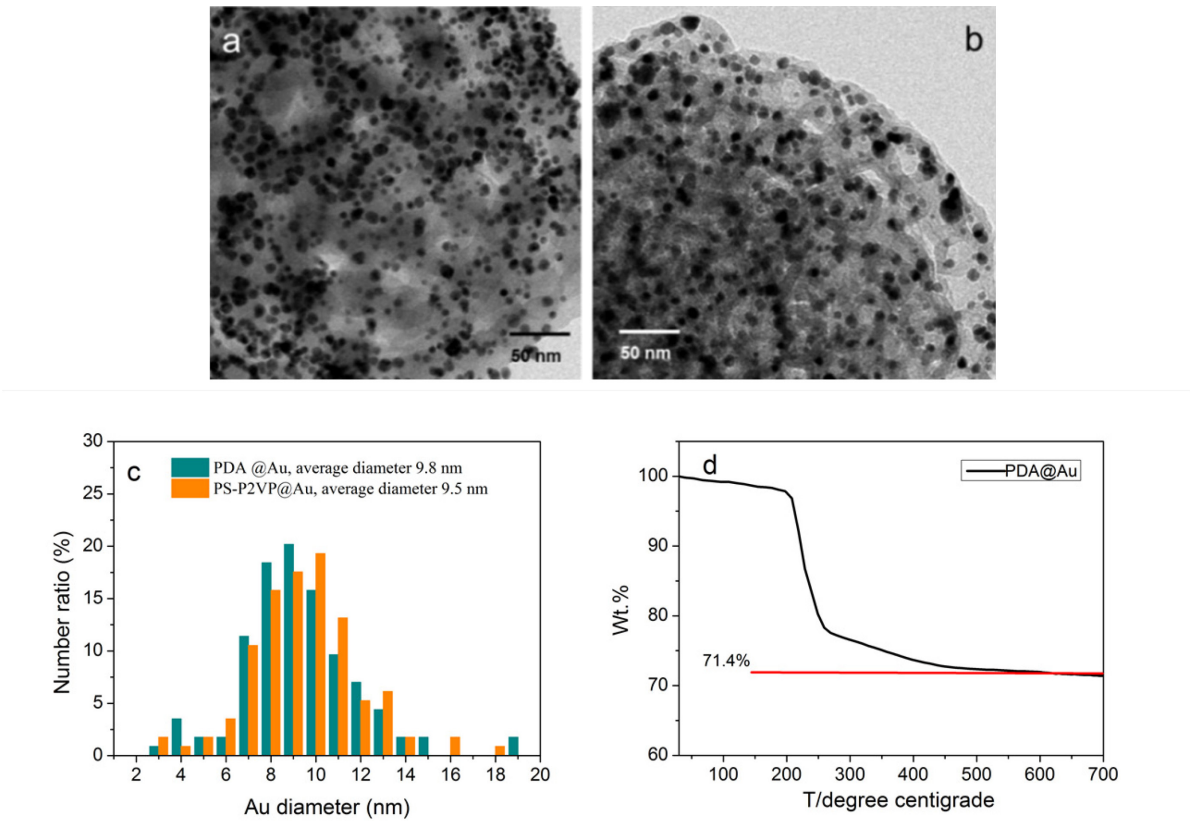


**Figure 4.6.1.1** Au NPs measured for the total surface area in the catalytic reactions. (a) Au NPs coated on PS-P2VP template; (b) Au nanoparticles embedded in PDA channels after the removal of PS-P2VP; (c) size distribution of Au NPs in (a) and (b); (d) TGA measurement of the PDA@Au shows the Au content up to 71.4%.

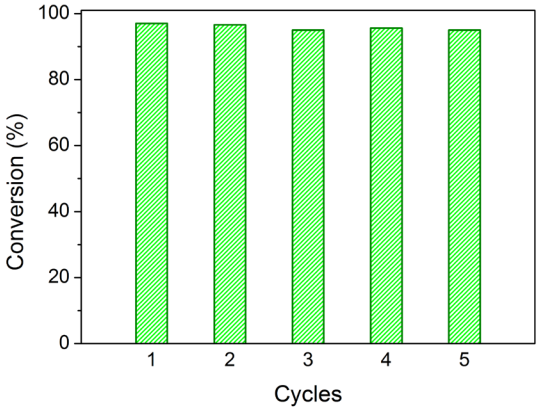


**Figure 4.6.1.2** Conversion efficiency of the PDA@Au catalytic nanoreactors in 5 consecutive reaction cycles. The repeated reactions run at a constant concentration of 4-nitrophenol 0.1 mM, $NaBH_4$ 10 mM, PDA@Au particles 15 mg/ml (50 µl) for 15 min.

distribution (Figure 4.6.1.1c). Then total surface area *S* is estimated from the TGA results (Figure 4.6.1.1d) and the average particle size. Langmuir-Hinshelwood kinetics[112, 115, 121, 122] is used for the mechanistic analysis of the catalytic activity. In chapter 2.3.2 we shows that 4-Nip is first reduced to 4-nitrosophenol and then to 4-hydroxylaminophenol (Hx). In the final step, Hx is reduced to 4-aminophenol (Amp). Figure 4.6.1.2 presents good reusability of the nanoreactors. After 5 repeated cycles, they show almost identical activities without obvious decreasing of the conversion.

### 4.6.2 Theoretic analysis of the surface-controlled reaction model

A simple analysis of the total reaction rate shows that in this system the reaction is surface-controlled. The reason is that the total catalytic time is much longer than that of the diffusive approach of the reactants to the dense layer of the nanoparticles.[229]

We define the total catalytic reaction time, $k_{tot}^{-1}$, is the sum of the time for the reactant 4-nitrophenol to diffuse to the gold nanoparticles in the PDA@Au nanoreactors, $k_D^{-1}$, and the time to get reduced by sodium borohydride $NaBH_4$ adjacent to a nanoparticle, $k_S^{-1}$, i.e.,

$$k_{tot}^{-1} = k_D^{-1} + k_S^{-1} \qquad (4.6.2.1)$$

Likewise, the diffusion time has two contributions: the diffusion from the bulk to the PDA@Au nanoreactor, $k_{D0}^{-1}$, and the diffusion from the outer surface of the PDA shell to the surface of a gold nanoparticle, $k_{Dg}^{-1}$, i.e. $k_D^{-1} = k_{D0}^{-1} + k_{Dg}^{-1}$. Since the density of gold nanoparticles in the nanoreactor is very large (see, e.g., Figure 4.5.2 ), according to the theory

for nanoreactors,[37] the rate limiting step in the diffusion approach (i.e. the slowest time) is the mean time to reach the nanoreactor from the bulk. Thus, the diffusion-controlled rate, $k_D$, is simply given by the Smoluchowski equation:

$$k_D \approx 4\pi D_0 R_0 c_{Nip,0} \qquad (4.6.2.2)$$

where $D_0$ is the diffusion coefficient of 4-nitrophenol in water, $R_0$ is the outer radius of the nanoreactor, and $c_{Nip,0}$ is the bulk concentration of 4-nitrophenol. If we make an order of magnitude analysis, considering $D_0 \sim 1$ nm$^2$/ns, $R_0 \sim$ (100-200) nm, and $c_{Nip,0} \sim 10^{-5}$ M (which is $\sim 10^{-5}$ nm$^{-3}$), we conclude that $k_D^{-1} \sim 10^{-7}$ s.

In addition, as shown in Figure 4.6.2.1, the apparent rate constant is, $k_{app} \sim 10^{-3}$ s$^{-1}$, which means that the total reaction time is $k_{tot}^{-1} \sim 10^{3}$ s. Since the total catalytic reaction time is approximately 10 orders of magnitude larger than the diffusion time, using Eq. (4.6.2.1) we clearly conclude that the reaction is surface-controlled.

We express the surface reaction rate $k_S$ as:

$$k_S = K_{vol} c_{Nip,g} \qquad (4.6.2.3)$$

where $c_{Nip,g}$ is the 4-nitrophenol concentration in the nanoreactor next to the gold nanoparticles, and $K_{vol} = k_{vol}\Delta V$, being $k_{vol}$ the fraction per unit time of the 4-nitrophenol

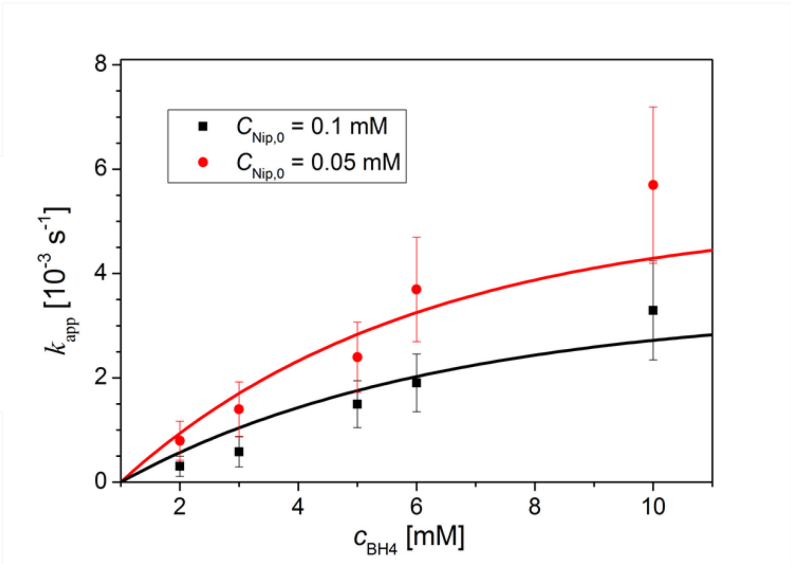


**Figure 4.6.2.1** Dependence of the apparent rate constant, $k_{app}$, with the borohydride concentration for different initial 4-nitrophenol concentrations. The solid lines refer to the fit of the experimental data obtained using, e.g., Eq. (3b) in Ref. 112.

molecules that are reduced by $NaBH_4$, and $\Delta V$ the volume of the shell next to the gold nanoparticles where effectively the chemical reaction is happening. As a consequence, the surface reaction is directly proportional to the 4-nitrophenol and $BH_4^-$ concentrations within the reactive volume. For large concentrations a competition of both reactants for reactive sites on the metal surface would lead to a saturation and a subsequent slowdown of the surface reaction rate.

We find such behavior in the total reaction rate, as shown in Figure 4.6.2.1. The apparent rate, $k_{app}$, increases linearly with increasing $BH_4^-$ concentration. The diminution of $k_{app}$ with increasing 4-nitrophenol concentration is due to the nearly full coverage of the nanoparticles surface by 4-nitrophenol, which slows down the injection of electrons to the metal surface. If the reaction would be diffusion-controlled, a modification of the $BH_4^-$ concentration would not affect the total rate. This fact supports our conclusion about the surface-controlled nature of the catalytic reaction.

### 4.6.3 Kinetic study of the reduction of 4-nitrophenol in PDA@Au nanoreactors

As discussed in chapter 2.3.2, the kinetic study follows a system of two coupled differential equations (Eqs. (2.3.2.3) and (2.3.2.5))[113, 114] which describe the two steps of the reduction. In the equations, $K_{Nip}$, $K_{Hx}$ and $K_{BH4}$ are the Langmuir adsorption constants of the respective compounds, and $k_a$, $k_b$ represent the reaction rate constants of step A and B. Eq. (2.3.2.3) describes the decay rate of Nip and the generation of Hx. Equation (2.3.2.5) presents the generation and decay of the intermediate Hx. The concentration of Nip as the function of reaction time was then calculated by the numerical solution of the equations as reported.[113]

As shown in Figure 4.6.3.1, the concentration of 4-Nip normalized by respective initial concentration $c_{Nip,0}$ was plotted as the function of time with different initial concentrations of 4-Nip and $BH_4^-$. The solid lines are the fits by theory. The experimental data can be well fitted even when the conversion reaches 70 %. Figure 4.6.3.2 displays the reaction rates of step A and B derived from the fitting results. As indicated by the dash lines, the rate constants $k_a$ and $k_b$ scatter around mean values within the limits of error. The whole set of kinetic and thermodynamic parameters are summarized and compared with reported systems in Table 4.6.3.1.

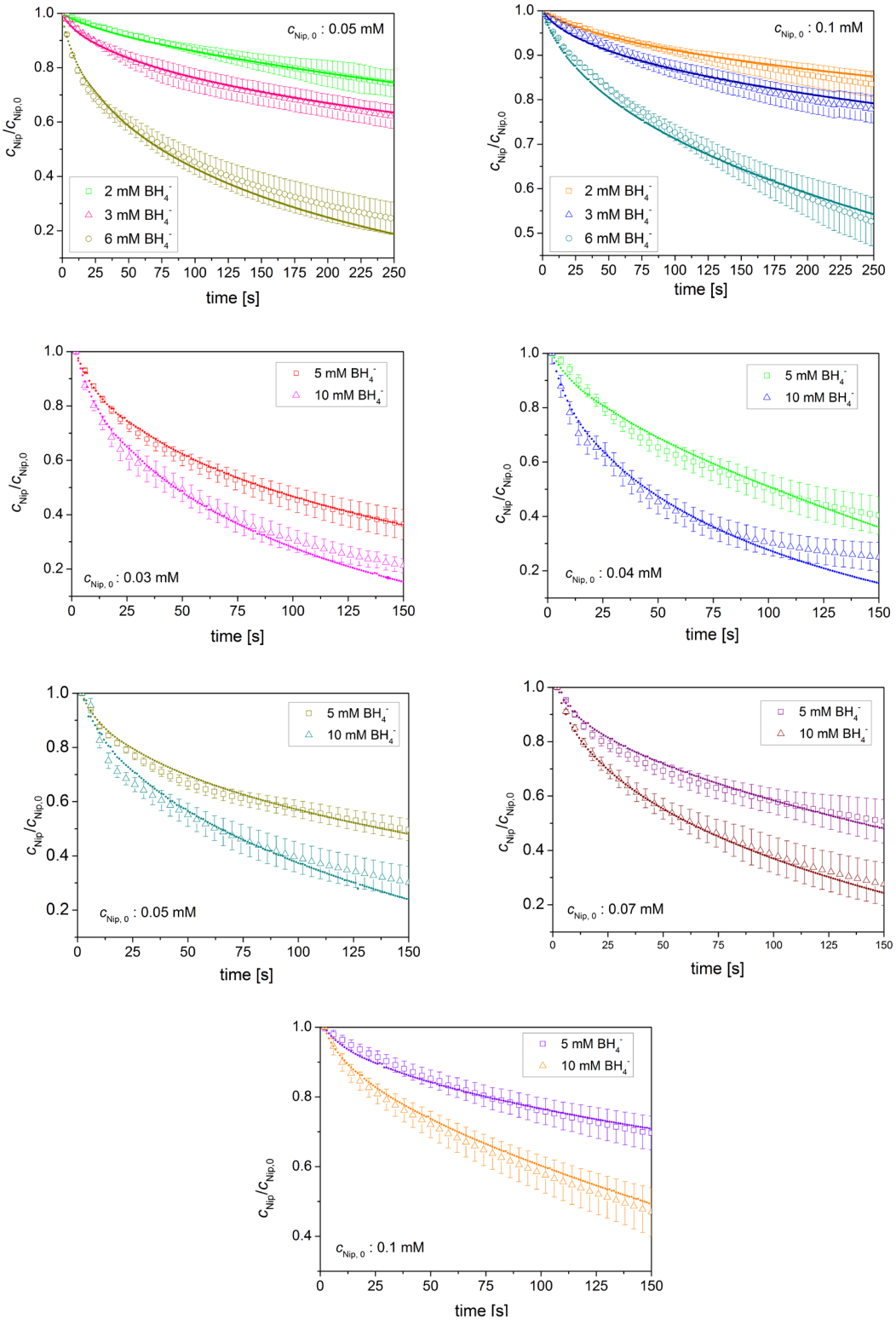


**Figure 4.6.3.1** Fit of the concentration of 4-Nip as the function of time by the numerical solution of Eqs. (2.3.2.3) and (2.3.2.5). The solid lines refer to the fits by the kinetic model. The concentration of Nip was normalized to the respective starting concentration $c_{Nip,0}$. The experimental data have been taken from reactions at temperature of 20 °C (data points with error bars).

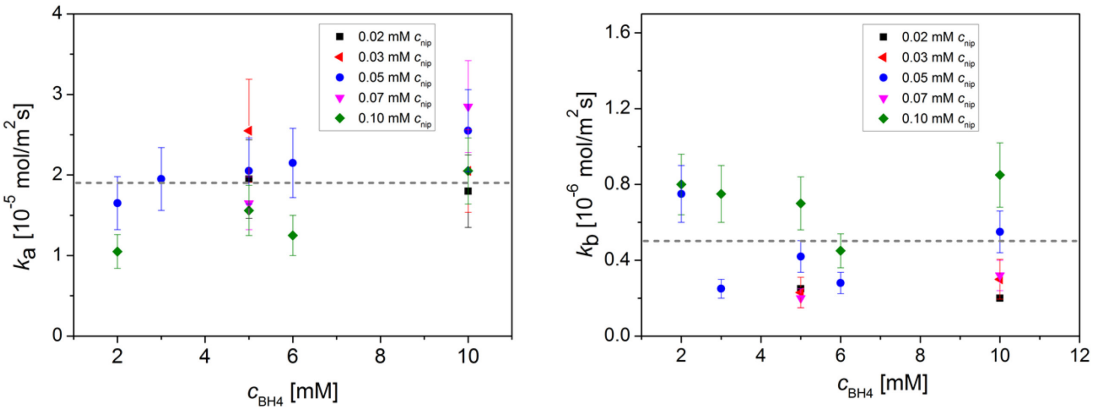


**Figure 4.6.3.2** Kinetic constants $k_a$ (left) and $k_b$ (right) derived from fitting results in Figure 4.6.3.1. The dash lines indicate the average values.

**Table 4.6.3.1** Summary of the kinetic and thermodynamic parameters

| | $k_a$ [mol/m$^2$ s] | $k_b$ [mol/m$^2$ s] | $K_{Nip}$ [L/mol] | $K_{BH4}$ [L/mol] | $K_{Hx}$ [L/mol] | n (nip) | $d_{NPs}$ (nm) |
|---|---|---|---|---|---|---|---|
| This study | $1.9\pm0.6\times10^{-5}$ | $0.5\pm0.3\times10^{-6}$ | 1200±400 | 80±20 | $(190\pm20)\times10^{3}$ | 0.5 | 9.8 |
| SPB-Au [112*] | $9.4\pm2.6\times10^{-4}$ | $5.6\pm1.4\times10^{-5}$ | 3700±900 | 50±4 | $(160\pm15)\times10^{3}$ | 0.5 | 2.6 |
| SPB-Pd [113*] | $1.4\pm0.4\times10^{-4}$ | $0.8\pm0.6\times10^{-5}$ | 2000±600 | 70±10 | $(180\pm20)\times10^{3}$ | 0.5 | 2.5 |
| $Au_{Ligand\text{-}free}$ [114] | $5.8\pm3.1\times10^{-4}$ | $5.4\pm2.0\times10^{-5}$ | 1800±700 | 60±10 | $(160\pm25)\times10^{3}$ | 0.5 | 7.2 |

* SPB: spherical polyelectrolyte brushes

For the rate constants $k_a$ and $k_b$, the values obtained in this study are smaller than the compared systems. The decrease in $k_a$ and $k_b$ may be related to the confinement of the PDA channels inside which Au nanoparticles are encapsulated. Besides, the PDA@Au nanoreactors have a smaller $K_{Nip}$, a similar $K_{BH4}$ and $K_{Hx}$. The slightly smaller $K_{Nip}$ indicates that the PDA protected Au nanoparticles are not as favorable as that of the compared systems for the adsorption of reactants. However, $K_{BH4}$ and $K_{Hx}$ of the PDA@Au nanoreactors are quite similar to those of SPB-Au, SPB-Pt, and ligand-free Au. The difference is within the experimental uncertainty. This indicates that the PDA scaffold has no obvious effect on the adsorption of $BH_4^-$ and Hx. Hence, we conclude that the PDA@Au nanoreactors show significant influence on $k_a$, $k_b$ and $K_{Nip}$ due to the separated PDA channels, but little effect on the adsorption of $BH_4^-$ and Hx. Despite lower reaction rates (smaller $k_a$ and $k_b$), the PDA@Au nanoparticles are firstly proved to be active catalytic nanoreactors for the reduction of 4-nitrophenol, revealing different kinetics from the reported systems.

In this work we demonstrate a novel approach for the synthesis of the PDA@Au nanoreactors

with interconnected channel structure by using PS-P2VP porous particles as soft template. PS-P2VP porous particles are firstly fabricated by swelling the solid nanospheres in ethanol at 75 °C. Au nanoparticles are assembled selectively onto the P2VP blocks of the template through *in situ* reduction of $AuCl_4^-$ under UV irradiation. A layer of PDA has been further deposited onto the template via the self-polymerization of dopamine under alkaline condition. By controlling the polymerizing time, the wall thickness of the PDA channel can be tuned efficiently. 3D reconstruction of the particles confirms the interconnected PDA channel structures, where Au nanoparticles are encapsulated. Because of the permeable property of the PDA layers, the composite particles can be applied as nanoreactors for the kinetic study of reduction of 4-nitrophenol. The reaction is surface controlled according to the theoretical analysis. The kinetic results show different $k_a$, $k_b$, and $K_{Nip}$, but similar $K_{BH4}$ and $K_{Hx}$ when compared with Au nanoparticles immobilized in SPB and ligand-free Au nanoparticles. As far as we know, this is the first report for the synthesis of PDA based nanoreactors with interconnected channel structure, which enables the kinetic study of encapsulated metal nanocatalysts in complex nanostructures. Because the continuous PDA channels possess larger surface area than normal nanoparticles, as well as permeable, durable and biocompatible properties, they are expected to have more applications in the field of nanoreactors.

# 5. Porous $Ti_4O_7$ particles as cathode material for lithium sulphur battery

With respect to low density and high specific surface area, mesoporous materials have become a subject of extensive research and been exploited in many applications, including ion exchange,[230] catalytic support,[231] efficient adsorbents for ion storage[232-234] and controlled release,[235, 236] supercapacitors,[237, 238] cathode materials for lithium-sulphur (Li-S) batteries,[239, 240] solar power and fuel cells.[241, 242] For example, Zhao et al.[231] demonstrated that mesoporous Au/silica materials with ordered mesopores exhibited an excellent performance in catalyzing the epoxidation of styrene with high conversion (95.4%) and selectivity (82.6%) toward styrene oxide owing to their high surface area (670 $m^2g^{-1}$) and efficient mass transport. Mesoporous carbon spheres with uniform pore sizes were fabricated by using poly(styrene-ethylene oxide) (PS-PEO) as template, which exhibited high electrochemical activity owing to the less restricted diffusion of guest species.[243] Mesoporous silica nanoparticles with pore sizes larger than big biomacromolecules (e.g., DNA) were shown to be an excellent candidate for drug delivery systems.[244] So far, most of the studies on porous nanoparticles are limited to classical materials (e.g., polymer, silica, carbon),[232-244] whereas the synthesis of conductive metal oxides with porous structures, for example $Ti_4O_7$ nanoparticles, have not been extensively studied, which has been highly valued as cathode materials for Li-S batteries.[245]

$Ti_4O_7$ is a member of the $Ti_nO_{2n-1}$ Magnéli phases, substoichiometric compositions of metallic titanium oxides that form a homologous series between the end members of $TiO_2$ and $Ti_2O_3$.[246] $Ti_4O_7$ has been utilized as a Pt catalyst support for fuel cells because of its high electrical conductivity (>$10^3$ S $cm^{-1}$ at room temperature).[247, 248] Besides, $Ti_4O_7$ contains polar O-Ti-O units that have a high affinity for polysulphide, which is essential for retarding the dissolution of polysulphide when applied as cathode material for Li-S batteries.[16, 249-251] According to Nazar's work,[73] the strong interaction between the $Ti_4O_7$ powders and polysulphide can mitigate the dissolution of polysulphide in the electrolyte, leading to excellent cycle performance and high-rate capability.

Generally, $Ti_4O_7$ can be synthesized by thermal reduction of $TiO_2$ at about 1000 ˚C with inert gas and carbon.[252, 253] This method results in the arbitrarily growing of the particles, making it difficult to precisely control the nanostructures of the particles. Considering the high volume ratio of sulphur and polysulphide in the electrolyte, the commonly used anchoring powder

would not be able to provide sufficient interfaces to fix all sulphide species. Thus, developing porous $Ti_4O_7$ nanoparticles by using template will be a practical way to address this limitation.

The formation of porous structures relies on the availability of porogens, which traditionally involve hard templates and soft templates.[254] Using hard template methods, pores could be created with precise control over size and shape.[255, 256] However, the removal of hard templates requires harsh conditions such as etching by acid or alkali, not only complicating the fabrication process, but also affecting the physical and chemical properties of the product. Soft templates are easier to be removed by means of simple dissolution or calcination. The use of preformed block copolymer particles as soft template opens a new path for the synthesis of inorganic particles with large surface area as well as complex inner structures. In the previous chapter of this thesis, a selective swelling strategy has been applied to generate porous PS-P2VP particles. They are proved to be good template for the synthesis of polydopamine@gold (PDA@Au) nanoreactors, as presented in chapter 4. Owing to the ability of coordinating with different precursors of metal and metal oxides, the porous PS-P2VP particles are considered to be promising template for the synthesis of porous $Ti_4O_7$ particles. In addition, when the $Ti_4O_7$ particles are used as cathode materials, the contact between the particles and the carbon black in the slurry can be improved by coating a thin layer of carbon onto the surface of the $Ti_4O_7$ particles. Reports of this kind have not been found yet.

In this chapter, the synthesis of $Ti_4O_7$ particles with interconnected pore structures will be investigated by using PS-P2VP porous particles as template. The synthesis procedure is shown in Figure 5.1. First, PS-P2VP porous particles can be obtained by selective swelling of the dense particles, as discussed in the previous chapters of this thesis. Second, titanium isopropoxide (TIP) can be used as precursor which can coordinate to the surface of the PS-P2VP template (Figure 5.1 step a). Third, TIP can be quickly hydrolyzed into $TiO_2$, which will transform to $Ti_4O_7$ nanoparticles by a consequent thermal reduction at 900 ˚C in argon atmosphere. The PS-P2VP templates can be burnt out, resulting in interconnected pores inside the nanoparticles (Figure 5.1 step b). In addition, a thin layer of carbon can be coated onto the porous $Ti_4O_7$ nanoparticles in order to improve the electrochemical performance, which can be directly compared with that of the uncoated $Ti_4O_7$ particles. To the best of our knowledge, this is the first report on the synthesis of $Ti_4O_7$ nanoparticles with interconnected pores. Such porous particles with high surface area can be used as multifunctional sulphur host material for lithium-sulphur batteries.

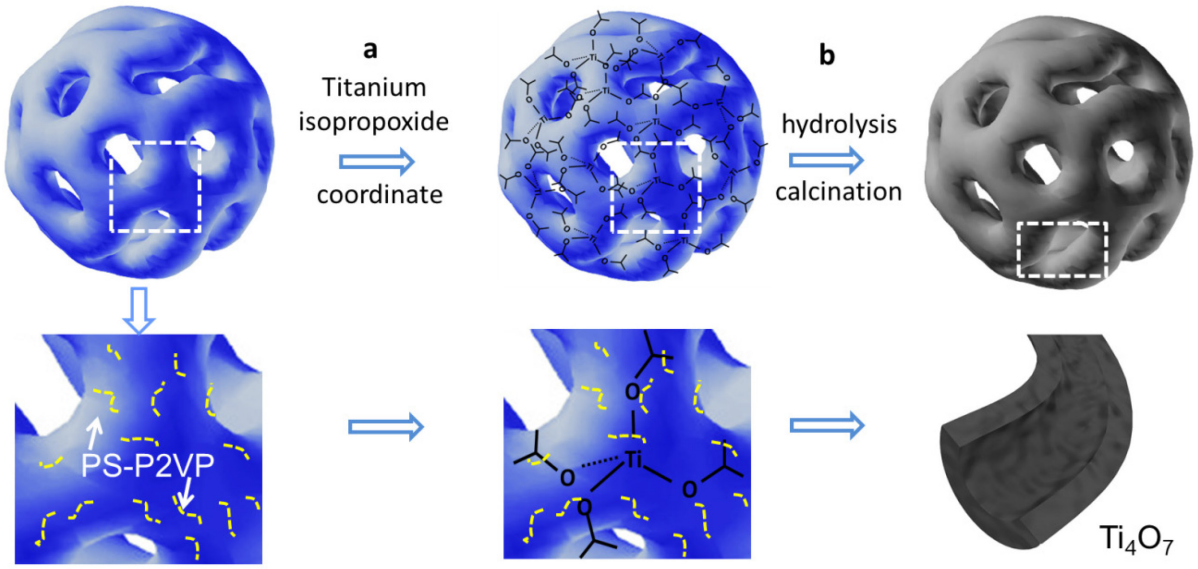


**Scheme 5.1** Synthesis procedure of the $Ti_4O_7$ nanoparticles. (a) Coordination of TIP with PS-P2VP template (b) Hydrolysis of the TIP into $TiO_2$, followed by the thermal reduction of $TiO_2$ into $Ti_4O_7$ at 900 ˚C in argon atmosphere.

## 5.1 Formation of porous $Ti_4O_7$ nanoparticles

Selective swelling induced porous materials preserve their mechanical strength and chemical heterogeneity of the block copolymers. These materials provide both geometric confinement and active sites for further functionalization, thus are perceived as potential soft templates for the synthesis of complex structures. In this work, PS-P2VP ($M_n$ (P2VP) = 16500 g/mol, $M_n$ (PS) = 50000 g/mol) has been used as model copolymer, which can provide 155 molar pyridine groups per gram for the coordination of inorganic precursors. As shown in Figure 5.1.1a-c, porous structure is generated by selective swelling of the P2VP domains accompanied with plastic deformation of the nonswollen PS. Titanium isopropoxide ($Ti(OCH(CH_3)_2)_4$) can coordinate to the porous PS-P2VP particles due to the coordination between the titanium and the pyridine group.[242] The $Ti(OCH(CH_3)_2)_4$ can be hydrolyzed into $TiO_2$ through addition of trace amount of water. Figure 5.1.1d-f show the $TiO_2$@PS-P2VP composite particles, from which we find that the pores on the surface of the template are mostly filled by the $TiO_2$ layer.

A thermal reduction process is essential for the generation of porous $Ti_4O_7$ particles. During this process, the PS-P2VP template is mostly burnt out, leaving interconnected pores inside the particles. Part of the polymer is carbonized and $TiO_2$ is reduced into $Ti_4O_7$ under argon

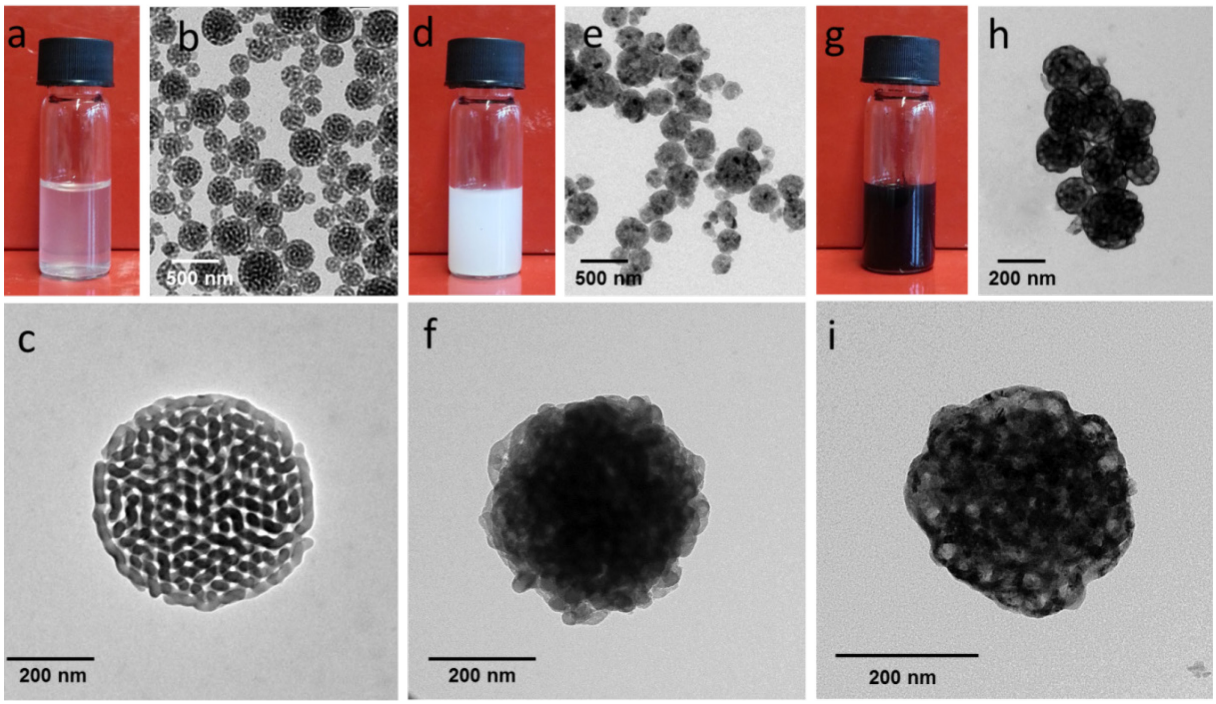


**Figure 5.1.1** Photos of the porous PS-P2VP particles (a), $TiO_2$@PS-P2VP particles (d) and $Ti_4O_7$ particles (g) dispersed in ethanol. TEM images of the porous PS-P2VP particles derived from a selective swelling process in ethanol at 75 ˚C for 60 min (b, c), $TiO_2$@PS-P2VP particles (e, f), and porous $Ti_4O_7$ particles (h, i) obtained from the thermal reducing of the $TiO_2$@PS-P2VP particles in figure (f).

atmosphere. Figure 5.1.1g-i show the obtained $Ti_4O_7$ particles, from which interconnected pores can be observed due to the removal of the PS-P2VP template. It is worth mentioning that the obtained porous $Ti_4O_7$ particles are easily redispersed in ethanol as shown in Figure 5.1.1g.

### 5.1.1 Influence of the water concentration on the hydrolysis of Titanium isopropoxide

In the synthesis of titanium oxides, the $H_2O$/Ti molar ratio, known as the hydrolysis ratio *r*, is a key factor in controlling the size, morphology and crystallinity of the precipitates that form.[257, 258] Using low hydrolysis ratios tends to result in partial hydrolysis, with retained organic groups present in the precipitate. Higher hydrolysis ratios are necessary for complete or near complete hydrolysis to take place.[259, 260] In this work, four different hydrolysis ratios have been studied on the hydrolysis of $Ti(OCH(CH_3)_2)_4$. It is found that the hydrolysis ratios lower than 60 lead to powders or partially collapsed porous particles after the thermal reduction of the $TiO_2$@PS-P2VP particles (Figure 5.1.1.1 a-c). Hydrolysis ratio of 100 results in $Ti_4O_7$ particles with interconnected pore structure (Figure 5.1.1.1d). Thus we choose r = 100 as the optimized hydrolysis ratio for the scalable synthesis of the porous $Ti_4O_7$ particles.

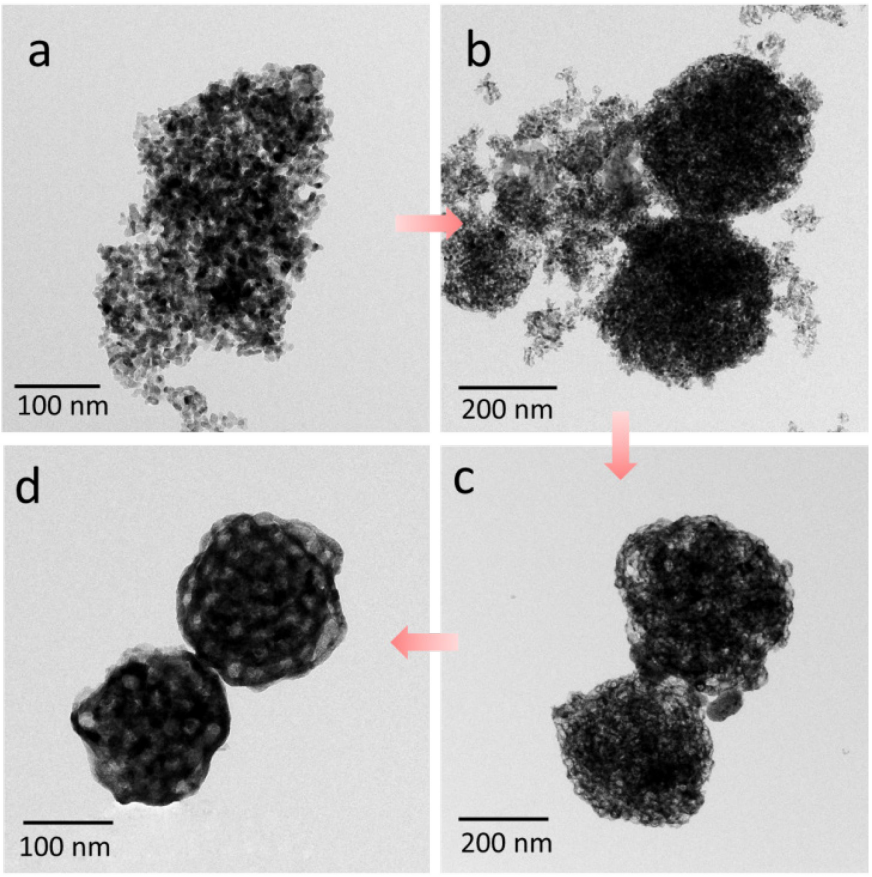


**Figure 5.1.1.1** TEM images of the $Ti_4O_7$ particles generated under different hydrolysis ratios. (a) r = 20. (b) r = 40. (c) r = 60. (d) r = 100.

### 5.1.2 Influence of PS-P2VP template on the porous structure of $Ti_4O_7$ particles

The swelling-induced porous structure of the PS-P2VP template can be adjusted by swelling time. At the initial stage of the morphology reconstruction, the volume of the P2VP domains increases as more swelling agent migrates into the swelling domains. The pressure imposed by the swelling P2VP domains results in plastic deformation of the nonswollen PS matrix. Porous structures are generated as a result of the swelling process advancing with time. As shown in Figure 5.1.2.1a, swelling at 75 ˚C for 30 min leads to the slightly swollen structure. Narrow spaces can be observed between the deformed PS-P2VP micellar fibers (Figure5.1.2.1a). Combining the TEM and SEM images, it is found that the resulted $Ti_4O_7$ particles show porous structure in the interior, but closed structure on the surface (Figure5.1.2.1b, e). This is because the small pores on the surface have been filled by the hydrolyzed $TiO_2$. The pore size inside of the $Ti_4O_7$ particles is measured as ~30 nm based on

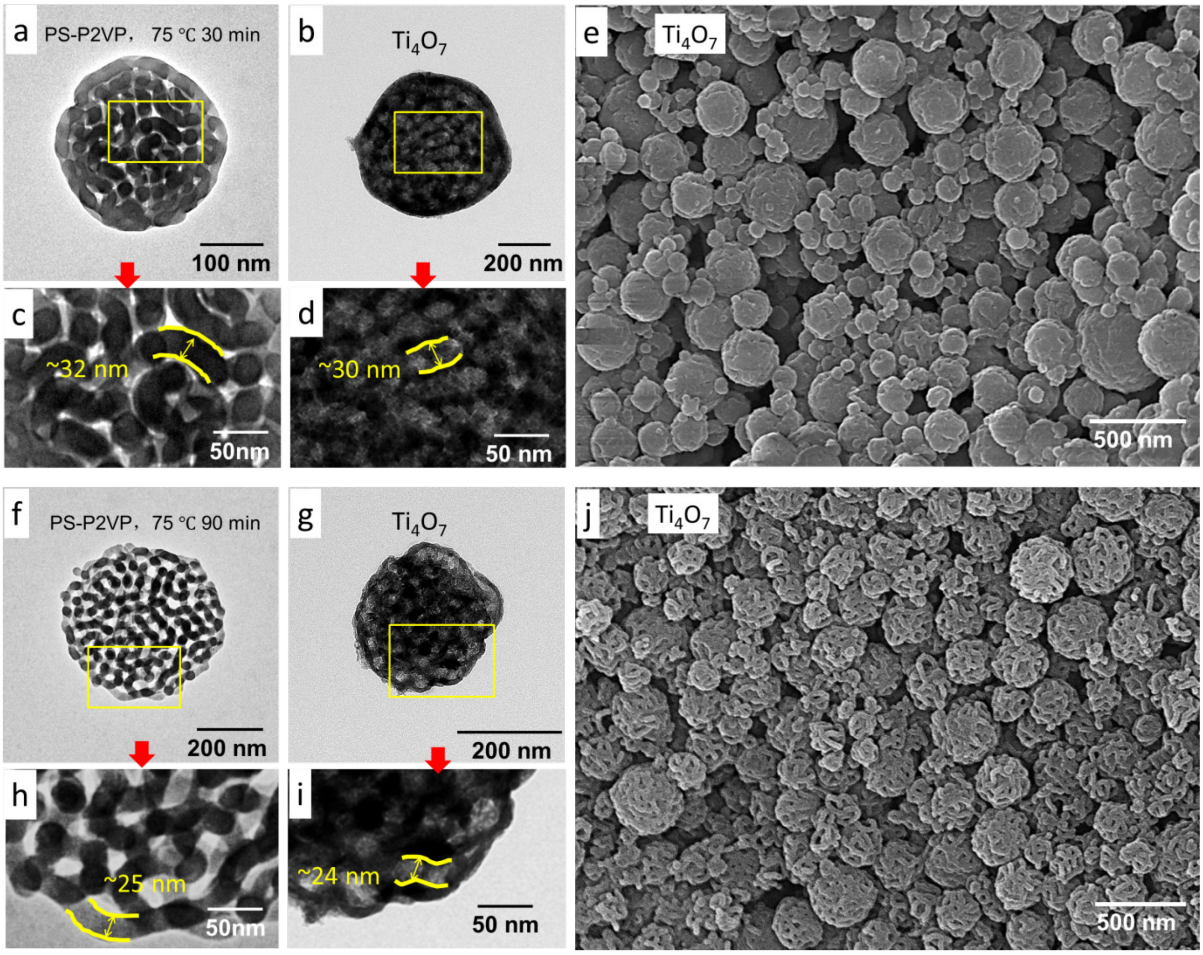


**Figure 5.1.2.1** (a) Porous PS-P2VP particles obtained from swelling in ethanol at 75˚C for 30 min. (b) $Ti_4O_7$ particles using particles in (a) as templates. (c) Selected zone in (a). (d) Selected zone in (b). (e) SEM image of the $Ti_4O_7$ particles in (b). (f) Porous PS-P2VP particles obtained from swelling in ethanol at 75˚C for 90 min. (g) $Ti_4O_7$ particles using particles in (f) as templates. (h) Selected zone in (f). (i) Selected zone in (g). (j) SEM image of the $Ti_4O_7$ particles (g).

the TEM image, which is similar with the width of the micellar nanofibers of the template particles (~32 nm, Figure 5.3.1c, d).

With the increase of the swelling time, the PS-P2VP micellar fibers further deform and expend to larger spaces. Figure 5.1.2.1f shows the porous structure of the PS-P2VP particles swollen at 75 ˚C for 90 min. More hollow spaces can be observed compared with Figure 5. 1.2.1a. In this case, the corresponding $Ti_4O_7$ particles show porous structure not only in the interior, but also on the surface (Figure5.1.2.1g, j). Because titanium can coordinate with pyridine groups, $Ti(OCH(CH_3)_2)_4$ precursor will adsorb on the PS-P2VP surface, which will then be covered by $TiO_2$ after hydrolysis. $TiO_2$ is reduced to $Ti_4O_7$ during the thermal reduction accompanied with the removal of the PS-P2VP template, which creates the interconnected pores. The width of the interconnected pores is ~24 nm, which is comparable

with that of the PS-P2VP micellar nanofibers of the templates (~25 nm, Figure5.1.2.1h, i). In addition, due to the large hollow space in the PS-P2VP template, the porous structures of the template will not be fully filled after coating with a thin layer of $TiO_2$ with a thickness of about 10 nm, which leads to open porous structures on the surface after calcination as shown in Figure Figure5.1.2.1j. This special porous structure can provide large surface area as well as valid confining space for sulphur/polysulphide.

## 5.2 X-ray diffraction and $N_2$ adsorption/desorption measurements of the $Ti_4O_7$ particles

Figure 5.2.1a shows the overview TEM image of the $Ti_4O_7$ particles (prepared with the $H_2O$/Ti molar ratio r = 100 by using the PS-P2VP templates swollen at 75˚C for 90 min). Highly porous particles consist of numerous interconnected pores can be observed. The structure is characterized by X-ray diffraction (XRD) and $N_2$ adsorption/desorption

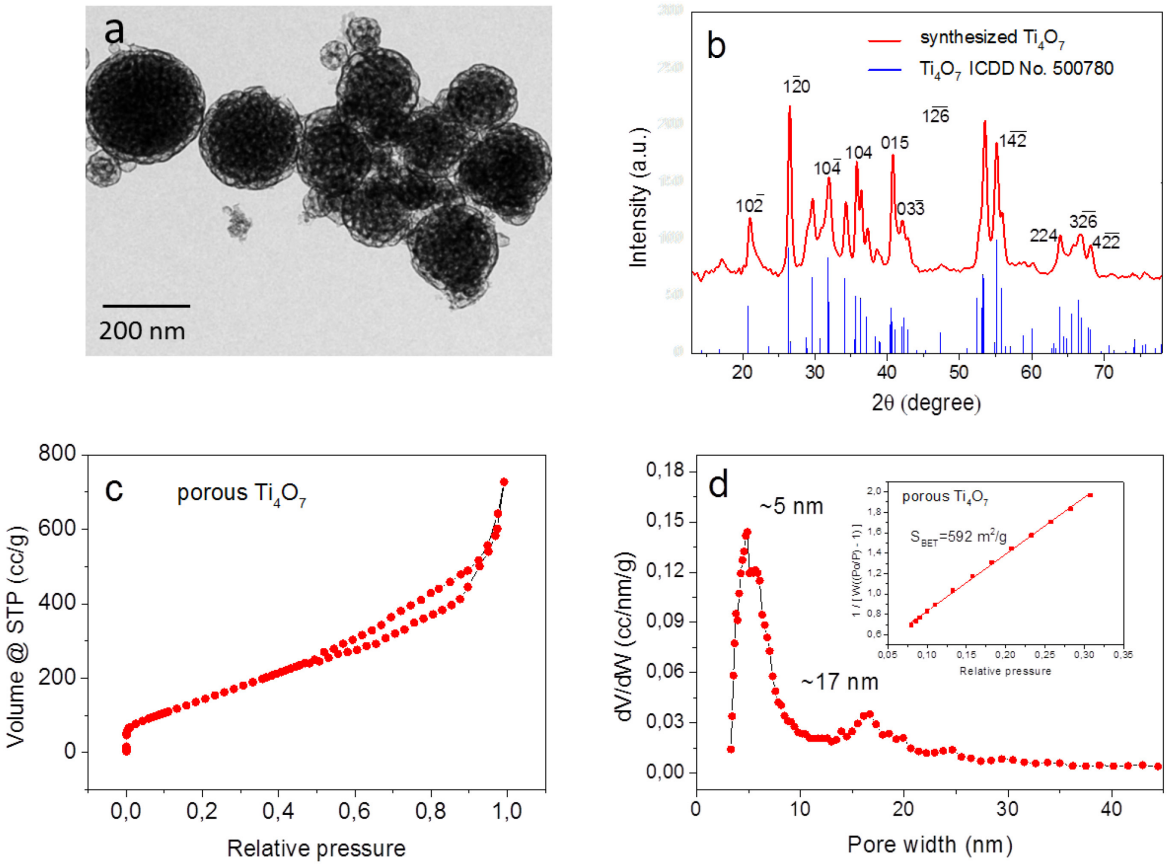


**Figure 5.2.1** (a) TEM image of the $Ti_4O_7$ particles. (b) XRD patterns of the $Ti_4O_7$ particles. (c) Nitrogen adsorption/desorption isotherms of the $Ti_4O_7$ particles. (c) BJH pore size distribution curve and BET data used to calculate surface area (inset).

measurement as shown in Figure 5.2.1. The XRD patterns of the synthesized particles are compared with the standard $Ti_4O_7$ (ICDD card No. 500780, Figure 5.2.1b). The good agreement in the XRD patterns indicates that $Ti_4O_7$ is the primary crystalline phase. The $N_2$ adsorption/desorption isotherms is displayed in Figure 5.2.1c. A distinct hysteresis loop can be observed with a typical IV isotherm, indicting the existence of a mesoporous structure. The pore size distribution curve shows a narrow range of mesopore size of 2-5 nm and a broad range (15-25 nm) centered at ca. 17 nm. The Brunauer-Emmett-Teller (BET) specific surface area of the $Ti_4O_7$ particles is 592 $m^2g^{-1}$ (Figure 5.2.1d), which is over two times the value of the $Ti_4O_7$ powders reported in previous works.[73]

To reveal the decisive effect of the PS-P2VP template on the porous morphology and the crystal structure of the $Ti_4O_7$ particles, a reference experiment has been conducted for the synthesis of $Ti_nO_m$ nanoparticles without using the PS-P2VP template. Figure 5.2.2a shows the TEM image of the obtained particles. The porous structure can not be produced without using the polymer template. Figure 5.2.2b shows the XRD pattern of the as-synthesized particles. Strong diffraction peaks at 25.27°and 48.01° are assigned to the (101) and (200)

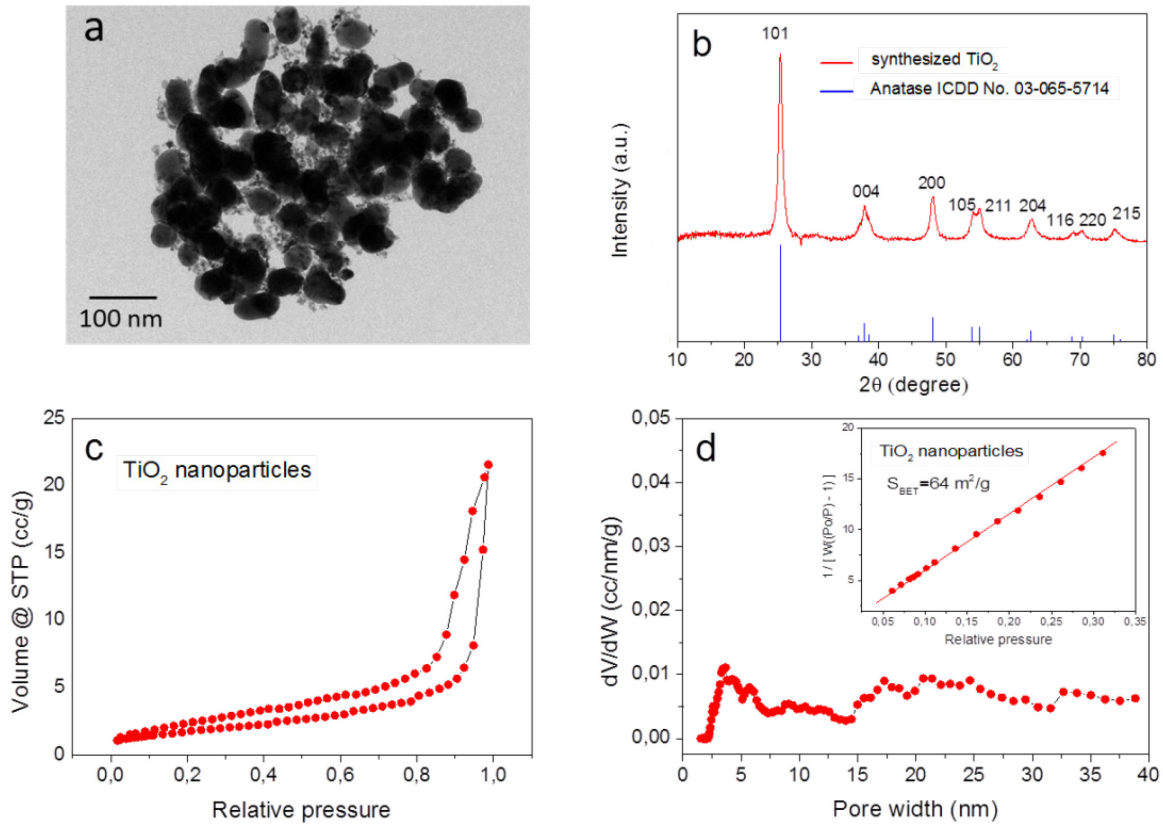


**Figure 5.2.2** (a) TEM image of the $TiO_2$ particles. (b) XRD patterns of the $TiO_2$ particles. (c) Nitrogen adsorption/desorption isotherms of the $TiO_2$ particles. (c) BJH pore size distribution curve and BET data used to calculate surface area (inset).

reflections of the anatase crystalline of $TiO_2$. The BET specific surface area of the $TiO_2$ particles is 64 $m^2 g^{-1}$, which is much smaller than that of the porous $Ti_4O_7$ particles. The pore size distribution curve in Figure 5.2.2d shows that no regular pores are formed in the range of 5-40 nm. This demonstrates that the presence of the PS-P2VP template is crucial for the formation of the porous structure of the $Ti_4O_7$ particles.

## 5.3 Modification of the $Ti_4O_7$ particles with a thin layer of carbon

In lithium-sulphur batteries, the electrodes are made up of multi-component mixtures. The key component in the cathode is a sulphur holding material such as porous carbon, graphite or metal oxides. Other components in the formulation generally include a binder, such as polyvinylidene fluoride (PVDF); a solvent of the electrode, such as N-methyl-2-pyrrolidone (NMP) - the solvent is just for making the slurry and is further rid off during the heat treatment, in the vacuum oven at ~ 80 ˚C; and an additive, such as carbon black, to improve the conductivity of the electrode.[261] Preparation of a good dispersion of nano-scaled powders in highly viscous polymer solutions has always been a problem in experiments.[262-266]

When metal oxides nanoparticles are applied as sulphur host material, the contact between the carbon black and the metal oxide nanoparticles is usually limited due to the uneven distribution of the carbon black particles. In order to improve this poor contact, a thin layer of carbon can be coated onto the surface of the metal oxide particles. In our study, the $Ti_4O_7$ particles have been further modified with a thin layer of polydopamine, which can be carbonized through calcination under argon atmosphere. TEM images of the $Ti_4O_7$ particles without and with a thin layer of carbon are presented in Figure 5.3.1a-d. A thin layer of carbon can be clearly seen after the surface coating (Figure 5.3.1c, d). TGA result indicates the inclusion of 2.3 wt% of carbon (Figure 5.3.1e).

Usually the direct comparison between different cathode materials is not easy due to the different morphologies and compositions of the materials. As is well known, the appropriate morphology of the cathode material is crucial in enhancing the electrochemical performance.[230-242] In this work, the surface coating route does not destroy the inner structure of the $Ti_4O_7$ particles. This enables the direct comparison

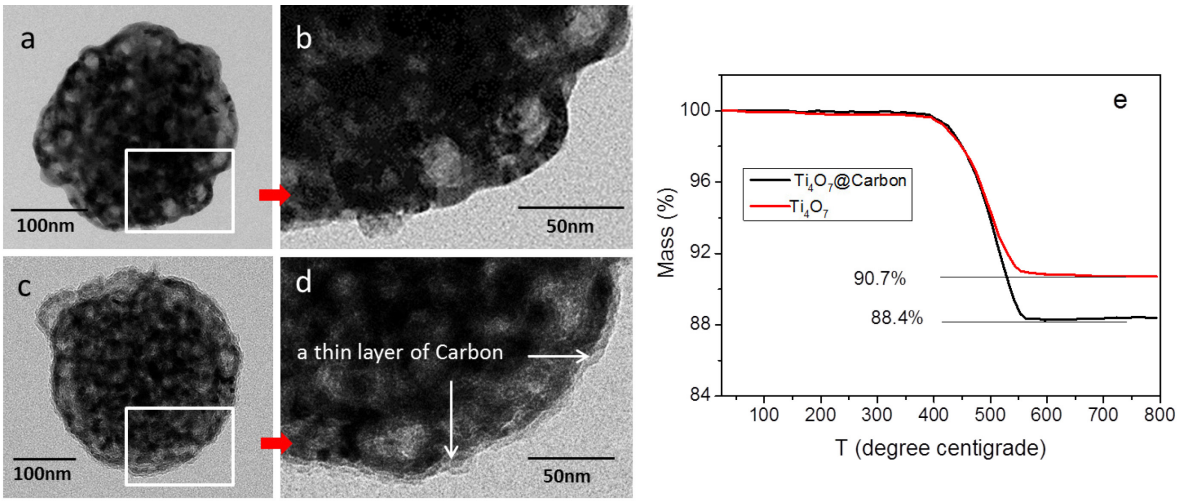


**Figure 5.3.1** (a) TEM image of the $Ti_4O_7$ particle; (b) enlarged zone in (a); (c) TEM image of the $Ti_4O_7$ particle coated with a thin layer of carbon. (d) enlarged zone in (c); (e) TGA results of the $Ti_4O_7$ particles with (black line) and without (red line) surface coating.

between the $Ti_4O_7$ particles and the carbon-coated $Ti_4O_7$ particles when they are used as cathode materials. The effect of the carbon layer can be demonstrated directly through the electrochemical performance.

## 5.4 The electrochemical performance of $Ti_4O_7$/sulphur cathode

$Ti_4O_7$ contains polar O-Ti-O units that have a high affinity for polysulphide. [16] The capability of $Ti_4O_7$ to adsorb $Li_2S_8$ is shown in Figure 5.4.1a. Addition of $Ti_4O_7$ into the $Li_2S_8$ solution results in a color change from light yellow to almost colorless upon the mixing for 2 h, which indicates the strong adsorption of $Li_2S_8$ onto the $Ti_4O_7$ particles. The distribution of different elements in the $Ti_4O_7$@sulphur composite is investigated by EDX mapping analysis under SEM observation (Figure 5.4.1b-f). The uniform distributions of Ti, O, C and S elements indicate the good adsorption and confinement of $Li_2S_8$ within the $Ti_4O_7$ porous particles.

To evaluate the electrochemical properties of the $Ti_4O_7$ porous particles, 2032-type coin cells have been fabricated with thick coated electrode films, in which the mass loading of sulphur is controlled to be approximately 1.0~1.2 mg per electrode. The utilized electrolyte (polysulphide solution) consists of stoichiometric 0.1 M $Li_2S_8$ (made of lithium sulphide and sulphur), 4 wt% lithium nitrate ($LiNO_3$), 8 wt% bis(trifluoromethane) sulfonimide lithium salt (LiTFSI) and a mixture of dioxolane and dimethoxy ethane (1:1, w/w).

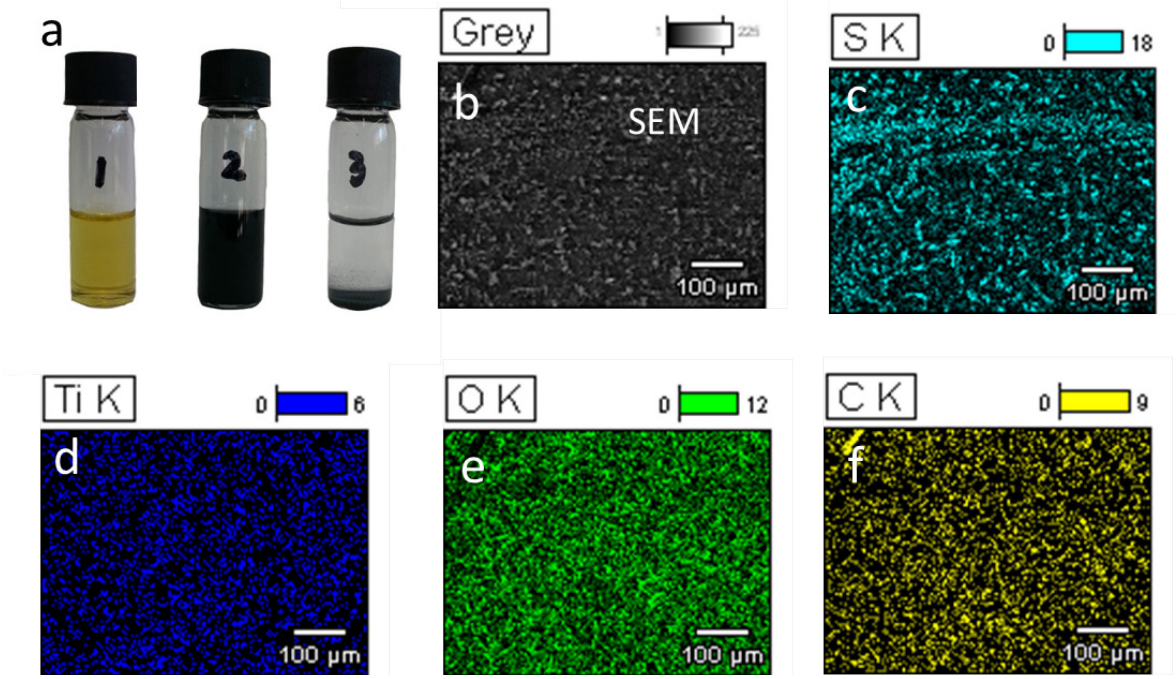


**Figure 5.4.1** (a) Sealed vials of a $Li_2S_8$/THF solution (1), a mixture of the $Li_2S_8$/THF solution and the $Ti_4O_7$ particles upon stirring for 2h (2), and the color change after it is settled down for 2 h (3). SEM image of the $Ti_4O_7$@$Li_2S_8$ (b) and corresponding EDX elemental mappings of (c) S; (d) Ti; (e) O and (f) C.

The electrochemical performance of both the mesoporous $Ti_4O_7$/S and the carbon-coated $Ti_4O_7$/S composites have been tested. Cyclic voltammetry (CV) curves of the Li-S cells with $Ti_4O_7$/S as the cathode are shown in Figure 5.4.2a. In the first cathodic scan, there are two well-defined reduction peaks at 2.34 and 2.02 V, corresponding to the multistep reduction mechanism of elemental sulphur. According to the previously reported mechanism, the 2.34 V plateau is caused by the change from element sulphur to higher-order lithium polysulphide ($Li_2S_n$, $4 < n < 8$), which are soluble in the liquid electrolyte.[267] The 2.02 V plateau is associated with further reduction of the higher polysulphide species ($Li_2S_n$, $4 < n < 8$) to the lower polysulphide species ($Li_2S_n$, $n \leqslant 2$).[268] In the anodic scan, the oxidation peak at about 2.38 V is associated with the reverse reactions in the charging stage. In the second scan, the anodic peak shifts to lower potential at 2.36 V, and the current of the corresponding peak decreases to a lower value.

Figure 5.4.2b shows the CV curves of the Li-S cells with the carbon-coated $Ti_4O_7$/S as a cathode. Compared with those of $Ti_4O_7$/S, a similar trend is found, implying that the carbon coating has no obvious effect on the redox mechanism of lithium sulphur battery. A little increase in the current peak indicates a lower resistance for the carbon-coated $Ti_4O_7$/S cathode. The variation in the anodic peaks between the first and second cycles can be ascribed to the

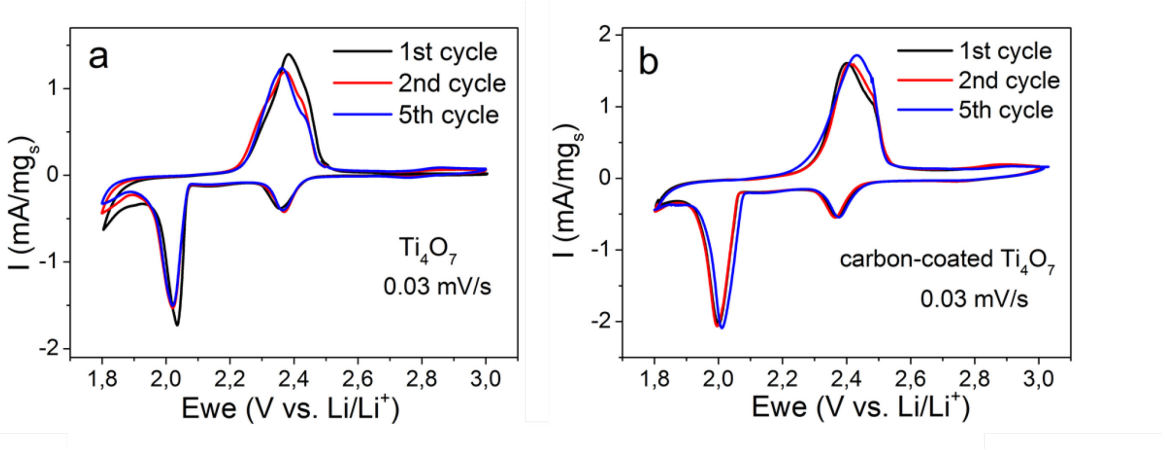


**Figure 5.4.2** CV profiles of the $Ti_4O_7$ based cathode (a) and the carbon-coated $Ti_4O_7$ based cathode (b). The scan rate is 0.03mV $s^{-1}$.

rearrangement of active sulphur from its original positions to more energetically stable sites. Little change of the current or potential for the redox peaks is noticeable in the subsequent scans, indicating high electrochemical stabilities for both the $Ti_4O_7$ and carbon-coated $Ti_4O_7$ based cathodes.

Figure 5.4.3 shows the galvanostatic charge/discharge profiles of the $Ti_4O_7$/S cathode and the carbon-coated $Ti_4O_7$/S cathode, which presents two typical discharge plateaus and one charge plateau, in accordance with the CV curves. Compared with the $Ti_4O_7$/S cathode, the carbon-coated $Ti_4O_7$/S cathode exhibits smaller electrochemical polarization (lower voltage hysteresis, ΔV). This suggests a highly facile electrochemical redox reaction and low resistance for the carbon-coated $Ti_4O_7$/S cathode.

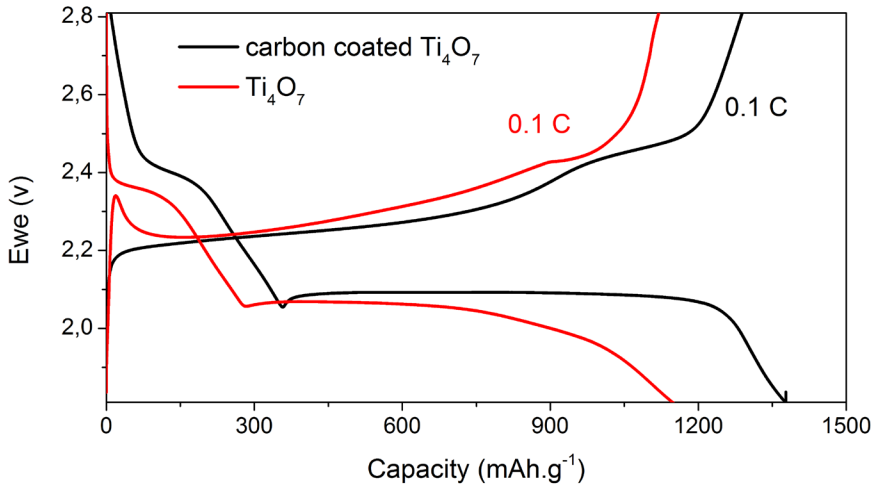


**Figure 5.4.3** Charge/discharge profiles of the $Ti_4O_7$ based cathode and the carbon-coated $Ti_4O_7$ based cathode. The current rate is 0.1 C.

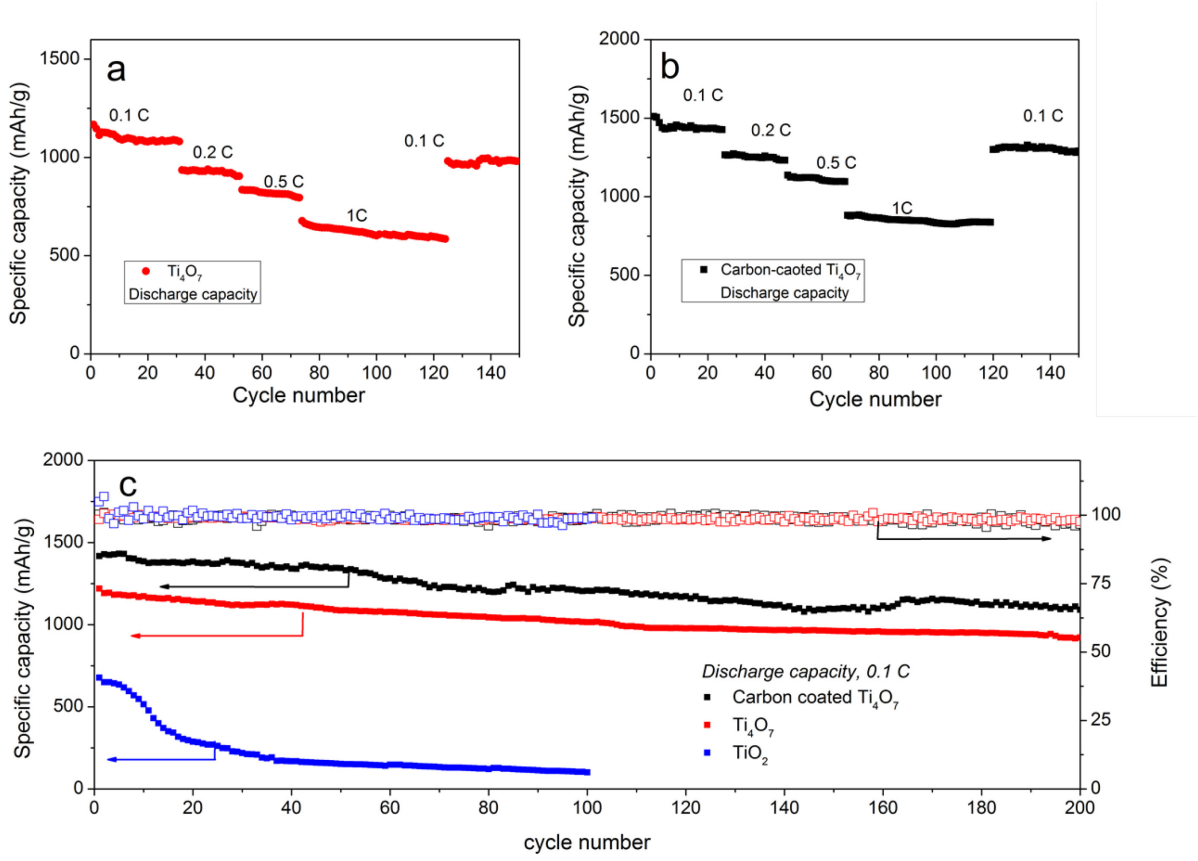


**Figure 5.4.4** Rate capabilities of the $Ti_4O_7$ based cathode (a) and the carbon-coated $Ti_4O_7$ based cathode (b) at different current rates (0.1C, 0.2 C, 0.5 C, 1 C and 0.1 C). (c) Cycling performance of the $Ti_4O_7$/S, carbon-coated $Ti_4O_7$/S and $TiO_2$/S cathodes with ~50μL of electrolyte over 200 cycles at a charge/discharge rate of 0.1 C. The solid squares represent capacity and hollow squares represent coulombic efficiency, respectively.

The rate capabilities of the electrodes are assessed at different discharge rates from 0.1 to 1 C rate, as shown in Figure 5.4.4. The $Ti_4O_7$/S electrode delivered a discharge capacity of 1119 mAh $g^{-1}$ at 0.1 C, 937 mAh $g^{-1}$ at 0.2 C, 840 mAh $g^{-1}$ at 0.5 C, and 640 mAh $g^{-1}$ at 1 C rate. When the current density is back to 0.1 C, the electrode shows a reversible capacity of 998 mAh $g^{-1}$ (Figure 5.4.4a). As comparison, the carbon-coated $Ti_4O_7$/S electrode exhibits higher discharge capacities under the same conditions. It delivers a discharge capacity of about 1450 mAh $g^{-1}$ at 0.1 C, 1270 mAh $g^{-1}$ at 0.2 C, 1113 mAh $g^{-1}$ at 0.5 C, and 873 mAh $g^{-1}$ at 1 C rate. When the current density is back to 0.1 C, the reversible capacity is 1304 mAh $g^{-1}$, suggesting better rate performance and improved stability (Figure 5.4.4b).

Nazar et al. [73] have used the $Ti_4O_7$ particles without porous structures as cathode materials. Their electrodes deliver a capacity of ~1000 mAh $g^{-1}$ at 0.2 C rate.[16] Another work reported by Cui et al.[269] using hydrogen reduced $TiO_2$ (which consists of TiO and $Ti_4O_7$) hollow particles as cathode materials. They present a high specific capacity of 1100 mAh $g^{-1}$ at 0.2 C

rate in the beginning. In my work, the carbon-coated porous $Ti_4O_7$/S electrode presents a higher capacity of 1270 mAh $g^{-1}$ at 0.2 C rate. This excellent performance should be attributed to the highly porous structure and the carbon layer on the surface of the $Ti_4O_7$ particles, which can provide larger surface area and better contact with the carbon black in the electrode than the reported works.

Figure 5.4.4c shows the cycling performances of the $Ti_4O_7$/S and the carbon-coated $Ti_4O_7$/S cathodes at a current rate of 0.1 C. As a comparison, $TiO_2$/S composite is also measured under the same conditions using the $TiO_2$ particles prepared in the absence of PS-P2VP templates as the cathode materials. The $Ti_4O_7$/S, carbon-coated $Ti_4O_7$/S, and $TiO_2$/S electrodes deliver the initial discharge capacities of 1219 mAh $g^{-1}$, 1411 mAh $g^{-1}$ and 543 mAh $g^{-1}$, respectively. A reversible capacity of 920 $mAhg^{-1}$ is obtained from the $Ti_4O_7$/S cathode even after 200 cycles, corresponding to 75.4% of capacity retention with an average Coulombic efficiency of 98.7%. The carbon-coated $Ti_4O_7$/S cathode presents a capacity of over 1090 mAh $g^{-1}$, corresponding to capacity retentions of 77.2% with an average Coulombic efficiency of 98.2%. In the case of the $TiO_2$/S electrode, it delivers a capacity of 99 mAh $g^{-1}$ after 100 cycles, corresponding to a capacity retention of only 18%. Apparently, the $Ti_4O_7$/S and carbon-coated $Ti_4O_7$/S electrodes exhibit not only much higher capacity but also better stability than the $TiO_2$/S electrode.

The excellent overall electrochemical performance of the $Ti_4O_7$/S and carbon-coated $Ti_4O_7$/S cathodes can be attributed to the following factors. First, a large amount of 2-5 nm and 15-25 nm mesopores in the $Ti_4O_7$ particles provide ultrahigh surface to adsorb the liquid electrolyte. Second, the porous $Ti_4O_7$ host can encapsulate and confine the polysulphide inside the pores by both physical and chemical interactions. [73] Compared with the typical carbon supports, which do not adsorb hydrophilic polysulphide intermediates, the strong surface interactions play a larger role in inhibiting sulphide dissolution and deposition than confinement that relies on physical barriers. Third, the carbon layer coated on the surface of the $Ti_4O_7$ particles provides better contact between the $Ti_4O_7$ particles and the carbon black of the slurry, which enables a lower resistance and improves the electrochemical performance of the carbon-coated $Ti_4O_7$ electrode.

In this chapter we demonstrate the synthesis of mesoporous $Ti_4O_7$ particles with high surface area of 592 $m^2g^{-1}$. $TiO_2$@PS-P2VP particles are first obtained through the hydrolysis of titanium isopropoxide adsorbed on the PS-P2VP templates. Porous $Ti_4O_7$ particles are generated by the thermal reduction of the $TiO_2$@PS-P2VP particles under argon atmosphere.

Combining the highly porous structure with the polar surface for strong lithium polysulphides binding, the $Ti_4O_7$/S cathode exhibit a high specific capacity of 1210 mAh $g^{-1}$ at 0.1 C, and a low capacity fade rate of 0.128% per cycle. More importantly, compared with the porous $Ti_4O_7$/S and the $TiO_2$/S cathodes, the carbon-coated $Ti_4O_7$/S cathode displays the highest capacity of 1411 mAh $g^{-1}$ at 0.1 C, and a best cycling stability with a capacity decay of only 0.11% per cycle over 200 charge/discharge cycles. This work realizes for the first time the precise control on the porous structures of the $Ti_4O_7$ materials. The complex structures are demonstrated to be crucial to enhance the electrochemical performance when they are applied as cathode materials for Li-S batteries.

# 6. Summary

This thesis presents the synthesis of novel functional materials using PS-P2VP particles and their porous structures as soft templates. By applying the Rayleigh instability of polymer tubes inside AAO nanopores, Pd@PS-P2VP@Au particles with Pd nanoparticles coated on the shell and Au nanoparticles trapped in the core have been synthesized. Their optical and catalytic properties have been studied. In addition, by using porous PS-P2VP particles as soft templates, PDA@Au nanoreactors and $Ti_4O_7$ nanoparticles with interconnected pore structures have been synthesized. Their applications as catalytic nanoreactors and cathode material for Li-S batteries have been investigated.

First, PS-P2VP@DT-Au core-shell particles have been synthesized by swelling the short polymer rods containing periodic DT-Au aggregations, which are derived from Rayleigh instability of bilayered PS-P2VP@DT-Au nanotubes confined in AAO cylindrical pores. The core size can be adjusted directly by using different amount of DT-Au nanoparticles. The composite particles with larger DT-Au cores exhibit a red shift of the surface plasmon absorption band in the UV-vis spectrum. Moreover, a second metal, Pd nanoparticles, has been successfully coated on the shell with patterned distribution, which can work efficiently as catalyst for the reduction of 4-nitrophenol. This study demonstrates for the first time the assembly of two types of metal nanoparticles onto polymer particles with separated distribution, which provides opportunities for the synthesis of novel multi-functional materials.

Second, the PDA@Au nanoreactors with interconnected channel structure have been synthesized by using porous PS-P2VP particles as template. The wall thickness of the PDA channels can be tuned efficiently by controlling the polymerizing time. 3D electron tomography (ET) reconstruction of the particles confirms the interconnected pore structure, where Au nanoparticles are encapsulated. Because of the permeable property of the PDA layers, the composite particles can be applied as nanoreactors for the kinetic study of catalytic reduction of 4-nitrophenol. The reaction is surface controlled according to the theoretical analysis. The kinetic results show different $k_a$, $k_b$ (the reaction rate constants of step A and step B), and $K_{Nip}$ (the adsorption constant of 4-nitrophenol), but similar $K_{BH4}$ and $K_{Hx}$ (the adsorption constant of $BH_4^-$ and Hx) when compared with Au nanoparticles immobilized in SPB and ligand-free Au nanoparticles. As far as we know, this is the first report for the

synthesis of PDA based nanoreactors with interconnected pore structure, which enables the kinetic study of encapsulated metal nanocatalyst in confined nanochannels.

Third, the synthesis of mesoporous $Ti_4O_7$ particles by using porous PS-P2VP particles as template has been demonstrated for the first time. The obtained particles exhibit the ultrahigh surface area of 592 $m^2g^{-1}$. When employed as sulfur host materials, the $Ti_4O_7$/S and carbon-coated $Ti_4O_7$/S cathodes exhibit high specific capacities and low capacity fade rates. More importantly, compared with mesoporous $Ti_4O_7$/S and $TiO_2$/S cathodes, the carbon-coated $Ti_4O_7$/S cathode displays the highest capacity of 1411 mAh $g^{-1}$ and a good cycling stability. The capacity decay is only 0.11% per cycle over 200 charge/discharge cycles.

# 7. Experimental

## 7.1 Chemicals and Materials

Poly(styrene-*b*-2-vinylpyridine) (PS-P2VP) ($M_n$ (PS) = 50000 g/mol; $M_n$ (P2VP) = 16500 g/mol; $M_w/M_n$ = 1.06) was obtained from Polymer Source Inc; dopamine hydrochloride, titanium isopropoxide ($Ti(OCH(CH_3)_2)_4$), 3-mercaptopropionic acid (MPA), sodium dodecyl sulfate (SDS), dodecanethiol (DT), gold(III) chloride hydrate ($HAuCl_4 \bullet 3H_2O$), palladium(II) chloride ($PdCl_2$), tetraoctylammonium bromide (TOBA), 4-nitrophenol, analytical grade toluene, ethanol, sodium hydroxide and sodium borohydride ($NaBH_4$), polyvinylidenedifluoride (PVDF), dioxolane (DOL), dimethoxyethane (DME), N-Methyl-2-pyrrolidone (NMP), lithium nitrate ($LiNO_3$) and bis(trifluoromethane)sulfonimide lithium salt (LiTFSI) were purchased from Sigma Aldrich, and used as received. Tetrahydrofuran (THF) was purchased from Fisher Scientific UK and used as received. De-ionized water was used for all aqueous solutions. Anodic aluminum oxide (AAO) membranes (Anodisc 13, 0.2 μm) were purchased from Whatman Ltd. The membranes were rinsed thoroughly with dichloromethane, tetrahydrofuran, and de-ionized water in sequence and then dried in vacuum before use.

## 7.2 Synthesis procedure

### 7.2.1 Synthesis of Pd@PS-P2VP@DT-Au particles

#### 7.2.1.1 Preparation of DT-Au nanoparticles

A $HAuCl_4 \bullet 3H_2O$ (0.6 mmol) aqueous solution (60 mL) was added to tetraoctylammonium bromide (TOAB, 1.2 mmol) dissolved in toluene (160 mL). Under vigorously stirring, the yellow aqueous solution became colorless, and the toluene phase turned to orange as a result of the complexing of $[AuCl_4]^-$ with tetraoctylammonium cations. The above solution was mixed with DT (0.6 mmol) in toluene (20 mL) for 10 min at room temperature. A freshly prepared aqueous solution (60 mL) of sodium borohydride (6 mmol) was added to the vigorously stirred mixture. After stirring for 12h, the obtained Au nanoparticles were separated by centrifugation (8000 rpm, 60 min), removal of the supernatant. The precipitation was cleaned by ethanol for three times. The product was dissolved in 30 mL toluene for the further preparation of PS-P2VP@DT-Au wetting solution.

#### 7.2.1.1 Synthesis of PS-P2VP@ DT-Au core-shell particles

For the wetting of the AAO membrane, one drop of PS-P2VP/DT-Au/toluene solution (5 µl) was placed on a glass slide. Subsequently, an AAO membrane was placed on the top of the solution. The nanopores of the membrane were filled with such mixed solution within seconds by capillary force. The membrane was first dried at ambient conditions, then in vacuum. The obtained PS-P2VP@DT-Au nanotubes with AAO membrane were annealed at 140 °C in vacuum for 120 minutes to produce polymer nanorods with periodic encapsulated holes based on the Rayleigh instability. Then the AAO membranes were dissolved in 5 wt % sodium hydroxide aqueous solution for 30 min to release the polymer nanorods. After thoroughly cleaned by DI water, these polymer nanorods were re-dispersed in water for ultrasonication. 30 minutes of ultrasonication is enough to cut the PS-P2VP@DT-Au nanorods into short nanoblocks. The concentrations of PS-P2VP and DT-Au nanoparticles used in the experiments are summarized as shown in table 7.2.1.1.1.

The obtained nanoblocks were dispersed in 4.5 ml SDS aqueous solution (the concentration of SDS is 1 mg/ml). A small amount of toluene (0.5 ml) was dropped into this aqueous suspension under sonication. The original clear suspension became opaque gradually. This opaque emulsion was kept at room temperature for 48 h to swell the PS-P2VP@DT-Au nanoblocks into particles. After that, the suspension was heated at 70°C to evaporate toluene, followed by centrifugation at 8000 rpm for 15 minutes to discard the surfactant.

**Table 7.2.1.1.1** The concentrations of PS-P2VP and DT-Au nanoparticles used in the experiments and the corresponding core sizes of the products.

| $c_{PS\text{-}P2VP}$ (mg/ml) | 60 | 60 | 60 | 60 | 40 | 90 |
|---|---|---|---|---|---|---|
| $c_{DT\text{-}Au}$ (mg/ml) | 5 | 20 | 30 | 40 | 20 | 20 |
| $D_{core}$ (nm) | 82 | 130 | 230 | 360 | 166 | 102 |

### 7.2.1.2 Assembly of Pd nanoparticles onto the PS-P2VP shell

PS-P2VP@DT-Au particles (5 mg) were first soaked in 5ml of the $PdCl_2$/HCl/ethanol ($PdCl_2$ 0.1 mM, HCl 1 mM) solution for 10 h to perform the coordination of metal ions with P2VP groups. Then the composite particles were centrifuged and redispersed in 5 ml $H_2O$. 0.1 ml of ice cold $NaBH_4$ ($10^{-3}$ M) was used as reducing agent and injected into the solution at a speed of 1ml/h with the syringe pump to generate Pd nanoparticels under stirring. The solution was further stirred for 2 min after adding of the reducing agent, followed by centrifugation twice at 5000 rpm for 10 min to remove the extra salt in the solution.

#### 7.2.1.3 Catalytic reduction of 4-nitrophenol

Sodium borohydride solution (0.5 ml, 0.1 M) was added to a 4-nitrophenol solution (4.5 ml, 0.11 mM) contained in a glass vessel. The solutions were purged with $N_2$ to remove oxygen from the system before mixing. A certain amount of Pd@PS-P2VP@DT-Au and PS-P2VP@DT-Au particles (50 µl, 0.36 mg/ml) was added to the mixed solution. UV-vis spectrum was immediately taken every minute in the range of 250 nm to 500 nm.

### 7.2.2 Synthesis of PDA@Au nanoreactors

#### 7.2.2.1 Synthesis of porous PS-P2VP templates

In a typical experiment, 10 mg of the PS-P2VP was dissolved into 10 ml toluene, and then emulsified into 100 ml water under sonication to form a surfactant emulsion (0.1 wt% of SDS). Toluene was evaporated at 75 °C in a water bath, resulting in the solidified PS-P2VP nanospheres dispersed in the water. The obtained nanoparticles were collected with repeated centrifugation at 10000 rpm and cleaned with de-ionized water for 3 times. 10 mg of the particles were redispersed in 60 ml ethanol and kept at 70 °C for 60 min to induce the porous structure. PS-P2VP with different swelling ratios ($M_n$ (P2VP)/$M_n$ (PS)) was studied in the experiment, as shown in table 7.2.2.1.1. The particles can be collected by centrifugation at 6000 rpm.

**Table 7.2.2.1.1** Experimental parameters in the synthesis of porous PS-P2VP particles.

| Block copolymer | $PS_{23.6k}$-$P2VP_{10.4k}$ | $PS_{50k}$-$P2VP_{16.5k}$ | $PS_{26k}$-$P2VP_{4.8k}$ |
|---|---|---|---|
| swelling ratio | 0.44 | 0.33 | 0.18 |
| swelling time (min) | 60 | 60 | 60 |
| swelling temperature (°C) | 70 | 70 | 70 |
| structure | collapsed particles | porous particles | multilayered particles |

#### 7.2.2.2 Assembly of Au nanoparticles onto the porous BCP particles

10 mg of the porous PS-P2VP particles were dispersed in 20 ml $HAuCl_4$/ethanol solution ($10^{-3}$ M) at room temperature for 12 h to allow the coordination of the $AuCl_4^-$ ions with the protonated pyridine rings of P2VP through electrostatic interactions. In order to avoid the formation of excess gold nanoparticles in the solution, the coordinated complex is separated from the free $AuCl_4^-$ ions by centrifugation. The composite particles were redispersed in 5 ml

ethanol in a quartz vessel. The adsorbed gold ions were reduced into gold nanoparticles by exposing the composites under UV light irradiation for 4h.

### 7.2.2.3 Deposition of polydopamine (PDA) to the Au@PS-P2VP porous particles

10 mg of the obtained Au@PS-P2VP porous particles were dipped into a solution of dopamine hydrochloride (0.3 mg/ml) dissolved in 10 ml Tris buffer (pH 8.5-8.8). The reaction vessel was kept in ice bath for several hours with vigorous stirring. After the deposition, the samples were collected by centrifugation at 6000 rpm for 10 min. In order to remove the extra dopamine and the secondary particles, the centrifugation should be repeated until the supernatant was colorless. The influence of the polymerization time on the thickness of the PDA layer is studies as shown in table 7.2.2.3.1.

**Table 7.2.2.3.1** The influence of the polymerization time on the thickness of the PDA layer.

| polymerization time (h) | ＜5 | 5 | 7 | 11 |
|---|---|---|---|---|
| thickness of the PDA layer (nm) | particles are fragile | 7~8 | 10~12 | 15~18 |

### 7.2.2.4 Removal of the PS-P2VP templates

The PDA@Au@PS-P2VP particles were redispersed in 50 ml THF at room temperature under stirring. After 7 days, the PS-P2VP frameworks were totally dissolved by THF and the PDA@Au hollow particles were remained in the suspension. Repeated centrifugation using THF at 6000 rpm was necessary for the complete removal of the dissolved polymer.

### 7.2.2.3 Kinetic study of the catalytic reduction of 4-nitrophenol

The reduction of 4-nitrophenol was conducted following the same procedure as presented in chapter 7.2.1.3. The PDA@Au nanoreactors were added into the solution before the UV-vis absorption measurement.

The kinetic analysis was performed by UV-vis spectroscopy at 400 nm (Perkin Elmer, Lambda 650 spectrometer). The content of Au nanoparticles was estimated from the TGA results and the size of the nanoparticles was measured from TEM images. For this calculation, the Au nanoparticles were assumed as spheres and the density of bulk Au metal was used ($\rho$ = 19.28 g/cm$^3$).

The evaluation of the data was done using a MatLab sheet as reported by Gu et al.[113] The concentration of Nip as the function of reaction time, $c_{Nip,exp}$, was analyzed by a numerical

solution of Eq 2.3.2.3 and 2.3.2.5 by two MatLab routines as reported by ref.113. The Matlab routines were used to calculate the theoretical Nip concentration $c_{Nip,th}$ as the function of time for a given values of $K_{Nip}$, $K_{BH4}$, $K_{Hx}$, $k_a$, $k_b$, and n. These data are compared to the experimental results and the constants are changed until agreement with the experiment is reached. In the following we give the details of this procedure.

First, all $c_{Nip,exp}$ data obtained at 20 ˚C were put into MatLab routine I. Routine I calculates $c_{Nip,th}$ for a given set of values of $K_{Nip}$, $K_{BH4}$, $K_{Hx}$, $k_a$, $k_b$ and n. The parameters from ref.113 were used as a first input for $K_{Nip}$, $K_{BH4}$, $k_a$, $k_b$, and n. Then every theoretical $c_{Nip,th}$ as the function of time was compared to the corre-sponding experimental data $c_{Nip,exp}$. The calculation is repeated until most of calculated data of $c_{Nip,th}$ match the corresponding experimental data sets $c_{Nip,exp}$.

Second, the reaction rate of steps A and B ($k_a$, $k_b$) may be different at different initial reaction concentrations, so the values of $k_a$ and $k_b$ were reoptimized using MatLab routine II. This routine can only analyze one $c_{Nip,exp}$ at one time. The values of $k_a$ and $k_b$ were changed while keeping $K_{Nip}$, $K_{BH4}$, $K_{Hx}$, and n obtained by routine I constant until full agreement was reached.

Third, the error bars of these parameters were also checked by MatLab routine II. Changing one parameter at one time, $c_{Nip,th}$ was compared to the corresponding experimental data $c_{Nip,exp}$ to check whether the value was within the error bars. Evidently, the consumption of the Hx intermediate cannot be measured directly and the fit values for $k_b$ and $K_{Hx}$ are less precise to get from this fit than the other parameters.

### 7.2.3 Synthesis of porous $Ti_4O_7$ nanoparticles

#### 7.2.3.1 Synthesis of porous PS-P2VP templates with different porosities

The porous PS-P2VP particles were generated as presented in chapter 7.2.2.1. The porous structures were tuned by swelling the PS-P2VP nanoparticles in ethanol at 75 °C for 30 min and 90 min, respectively. Typically, 10 mg of the PS-P2VP nanoparticles were swollen in 100 ml ethanol to generate the porous structures.

#### 7.2.3.2 Synthesis of $TiO_2$@PS-P2VP particles

In a typical synthesis, 10 mg of the PS-P2VP porous particles were dispersed in 100 ml ethanol. 0.2 mL of 3-mercaptopropionic acid (MAP) was added and stirred for 30 min at room temperature. 0.2 mL of titanium (IV) isopropoxide (TIP) was then added to the

suspension. The suspension was stirred for 48 h to allow the coordination of TIP with the P2VP components. A hydrolysis process was induced by addition of a certain amount of $H_2O$ into the suspension. The $H_2O$/Ti molar ratio (known as hydrolysis ratio *r*) was controlled by using different amounts of $H_2O$ (0.15 ml, 0.3 ml, 0.45 ml, 0.7 ml). The suspension was stirred for 3 h and then centrifuged for 30 min at 8000 rpm to collect the PS-P2VP@titanium oxide nanoparticles.

### 7.2.3.3 The transformation of $TiO_2$@PS-P2VP particles into porous $Ti_4O_7$ particles

The $TiO_2$@PS-P2VP particles were collected by freeze drying and heated at 100 °C for 4-6 h, then heated at ~900 °C for 4 h under an Ar stream in a tubular furnace (Nabertherm GmbH) using a heating ramp of 4 °C $min^{-1}$. A black powder product (porous $Ti_4O_7$ particles) was obtained. The experimental parameters and results are summarized in table 7.2.3.3.1.

**Table 7.2.3.3.1** Effect of the experimental parameters on the structure of the obtained $Ti_4O_7$ particles.

| hydrolysis ratio *r* / PS-P2VP template | 20 | 40 | 60 | 100 |
|---|---|---|---|---|
| swelling at 75 °C for 30 min | ×* | × | × | closed particles with interconnected pores |
| swelling at 75 °C for 90 min | × | × | × | open porous particles with interconnected pores |

* no porous particles were generated.

### 7.2.3.4 Synthesis of the carbon-coated porous $Ti_4O_7$ particles

In a typical experiment, 10 mg of the $TiO_2$@PS-P2VP particles were dipped into a solution of dopamine hydrochloride (0.1 mg/ml) dissolved in 10 ml Tris buffer (pH 8.5-8.8). The reaction vessel was kept in ice bath for more than 7 h with vigorous stirring. After the deposition, the dispersion shows a color change from white to black indicating the deposition of PDA on the surface of the particles. The samples were collected by centrifugation at 6000 rpm for 10 min. The secondary PDA particles were removed by repeated centrifugation until the supernatant was colorless.

### 7.2.3.5 Polysulphide adsorption study

Solid $Li_2S_8$ was synthesized by reacting elemental sulphur and $Li_2S$ in the desired ratio in a mixed solution of dioxolane (DOL) and dimethoxyethane (DME) (see table 7.2.3.5.1). The solution was stirred at room temperature for 1 h inside an Ar-filled glovebox. The solvent was removed in vacuum and the precipitate was washed with toluene and then vacuum dried.

A $Li_2S_8$ solution was prepared by dissolving 4 mg of $Li_2S_8$ in 5 ml of THF. 20 mg of the mesoporous $Ti_4O_7$ particles were added to the solution. To inspect the color change, the solution was stirred for 2 h and then settled down for 2 h.

**Table 7.2.3.5.1** Preparation of $Li_2S_8$ solution.

| $Li_2S_8$ solution (1 M) | |
|---|---|
| lithium sulfide ($Li_2S$) | 460 mg |
| Sulfur (S) | 2245 mg |
| dioxolane (DOL) | 3.897 ml |
| dimethoxyethane (DME) | 4.764 ml |

### 7.2.3.6 Electrochemical measurements

Mesoporous $Ti_4O_7$ particles with carbon black Super P and the binder (PVDF) at a weight ratio of 8:1:1 were dispersed in NMP. The mixture was drop-cast on carbon coated aluminium foil with an area of 2 $cm^2$ to form a thin slurry, which was applied as the positive electrodes. The electrodes were dried at 80 °C overnight before use. Coin cells were assembled inside the glovebox with lithium foil as anode and an electrolyte consisting of 0.1 M $Li_2S_8$, 4 wt% lithium nitrate ($LiNO_3$), 8 wt% bis(trifluoromethane)sulfonimide lithium salt (LiTFSI) and a mixture of dioxolane and dimethoxy ethane (1 : 1, w/w). The typical sulphur loading was 1.0-1.2 mg per electrode, with an electrolyte volume of ~50 µl in all cases. Celgard was used as a separator material. The cells were galvanostatically cycled between 1.8 and 3.0 V at different C rates (1C=1675 mA $g^{-1}$). The CV curves were recorded on an electrochemical workstation at a scanning rate of 0.03mV $s^{-1}$ in the voltage range of 1.8-3.0 V. The current density and the capacities were calculated based on the mass of sulfur.

## 7.3 Characterization

### 7.3.1 Transmission electron microscopy (TEM)

The morphology of the obtained particles including Pd@PS-P2VP@Au nanoparticles, PDA@Au nanoreactors and the porous $Ti_4O_7$ particles was investigated by the transmission electron microscopy (TEM). Carbon support film (200 mesh, Science Services, Munich, Germany) have been pretreated by the glow discharge for 10 seconds. TEM specimens were prepared by dropping approximately 5 µL of a 0.1 wt.-% solution on a TEM copper grid. After 2 minutes, the excess liquid was blotted with a filter paper. The remaining liquid film on

the TEM grid was dried at room temperature for at least one hour. The specimen was inserted into the sample holder (EM21010, JEOL GmbH, Eching, Germany) and transferred to a JEOL JEM-2100 with a LaB6 cathode (JEOL GmbH, Eching, Germany). The TEM was operated at an acceleration voltage of 200 kV. All images were recorded digitally by a bottom-mounted 4k CMOS camera system (TemCam-F416, TVIPS, Gauting, Germany) and proceeded with a digital imaging processing system (EM-Menu 4.0, TVIPS, Gauting, Germany).

### 7.3.2 Scanning electron microscope (SEM)

The SEM imaging and EDX elemental mapping were performed using a LEO 1530 field emission SEM equipped with an EDX attachment (Zeiss) measurement in secondary electron mode at 2kV. The samples for the SEM analysis were prepared by dropping 100µL of the concentrated sample solution on the silicon wafer and drying at room temperature.

### 7.3.3 Electron tomography (ET) and image processing

For electron tomography a drop of PDA@Au nanoparticles suspended in water was dried on a standard TEM grid (copper grid with a thin layer of carbon). Tomographic data were collected on a JEM-2100 (JEOL GmbH, Eching, Germany) operated at 200 kV and equipped with a 4 k × 4 k CMOS digital camera (TVIPS TemCam-F416). Tilt series were acquired using the Serial-EM acquisition software package with a tilt-range of ± 60° and a 2° angular increment at a magnification of 30,000x, corresponding to a pixel size of 3.6 Å at the specimen level.

Tilt series were aligned using patch tracking then reconstructed using weighted back-projection with the IMOD software package. Surface segmentation was performed using Amira (FEI Company, Eindhoven, the Netherlands). Three-dimensional surface renderings and movies were generated with UCSF Chimera.

### 7.3.4 Thermogravimetric Analysis (TGA)

The TGA measurements were conducted using a Netsch STA409PC LUXX. 10 mg of dried samples were filled in the crucible and heated from 25 °C to 600 °C under a constant Ar flow (30 ml/min) with a heating rate of 10K/min. Then the samples were hold at this temperature for 8 h. The weight loss was attributed to the polymer and the remaining weight to the metal content of the sample.

### 7.3.5 Fourier transform infrared spectroscopy (FT-IR)

FTIR were carried out at a FT-IR Nexus (Thermo Nicolet). 5 mg of the dried sample (PDA@Au nanoreactors) was mixed with KBr and pressed to a pellet. The absorption bonds located at 1490, 1435 and 1250 $cm^{-1}$ were used to identify the formation of polyphenoles structure. The absorption at 1622 $cm^{-1}$ was used to identify the stretching of aromatic C-C bonds of indole.

### 7.3.6 X-ray diffraction (XRD)

XRD measurements were performed in a Bruker D8 diffractometer in the locked coupled mode (2θ ranging from 10° to 80°) with Cu Kα1 radiation, the incident wavelength is 1.5406 Å. For the accomplished measurements the acceleration voltage is set to 40 kV and the filament current to 40 mA.

### 7.3.7 Ultraviolet-visible (UV-vis) spectroscopy

For the measurement of the UV-vis absorption spectra, the reaction solution with catalytic particles (Pd@PS-P2VP@Au nanoparticles or PDA@Au nanoreactors) was placed in quartz sample cell with a 1.0 cm cell path length. UV-vis spectra (at 400 nm) were recorded by using Lambda 650 spectrometer supplied by Perkin-Elmer at 20 °C with reference spectra of the corresponding particles in water.

### 7.3.8 $N_2$ adsorption/desorption measurement

$N_2$ adsorption/desorption isotherms were obtained using a Quantachrome Autosorb-1 system at 77 K. Surface areas were calculated using the Brunauer-Emmett-Teller method based on a multipoint analysis. Mesoporous $Ti_4O_7$ particles and $TiO_2$ particles were degassed at 250 °C for 12 h before measurement.

# Bibliography

(1) Wu, D.; Xu, F.; Sun, B.; Fu, R.; He, H.; Matyjaszewski, K. Design and Preparation of Porous Polymers. *Chem*. *Rev*. **2012**, *112*, 3959- 4015.

(2) Lou, X. W.; Archer, L.A.; Yang, Z. Hollow Micro-/Nanostructures: Synthesis and Applications. *Adv*. *Mater.* **2008**, *20*, 3987-4019.

(3) Pal, N.; Bhaumik, A. Soft Templating Strategies for the Synthesis of Mesoporous Materials: Inorganic, Organicinorganic Hybrid and Purely Organic Solids. *Adv. Colloid Interface Sci.* **2013**, *189*, 21-41.

(4) Mai, Y.; Eisenberg, E. Self-assembly of block copolymers, *Chem. Soc. Rev.* **2012**, *41*, 5969-5985.

(5) Zvelindovsky, A. V. Nanostructured Soft Matter: Experiment, Theory, Simulation and Perspectives. Springer: Dordrecht, The Netherlands, **2007**

(6) Wang, L.; Mei, S. L.; Jin, Z. X. The Influences of Cooperative Swelling and Coordination on Patterned Decoration of Gold on block Copolymer Nanospheres. *Macromol. Chem. Phys.* **2013**, *214*, 2579-2583.

(7) Jang, S. G.; Audus, D. J.; Klinger, D.; Krogstad, D. V.; Kim, B. J.; Cameron, A.; Kim, S. W.; Delaney, K. T.; Hur, S. M.; Killops, K. L.; Fredrickson, G. H.; Kramer, E. J.; Hawker, C. J. Striped, Ellipsoidal Particles by Controlled Assembly of Diblock Copolymers. *J. Am. Chem. Soc.* **2013**, *135*, 6649-6657.

(8) Liang, R.; Xu, J.; Deng, R.; Wang, K.; Liu, S.; Li, J.; Zhu, J. Assembly of Polymer-Tethered Gold Nanoparticles under Cylindrical Confinement. *ACS Macro Lett.* **2014**, *3*, 486-490.

(9) Yabu, H.; Jinno, T.; Koike, K.; Higuchi, T.; Shimomura, M. Three-Dimensional Assembly of Gold Nanoparticles in Spherically Confined Microphase-Separation Structures of Block copolymers. *Macromolecules* **2011**, *44*, 5868-5873.

(10) Yang, H.; Guo, L.; Wang, Z.; Yan, N.; Wang, Y. Nanoporous Films with Superior Resistance to Protein Adsorption by Selective Swelling of Polystyrene-block-poly(ethylene oxide). *Ind. Eng. Chem. Res.* **2016***, 55,* 8133-8140.

(11) Wang, Y.; Tong, L.; Steinhart, M. Swelling-Induced Morphology Reconstruction in Block Copolymer Nanorods: Kinetics and Impact of Surface Tension during Solvent Evaporation. *ACS Nano* **2011**, *5*, 1928-1938.

(12) Mei, S. L.; Jin, Z. X. Mesoporous Block-Copolymer Nanospheres Prepared by Selective Swelling. *Small* **2012**, *9*, 322-329.

(13) Guo, L.; Zhang, X.; Wang, Y. Atomic Layer Deposition on Block Copolymer Membranes with Gyroidal Nanopores Toward Periodically Nanostructured Vapor Sensors: Nanotubes versus Nanorods. *Adv. Mater. Interf.* **2016**, *3*, 1600017(1-9).

(14) Yin, J.; Yao, X. P.; Liou, J.-Y.; Sun, W.; Sun, Y.-S.; Wang, Y. Membranes with Highly Ordered Straight Nanopores by Selective Swelling of Fast Perpendicularly Aligned Block Copolymers. *ACS Nano* **2013**, *7*, 9961-9974.

(15) Hamley, I. W. Nanostructures Fabrication Using Block Copolymers. *Nanotechnology* **2003**, *14*, 39-54.

(16) Loo, Y.-L. Templating Polymer Crystal Growth Using Block Copolymer, *Dekker Encyclopedia of Nanoscience and Nanotechnology* **2009**, 4303-4315.

(17) Park, C.; Yoon, J.; Thomas, E. L. Enabling Nanotechnology with Self Assembled Block Copolymer Pattern. *Polymer* **2003**, *44*, 6725-6760.

(18) Jeon, S. J.; Yi, G. R.; Koo, C. M.; Yang, S. M. Nanostructures inside Colloidal Particles of Block Copolymer/Homopolymer Blends. *Macromolecules* **2007**, *40*, 8430-8439.

(19) Yu, B.; Li, B.; Jin, Q.; Ding, D.; Shi, A.-C. Self-Assembly of Symmetric Diblock Copolymers Confined in Spherical Nanopores. *Macromolecules* **2007**, *40*, 9133.

(20) Jackson, A. M.; Myerson, J. W.; Stellacci, F. Spontaneous Assembly of Subnanometreordered Domains in the Ligand Shell of Monolayer-Protected Nanoparticles. *Nat. Mater.* **2004**, *3*, 330-336.

(21) Yabu, H.; Higuchi, T.; Ljiro, K.; Shimomura, M. Spontaneous Formation of Polymer Nanoparticles by Good-Solvent Evaporation as a Nonequilibrium Process. *Chaos* **2005**, *15*, 047505

(22) Higuchi, T.; Tajima, A.; Yabu, H.; Shimomura, M. Spontaneous Formation of Polymer Nanoparticles with Inner Micro-Phase Separation Structures. *Soft Matter* **2008**, *4*, 1302-1305.

(23) Rider, D. A.; Chen, J. I. L.; Eloi, J.-C. Arsenault, A. C.; Russell, T. P.; Ozin, G. A.; Manners, I. Controlling the Morphologies of Organometallic Block Copolymers in the 3-Dimensional Spatial Confinement of Colloidal and Inverse Colloidal Crystals. *Macromolecules* **2008**, *41*, 2250-2259.

(24) Higuchi, T.; Motoyoshi, K.; Sugimori, H.; Jinnai, H.; Yabu, H.; Shimomura, M.; Phase Transition and Phase Transformation in Block Copolymer Nanoparticles. *Macromol. Rapid Commun.* **2010**, *31*, 1773-1778.

(25) Urbas, A.; Sharp, R.; Fink, Y.; Thomas, E. L.; Xenidou, M.; Fetters, L. J. Tunable Block Copolymer/Homopolymer Photonic Crystals. *Adv. Mater.* **2000**, *12*, 812-814.

(26) Broz, P.; Driamov, S.; Ziegler, J.; Ben-Haim, N.; Marsch, S.; Meier, W.; Hunziker, P. Toward Intelligent Nanosize Bioreactors: A pH-Switchable, Channel-Equipped, Functional Polymer Nanocontainer. *Nano Lett.* **2006**, *6*, 2349-2353.

(27) Chen, W.-Q.; Wei, H.; Li, S.-L.; Feng, J.; Nie, J.; Zhang, X.-Z.; Zhuo, R.-X. Fabrication of Star-Shaped, Thermo-Sensitive Poly-(N-isopropylacrylamide)-cholic Acid-poly(-caprolactone) Copolymers and Their Self-Assembled Micelles as Drug Carriers. *Polymer* **2008**, *49*, 3965-3972.

(28) Shipway, A. N.; Katz, E.; Willner, I. Nanoparticle Arrays on Surfaces for Electronic, Optical, and Sensor Applications. *ChemPhysChem* **2000**, *1*, 18-52.

(29) Fort, E.; Ricolleau, C.; Sau-Pueyo, J. Dichroic Thin Films of Silver Nanoparticle Chain Arrays on Facetted Alumina Templates. *Nano Lett.* **2003**, *3*, 65-67.

(30) Bai, J.; Huang, S.; Wang, L.; Chen, Y.; Huang, Y. Fluid Assisted Assembly of One-dimensional Nanoparticle Array inside Inorganic Nanotubes. *J. Mater. Chem.* **2009**, *19*, 921-923.

(31) Sung, J.; Hicks, M. E.; Van Duyne, R. P.; Spears, K. G. Nanoparticle Spectroscopy: Plasmon Coupling in Finite-Sized Two-Dimensional Arrays of Cylindrical Silver Nanoparticles. *J. Phys. Chem. C* **2008**, *112*, 4091-4096.

(32) Hicks, E. M.; Zou, S.; Schatz, G. C.; Spears, K. G.; Van Duyne, R. P.; Gunnarsson, L.; Rindzevicius, T.; Kasemo, B.; Käll, M. Controlling Plasmon Line Shapes through Diffractive Coupling in Linear Arrays of Cylindrical Nanoparticles Fabricated by Electron Beam Lithography. *Nano Lett.* **2005**, *5*, 1065-1070

(33) Zhang, H.; Chung, S.W.; Mirkin, C. A. Fabrication of Sub-50-nm Solid-State Nanostructures on the Basis of Dip-Pen Nanolithography. *Nano Lett.* **2003**, *3*, 43-45.

(34) Li, W.K.; Liu, S.Q.; Deng, R.H.; Wang, J.Y.; Nie, Z.Z.; Zhu, J.T. A Simple Route To Improve Inorganic Nanoparticles Loading Efficiency in Block Copolymer Micelles. *Macromolecules* **2013**, *46*, 2282-2291.

(35) Bockstaller, M. R.; Mickiewicz, R. A.; Thomas, E. L. Block Copolymer Nanocomposites: Perspectives for Tailored Functional Materials. *Adv. Mater.* **2005**, *17*, 1331-1349.

(36) Haryono, A.; Binder, W. H. Controlled Arrangement of Nanoparticle Arrays in Block-Copolymer Domains. *Small* **2006**, *2*, 600-611.

(37) Balazs, A. C.; Emrick, T.; Russell, T. P. Nanoparticle Polymer Composites: Where Two Small Worlds Meet. *Science* **2006**, *314*, 1107-1110.

(38) Lee, J. Y.; Shou, Z. Y.; Balazs, A. C. Predicting the Morphologies of Confined Copolymer/Nanoparticle Mixtures. *Macromolecules* **2003**, *36*, 7730-7739.

(39) Mayer, A. B. R. Colloidal Metal Nanoparticles Dispersed in Amphiphilic Polymers. *Polym. Adv. Technol.* **2001**, *12*, 96-106.

(40) Mandal, M.; Ghosh, S.K.; Kundu, S.; Esumi, K.; Pal, T. UV Photoactivation for Size and Shape Controlled Synthesis and Coalescence of Gold Nanoparticles in Micelles. *Langmuir* **2002**, *18*, 7792-7.

(41) Caruso, R.A. Ashokkumar, M.; Grieser, F. Sonochemical Formation of Gold Sols. *Langmuir* **2002**, *18*, 7831-7836.

(42) Sun, X.; Jiang, X.; Dong, S.; Wang, E. One-step Synthesis and Size Control of Dendrimer-protected Gold Nanoparticles: A Heat-Treatment Based Strategy. *Macromol Rapid Commun* **2003**, *24*, 10241-10248.

(43) Kao, J.; Thorkelsson, K.; Bai, P.; Rancatoreb, B. J.; Xu, T. Toward Functional Nanocomposites: Taking the Best of Nanoparticles, Polymers, and Small Molecules. *Chem. Soc. Rev.* **2013**, *42*, 2654-2678.

(44) Mizuno, H.; Buriak, J.M. Nanoscale Patterning of Organic Monolayers by Catalytic Stamp Lithography: Scope andL. *ACS Appl. Mater. Interfaces* **2009**, *1*, 2711-2720.

(45) Kim, M. P.; Ku, K. H.; Kim, H. J.; Jang, S. G.; Yi, G. R.; Kim, B. J. Surface Intaglio Nanostructures on Microspheres of Gold-Cored Block Copolymer Spheres. *Chem. Mater.* **2013**, *25*, 4416-4422.

(46) Yabu, H.; Jinno, T.; Koike, K.; Higuchi, T.; Shimomura, M. Three-Dimensional Assembly of Gold Nanoparticles in Spherically Confined Microphase-Separation Structures of Block Copolymers. *Macromolecules* **2011**, *44*, 5868-5873.

(47) Liang, R.; Xu, J. P.; Deng,R. H.; Wang, K.; Liu, S. Q.; Li, J. Y.; Zhu, J. T. Assembly of Polymer-Tethered Gold Nanoparticles under Cylindrical Confinement. *ACS Macro Lett.* **2014**, *3*, 486-490.

(48) Mei, S. L.; Feng, X. D.; Jin; Z. X. Fabrication of Polymer Nanospheres Based on Rayleigh Instability in Capillary Channels. *Macromolecules* **2011**, *44*, 1615-1620.

(49) Su, B. L.; Sanchez, C.; Yang,X. Y. Hierarchically Structured Porous Materials from Nanoscience to Catalysis, Separation, Optics, Energy, and Life Science, Wiley-VCH, Weinheim, Germany, **2012**.

(50) Hamley, I. W. The Physics of Block Copolymers. Oxford Univ. Press, Oxford, **1998**.

(51) Lee, J. S.; Hirao, A.; Nakahama, S. Polymerization of Monomers Containing Functional Silyl Groups. 5. Synthesis of New Porous Membranes with Functional Groups. *Macromolecules* **1988**, *21*, 274-276.

(52) Urbas, A. M.; Maldovan, M.; DeRege, P.; Thomas, E. L. Bicontinuous Cubic Block Copolymer Photonic Crystals. *Adv. Mater.* **2002**, *14*, 1850-1853.

(53) Wang, Y.; Tong, L.; Steinhart, M. Swelling-Induced Morphology Reconstruction in Block Copolymer Nanorods: Kinetics and Impact of Surface Tension During Solvent Evaporation. *ACS Nano* **2011**, *5*, 1928-1938.

(54) Li, L.; Shen, X.; Hong,S. W.; Hayward, R. C.; Russell, T. P. Fabrication of Co-continuous Nanostructured and Porous Polymer Membranes: Spinodal Decomposition of Homopolymer and Random Copolymer Blends. *Angew. Chem. Int. Ed.* **2012**, *51*, 4089-4094.

(55) Park, M.; Harrison, C.; Chaikin, P. M.; Register, R. A.; Adamson, D. H. Block Copolymer Lithography: Periodic Arrays of 1011 Holes in 1 Square Centimeter. *Science* **1997**, *276*, 1401-1404.

(56) Thurn-Albrecht, T.; Steiner, R.; DeRouche, J.; Stafford, C. M.; Huang, E.; Bal, M.; Tuominen, M.; Hawker, C. J.; Russell, T. P. Nanoscopic Templates from Oriented Block Copolymer Films. *Adv. Mater.* **2000**, *12*, 787-791.

(57) Zalusky, A. S.; Olayo-Valles, R.; Taylor, C. J.; Hillmyer, M. A. Mesoporous Polystyrene Monoliths. *J. Am. Chem. Soc.* **2001**, *123*, 1519-1520.

(58) Cheng, J. Y.; Ross, C. A.; Chan, V. Z. H.; Thomas, E. L.; Lammertink, R. G. H.; Vancso, G. J. Formation of a Cobalt Magnetic Dot Array via Block Copolymer Lithography. *Adv. Mater.* **2001**, *13*, 1174-1178.

(59) Cho, H.; Park, H.; Russell, T. P.; Park, S. Precise Placements of Metal Nanoparticles from Reversible Block Copolymer Nanostructures. *J. Mater. Chem.* **2010**, *20*, 5047-5051.

(60) Yokoyama, H.; Sugiyama, K. Nanocellular Structures in Block Copolymers with $CO_2$-philic Blocks Using $CO_2$ as a Blowing Agent: Crossover from Micro- to Nano-cellular Structures with Depressurization Temperature. *Macromolecules* **2005**, *38*, 10516-10522.

(61) Yan, N.; Wang, Y. Selective Swelling Induced Pore Generation of Amphiphilic Block Copolymers: The Role of Swelling Agents. *Journal of Polymer Science Part B: Polymer Physics* **2016**, *54*, 926-933.

(62) Clodt,J. I.; Filiz, V.; Rangou, S.; Buhr, K.; Abetz, C.; Höche, D.; Hahn, J.; Jung, A.; Abetz, V. Double Stimuli-Responsive Isoporous Membranes via Post-Modification of pH-Sensitive Self-Assembled DiBlock Copolymer Membranes. *Adv. Funct. Mater.* **2013**, *23*, 731-738.

(63) Hsueh, H.-Y.; Huang, Y.-C.; Ho, R.-M.; Lai, C.-H.; Makida, T.; Hasegawa, H. Nanoporous Gyroid Nickel from Block Copolymer Templates via Electroless Plating. *Adv. Mater.* **2011**, *23*, 3041-3046.

(64) Tappan, B. C.; Steiner, S. A.; Luther, E. P. Nanoporous Metal Foams. *Agnew. Chem. Int. Ed.* **2010**, *49*, 4544-4565.

(65) Chu, S. Z.; Wada, K.; Inoue, S.; Todoroki, S. I. Synthesis and Characterization of Titania Nanostructures on Glass by Al Anodization and Sol−Gel Process. *Chem. Mater.* **2002**, *14*, 4595-4602.

(66) Erlebacher, J.; Aziz, M. J.; Karma, A.; Dimitrov, N.; Sleradzki, K. Evolution of Nanoporosity in Dealloying. *Nature* **2001**, *410*, 450-453.

(67) Nielsch, K.; Müller, F.; Li, A. P.; Gösele, U. Uniform Nickel Deposition into Ordered Alumina Pores by Pulsed Electrodeposition. *Adv. Mater.* **2000**, *12*, 582-586.

(68) Hashimoto, T.; Tsutsumi, K.; Funaki, Y. Nanoprocessing Based on Bicontinuous Microdomains of Block Copolymers: Nanochannels Coated with Metals. *Langmuir* **1997**, *13*, 6869-6872.

(69) Li, F. B.; Yao, X. P.; Wang, Z. Z.; Xing, W. H.; Jin, W. Q.; Huang, J.; Wang, Y. Highly Porous Metal Oxide Networks of Interconnected Nanotubes by Atomic Layer Deposition. *Nano Lett.* **2012**, *12*, 5033-5038.

(70) Wang, Y.; Qin, Y.; Berger, A.; Yau, E.; He, C.; Zhang, L. B.; Gösele, U.; Knetz, M.; Steinhart, M. Nanoscopic Morphologies in Block Copolymer Nanorods as Templates for Atomic-Layer Deposition of Semiconductors. *Adv. Mater.* **2009**, *21*, 2763-2766.

(71) Liu, J.; Xue, D. F. Thermal Oxidation Strategy towards Porous Metal Oxide Hollow Architectures. *Adv. Mater.* **2008**, *20*, 2622-2627.

(72) Tao, X.; Wang, J.; Ying, Z.; Cai, Q.; Zheng, G.; Gan, Y.; Huang, H.; Xia, Y.; Liang,C.; Zhang, W.; Cui, Y. Strong Sulfur Binding with Conducting Magnéli-Phase TinO2n-1 Nanomaterials for Improving Lithium-Sulfur Batteries. *Nano Lett*. **2014**, *14*, 5288-5294.

(73) Pang, Q.; Kundu, D.; Cuisinier, M.; Nazar, L. F. Surface-enhanced Redox Chemistry of Polysulphides on A Metallic and Polar Host for Lithium-Sulphur Batteries. *Nat*. *Commun*. **2014**, *5*, 47591-8.

(74) Caruso, F. Colloids and Colloid Assemblies. Wiley-VCH, Weinheim,Germany, **2004.**

(75) Rayleigh, L. On the Stability of a Cylinder of Viscous Liquid under Capillary Force, Scientific Papers (*Cambridge University Press, Cambridge*) **1902**, *3*, 585-593.

(76) Plateau, J. Statique Expérimentale Et Théorique Des Liquides Soumis Aux Seules Forces Moléculaires. *Gauthier-Villars*, **1873**. Paris.

(77) Vollrath, F.; Edmonds, D. J. Modulation of the Mechanical-Properties of Spider Silk by Coating with Water, *Nature*, **1989**, *340*, 305-307.

(78) Tsai, C. C.; Chen, J. T. Rayleigh Instability in Polymer Thin Films Coated in the Nanopores of Anodic Aluminum Oxide Templates. *Langmuir* **2014**, *30*, 387-393.

(79) Srolovitz, D. J.; Safran, S. A. Capillary Instabilities in Thin Films. I. Energetics. *J. Appl. Phys.* **1986**, *60*, 247-254 .

(80) Gennes, P. G.; Brochard-Wyart, F.; Quere, D. Capillarity and Wetting Phenomena; *Springer, New York*, **2004**.

(81) Callegari, G.; Calvo, A.; Hulin, J. P.; Brochard-Wyart, F. Dewetting versus Rayleigh Instability inside Capillaries. *Langmuir* **2002**, *18*, 4795-4798.

(82) Callegari, G.; Calvo, A.; Hulin, J. P. Dewetting Processes in a Cylindrical Geometry. *Eur. Phys. J. E* **2005**, *16*, 283-290.

(83) Chen, J. T.; Zhang, M.; Russell, T. P. Instabilities in Nanoporous Media. *Nano Lett*. **2007**, *7*, 183-187.

(84) Ugelstad, J.; Mork, P.C.; Kaggerud, K.H.; Ellingsen, T.; Berge, A. Swelling of Oligomer-Polymer Particles. New Methods of Preparation of Emulsions and Polymer Dispersions. *Adv*. *Colloid Interface Sci*. **1980**, *13*, 101-140.

(85) Wilkinson, M. C.; Hearn, J.; Steward, P. A. The Cleaning of Polymer Colloids. *Adv*. *Colloid Interface Sci*. **1999**, *81*, 77-165.

(86) Yaffe, M. B.; Kramer, E. J. Plasticization Effects on Environmental Craze Microstructure. *J. Mater. Sci.* **1981**, *16*, 2130-2136.

(87) Wang, Y. Nondestructive Creation of Ordered Nanopores by Selective Swelling of Block Copolymers: Toward Homoporous Membranes. *Acc Chem Res*. **2016**, *49*, 1401-1408.

(88) Bates, F. S.; Fredrickson, G. H. Block Copolymers-Designer Soft Materials. Phys. *Today* **1999**, *52*, 32-38.

(89) Wang, Y.; He, C.; Xing, W. H.; Li, F. B.; Tong, L.; Chen, Z. Q.; Liao, X. Z.; Steinhart, M. Nanoporous Metal Membranes with Bicontinuous Morphology from Recyclable Block-Copolymer Templates. *Adv*. *Mater*. **2010**, *22*, 2068-2072.

(90) Guo, L. M.; Wang, Y. Monolithic Membranes with Designable Pore Geometries and Sizes via Retarded Evaporation of Block Copolymer Supramolecules. *Macromolecules* **2015**, *48*, 8471-8479.

(91) Bates, F. S. Polymer-polymer phase behavior. *Science* **1991**, *251*, 898-905.

(92) Yu, Y.; Zhang, L.; Eisenberg, A. Morphogenic Effect of Solvent on Crew-Cut Aggregates of Amphiphilic Diblock Copolymers. *Macromolecules* **1998**, *31*, 1144-1154.

(93) Bhargava, P. et al. Self-assembled Polystyrene-Block-Poly (Ethylene Oxide) Micelle Morphologies in Solution. *Macromolecules* **2006**, *39*, 4880-4888.

(94) Xu, Y.; Jin, S.; Xu, H.; Nagai, A.; Jiang, D. Conjugated Microporous Polymers: Design, Synthesis and Application. *Chem*. *Soc*. *Rev*. **2013**, *42*, 8012-8031.

(95) Taniguchi, I.; Duan, S.; Kai, T.; Kazama, S.; Jinnaiacd, H. Effect of the Phase-Separated Structure on CO2 Separation Performance of the Poly(Amidoamine) Dendrimer Immobilized in a Poly(Ethylene Glycol) Network. *J. Mater. Chem. A*, **2013**, *1*, 14514-14523.

(96) Grünewald, K.; Desai, P.; Winkler, D. C.; Heymann, J.B.; Belnap, D. M.; Baumeister, W.; Steven, A.C. Three-Dimensional Structure of Herpes Simplex Virus from Cryo-Electron Tomography. *Science* **2003**, *302*, 1396-1398.

(97) Radon J. Über die Bestimmung von Funktionen durch ihre Integralwerte längs gewisser Mannigfaltigkeiten. Berichte über die Verhandlungen der Königlich Sächsischen Gesellschaft der Wissenschaften zu Leipzig. Mathematisch-Physische KlasseSachs. **1917**, *69*, 262-277.

(98) Ersen, O.; Hirlimann, C.; Drillon, M.; Werckmann, J.; Tihay, F.; Pham-Huu, C.; Crucifix, C.; Schultz, P. 3D-TEM Characterization of Nanometric Objects. *Solid State Sciences* **2007**, *9*, 1088-1098.

(99) DeRosier, D. J.; Klug, A. Reconstruction of Three Dimentional Structures from Electron Micrographs. *Nature* **1968**, *217*, 130-134.

(100) Frank, J. Electron Tomography: Three Dimensional Imaging with the Transmission Electron Microscope, Plenum Press, **1992**.

(101) Lucic, V.; Forster, F.; Baumeister, W. Structural Studies by Electron Tomography: From Cells to Molecules. *Annual Review of Biochemistry* **2005**, *74*, 833-865.

(102) Frank, *J. Electron Tomography*: Methods for Three-Dimensional Visualization of Structures in the Cell. *Springer*; **2006**.

(103) Midgley, P. A.; Dunin-Borkowski, R. E. Electron Tomography and Holography in Materials Science. *Nature Materials* **2009**, *8*, 271-280.

(104) Nie, Z. H.; Petukhova, A.; Kumacheva, E. Properties and Emerging Applications of Self-assembled Structures Made from Inorganic Nanoparticles. *Nat*. *Nanotechnol*. **2010**, *5*, 15-25.

Lin, Y.; Daga, V. K.; Anderson, E. R.; Gido, S. P.; Watkins, J. J. Nanoparticle-Driven Assembly of Block Copolymers: A Simple Route to Ordered Hybrid Materials. *J. Am. Chem. Soc.* **2011**, *133*, 6513-6516.

(105) Warren, S. C.; DiSalvo, F. J.; Wiesner, U. Nanoparticle-tuned Assembly and Disassembly of Mesostructured Silica Hybrid. *Nature Materials* **2007**, *6*, 156-161.

(106) Liu, K.; Ahmed, A.; Chung, L.; Sugikawa, K.; Wu, G.; Nie, Z. H.; Gordon, G.; Kumacheva, E. In Situ Plasmonic Counter for Polymerization of Chains of Gold Nanorods in Solution. *ACS Nano* **2013**, *7*, 5901-5910.

(107) Zhu, Y.; Fan, L.; Yang, B.; Du, J. Multifunctional Homopolymer Vesicles for Facile Immobilization of Gold Nanoparticles and Effective Water Remediation. *ACS Nano* **2014**, *8*, 5022-5031.

(108) Lin, Y.; Daga, V. K.; Anderson, E. R.; Gido, S. P.; Watkins, J. J. Nanoparticle-Driven Assembly of Block Copolymers: A Simple Route to Ordered Hybrid Materials. *J. Am. Chem. Soc.* **2011**, *133*, 6513-6516.

(109) Hervés, P.; Pérez-Lorenzo, M.; Liz-Marzán, L. M.; Dzubiella, J.; Lu, Y.; Ballauff, M. Catalysis by Metallic Nanoparticles in Aqueous Solution: Model Reactions. *Chem. Soc. Rev.* **2012**, *41*, 5577-5587.

(110) Shine, H. J.; Mallory, H. E. Reduction of Aromatic Nitro Compounds by Potassium Borohydride, *J. Org. Chem.* **1962**, *27*, 2390.

(111) Mei, Y.; Lu, Y.; Polzer, F.; Ballauff, M.; Drechsler, M. Catalytic Activity of Palladium Nanoparticles Encapsulated in Spherical Polyelectrolyte Brushes and Core−Shell Microgels. *Chem. Mater.* **2007**, *19*, 1062-1069.

(112) Gu, S.; Wunder, S.; Lu, Y.; Ballauff, M.; Fenger, R.; Rademann, K.; Jaquet, B.; Zaccone, A. Kinetic Analysis of the Catalytic Reduction of 4-Nitrophenol by Metallic Nanoparticles. *J. Phys. Chem. C* **2014**, *118*, 18618-18625.

(113) Gu, S.; Lu, Y.; Kaiser, J.; Albrecht, M.; Balluaff, M.; Kinetic Analysis of The Reduction of 4-Nitrophenol Catalyzed by Au/Pd Nanoalloys Immobilized in Spherical Polyelectrolyte Brushes. *Phys. Chem. Chem. Phys* **2015**, *17*, 28137-28143.

(114) Gu, S.; Kaiser, J.; Marzum, C.; Ott, A.; Lu, Y.; Ballauff, M.; Zaccone, A.; Barcikowski, S.; Wagener, P. Ligand-free Gold Nanoparticles as a Reference Material for Kinetic Modelling of Catalytic Reduction of 4-Nitrophenol. *Catal Lett* **2015**, *145*, 5, 1105-1112.

(115) Yuan, J.; Wunder, S.; Warmuth, F.; Lu, Y. Spherical Polymer Brushes with Vinylimidazolium-Type Poly(ionic liquid) Chains as Support For Metallic Nanoparticles. *Polymer* **2012**, *53*, 43-49.

(116) Ghosh, S.K.; Mandal, M.; Kundu, S.; Nath, S.; Pal, T.; Bimetallic Pt-Ni Nanoparticles Can Catalyze Reduction of Aromatic Nitro Compounds by Sodium Borohydride in Aqueous Solution, *Appl. Catal. A* **2004**, *268*, 61.

(117) Hayakawa, K.; Yoshimura, T.; Esumi, K. Preparation of Gold-Dendrimer Nanocomposites by Laser Irradiation and Their Catalytic Reduction of 4-Nitrophenol, *Langmuir*, **2003**, 19, 5517-5521.

(118) Blaser, H. U. A Golden Boost to an Old Reaction. *Science* **2006**, *313*, 312-313.

(119) Corma, A.; Concepcion, P.; Serna, P. A Different Reaction Pathway for the Reduction of Aromatic Nitro Compounds on Gold Catalysts. *Angew. Chem.* **2007**, *119*, 7404-7407.

(120) Corma, A.; Serna, P. Chemoselective Hydrogenation of Nitro Compounds with Supported Gold Catalysts. *Science* **2006**, *313*, 332-4.

(121) Wunder, S.; Lu, Y.; Albrecht, M.; Ballauff, M. Catalytic Activity of Faceted Gold Nanoparticles Studied by a Model Reaction: Evidence for Substrate-Induced Surface Restructuring. *ACS Catal.* **2011**, *1*, 908-916.

(122) Wunder, S.; Polzer, F.; Lu,;Y.; Mei, Y.; Ballauff, M. Kinetic Analysis of Catalytic Reduction of 4-Nitrophenol by Metallic Nanoparticles Immobilized in Spherical Polyelectrolyte Brushes. *J. Phys. Chem. C* **2010**, *114*, 8814-8820.

(123) Noguera, C. Physics and Chemistry at Oxide Surfaces; Cambridge University Press: Cambridge, UK, **1996**.

(124) Wyckoff, R.W.G. Crystal Structures, 2nd ed; Wiley: New York, **1964**.

(125) Lee, J.; Orilall, M. C.; Warren, S. C.; Kamperman, M.; DiSalvo, F. J.; Wiesner, U. Direct Access to Thermally Stable and Highly Crystalline Mesoporous Transition-Metal Oxides with Uniform Pores. *Nat. Mater.* **2008**, *7*, 222-228.

(126) Orilall, M. C.; Matsumoto, F.; Zhou, Q.; Sai, H.; Abruña, H. D.; DiSalvo, F.J.; Wiesner, U. One-Pot Synthesis of Platinum-Based Nanoparticles Incorporated into Mesoporous Niobium Oxide-Carbon Composites for Fuel Cell Electrodes. *J. Am. Chem. Soc.* **2009**, *131*, 9389-9395.

(127) Crossland, E. J. W.; Kamperman, M.; Nedelcu, M.; Ducati, C.; Wiesner, U.; Smilgies, D. M.; Toombes, G. E. S.; Hillmyer, M. A.; Ludwigs, S.; Steiner, U.; Snaith, H. J. A Bicontinuous Double Gyroid Hybrid Solar Cell. *Nano Lett*. **2009**, *9*, 2807-2812.

(128) Hart, C. J.; Cuisinier, M.; Liang, X.; Kundu, D.; Garsuch, A.; Nazar, L. F. Rational Design of Sulphur Host Materials for Li-S Batteries: Correlating Lithium Polysulphide Adsorptivity and Self-discharge Capacity Loss. *Chem. Commun.* **2015**, *51*, 2308-2311.

(129) Seh, Z. W.; Li, W.; Cha, J. J.; Zheng, G; Yang, Y.; McDowell, M. T.; Hsu, P. C.; Cui, Y. Sulphur-$TiO_2$ Yolk-Shell Nanoarchitecture with Internal Void Space for Long-Cycle Lithium-Sulphur Batteries. *Nat*. *Commun*. **2013**, *4*, 1331.

(130) Ji, X.; Evers, S.; Black, R.; Nazar, L. F. Stabilizing Lithium-Sulphur Cathodes Using Polysulphide Reservoirs. *Nat*. *Commun*. **2011**, *2*, 325.

(131) Zhou, W.; Yu, Y.; Chen, H.; DiSalvo, F. J.; Abruña, H. D. J. Yolk-Shell Structure of Polyaniline-Coated Sulfur for Lithium-Sulfur Batteries. *Am. Chem. Soc.* **2013**, *135*, 16736-16743.

(132) Barchasz, C.; Lepretre J. C.; Alloin, F.; Patoux, S. New Insights into The Limiting Parameters of the Li/S Rechargeable Cell. *J. Power Sources* **2012**, *199*, 322-330.

(133) Mikhaylik, Y. V.; Akridge, J. R.; Low Temperature Performance of Li/S Batteries. *J. Electrochem. Soc.* **2004**, *151*,1969-1976.

(134) Wang, J.; Chew, S. Y.; Zhao, Z. W.; Ashraf, S.; Wexler, D.; Chen, J.; Ng, S. H.; Chou, S. L.; Liu, H. K. Sulfur-Mesoporous Carbon Composites in Conjunction With a Novel Ionic Liquid Electrolyte for Lithium Rechargeable Batteries. *Carbon* **2008**, *46*, 229-235.

(135) Zhang, Y.; Zhao, Y.; Sun, K. E.; Chen, P. Development in Lithium/Sulfur Secondary Batteries. *The Open Materials Science Journal* **2011**, *5*, 215-211.

(136) Jeon, B. H.; Yeon, J. H.; Chung, I. J. Preparation and Electrical Properties of Lithium-Sulfur-Composite Polymer Batteries. *J. Mater. Process. Technol.* **2003**, *143-144*, 93-97.

(137) Manthiram, A.; Fu, Y. Z.; Chung, S. H.; Zu, C. X.; Su, Y. S. Rechargeable Lithium−Sulfur Batteries. *Chem. Rev.* **2014**, *114*, 11751−11787.

(138) Jung Y.; Kim, S. New Approaches to Improve Cycle Life Characteristics of Lithium-Sulfur Cells. *Electrochem*. *Commun*. **2007**, *9*, 249-254.

(139) Bruce, P. G.; Freunberger, S. A.; Hardwick, L. J.; Tarascon, J.-M. Li-O2 and Li-S Batteries with High Energy Storage. *Nat*. *Mater*. **2012**, *11*, 19-29.

(140) Skotheim, T. A. High Capacity Cathodes for Secondary Cells. U.S. Patent 5, 460, 905, Oct 24, **1995**.

(141) Skotheim, T. A. High Capacity Cathodes for Secondary Cells. U.S. Patent 5, 462, 566, Oct 31, **1995**.

(142) Peramunage, D.; Licht, S. A Solid Sulfur Cathode for Aqueous Batteries. *Science* **1993**, *261*, 1029-1032.

(143) Chu, M.-Y. Rechargeable Positive Electrodes. U.S. Patent 5, 686, 201, Nov 11, **1997**.

(144) Mikhaylik, Y. V.; Skotheim, T. A.; Trofimov, B. A. Lithium Batteries. U.S. Patent 6, 936, 382, Aug 30, **2005**.

(145) Mikhaylik, Y. V.; Akridge, J. R. Polysulfide Shuttle Study in the Li/S Battery System. *J. Electrochem. Soc.* **2004**, *151*, A1969-1976.

(146) Zu C.; Manthiram, A. J. Stabilized Lithium-Metal Surface in a Polysulfide-Rich Environment of Lithium-Sulfur Batteries. *J. Phys. Chem. Lett.* **2014**, *5*, 2522-2527.

(147) Assary, R. S.; Curtiss L. A.; Moore, S. Toward a Molecular Understanding of Energetics in Li-S Batteries Using Nonaqueous Electrolytes: A High-Level Quantum Chemical Study. *J. Phys. Chem. C* **2014**, *118*, 11545-11558.

(148) Diao, Y.; Xie, K.; Xiong S.; Hong, X. Shuttle Phenomenon - the Irreversible Oxidation Mechanism of Sulfur Active Material in Li-S Battery. *J. Power Sources* **2013**, *235*, 181-186.

(149) Xiong, S.; Xie, K.; Diao Y.; Hong, X. Characterization of the Solid Electrolyte Interphase on Lithium Anode for Preventing the Shuttle Mechanism in Lithium-Sulfur Batteries. *J. Power Sources* **2014**, *246*, 840-845.

(150) Lécuyer, M.; Gaubicher, J.; Deschamps, M.; Lestriez, B.; Brousse T.; Guyomard, D. Structural Changes of A Li/S Rechargeable Cell in Lithium Metal Polymer Technology. *J. Power Sources* **2013**, *241*, 249-254.

(151) Hassoun, J.; Scrosati, B. Moving to a Solid-State Configuration: A Valid Approach to Making Lithium-Sulfur Batteries Viable for Practical Applications. *Adv. Mater.* **2010**, *22*, 5198-5201.

(152) Fu, Y. Z.; Su, Y. S.; Manthiram, A. Highly Reversible Lithium/Dissolved Polysulfide Batteries with Carbon Nanotube Electrodes. *Angew. Chem. Int. Ed.* **2013**, *52*, 6930-6935.

(153) Hayashi, A.; Ohtomo, T.; Mizuno, F.; Tadanaga, K.; Tatsumisago, All-Solid-State Li/S Batteries with Highly Conductive Glass-Ceramic Electrolytes. *M. Electrochem. Commun.* **2003**, *5*, 701-705.

(154) Su, Y. S.; Manthiram, A. Lithium-Sulphur Batteries with a Microporous Carbon Paper as A Bifunctional Interlayer. *Nat. Commun.* **2012**, *3*, 11661.

(155) Zhang, S. S. Role of LiNO3 in Rechargeable Lithium/Sulfur Battery. *Electrochim. Acta* **2012**, *70*, 344-348.

(156) Zhou, W.; Xiao, X.; Cai, M.; Yang, L. Polydopamine-Coated, Nitrogen-Doped, Hollow Carbon-Sulfur Double-Layered Core-Shell Structure for Improving Lithium-Sulfur Batteries. *Nano Lett.* **2014**, *14*, 5250-5256.

(157) Ji, X. L.; Lee, K. T.; Nazar, L. F. A Highly Ordered Nanostructured Carbon-Sulphur Cathode for Lithium-Sulphur Batteries. *Nat. Mater.* **2009**, *8*, 500-506.

(158) Peng, H. J.; Zhang, Q. Designing Host Materials for Sulfur Cathodes: From Physical Confinement to Surface Chemistry. *Angew. Chem Int. Ed.* **2015**, *54*, 11018-11020.

(159) Pang, Q.; Kundu, D.; Nazar, L. F. A Graphene-Like Metallic Cathode Host for Long-Life and High-Loading Lithium-Sulfur Batteries. *Mater. Horiz.* **2016**, *3*, 130-136.

(160) Hu, G.; Xu, C.; Sun, Z.; Wang, S.; Cheng, H. M.; Li, F.; Ren,W. 3D Graphene-Foam-Reduced-Graphene-Oxide Hybrid Nested Hierarchical Networks for High-Performance Li-S Batteries. *Adv. Mater.* **2016**, *28*, 1603-1609.

(161) Jayaprakash, N.; Shen, J.; Moganty, S. S.; Corona, A.; Archer, L. A. Porous Hollow Carbon@Sulfur Composites for High-Power Lithium-Sulfur Batteries. *Angew. Chem. Int. Ed.* **2011**, *50*, 5904-5908.

(162) Yao, C., Li, F., Li, X. & Xia, D. Fiber-like Nanostructured $Ti_4O_7$ Used as Durable Fuel Cell Catalyst Support in Oxygen Reduction Catalysis. *J. Mater. Chem.* **2012**, *22*, 16560-16565.

(163) Xiao, Z. B.; Yang, Z.; Wang, L.; Nie, H. G.; Zhong, M. E.; Lai, Q. Q.; Xu, X. J.; Zhang, L. J.; Huang, S. M. A Lightweight $TiO_2$/Graphene Interlayer, Applied as a Highly Effective Polysulfide Absorbent for Fast, Long-Life Lithium-Sulfur Batteries. *Adv. Mater.* **2015**, *27*, 2891-2898.

(164) Ding, B.; Shen, L. F.; Xu, G. Y.; Nie, P.; Zhang, X. G. Encapsulating Sulfur into Mesoporous $TiO_2$ Host as A High Performance Cathode for Lithium-Sulfur Battery. *Electrochim*. *Acta* **2013**, *107*, 78-74.

(165) Zhang, Z.; Li, Q.; Jiang, S. F.; Zhang, K.; Lai, Y. Q.; Li, J. Sulfur Encapsulated in a $TiO_2$-Anchored Hollow Carbon Nanofiber Hybrid Nanostructure for Lithium-Sulfur Batteries. *Chem.-a Eur. J.* **2015**, *21*, 1343-1349.

(166) Liang X.; Nazar, L. F. In Situ Reactive Assembly of Scalable Core-Shell Sulfur-MnO2 Composite Cathodes. *ACS Nano* **2016***, 10,* 4192-4198.

(167) Liang, X.; Hart, C.; Pang, Q.; Garsuch, A.; Weiss, T.; Nazar, L. F. A Highly Efficient Polysulfide Mediator for Lithium-Sulfur Batteries. *Nat*. *Commun*. **2015**, *6*, 56821-8.

(168) Yao, C. H.; Li, F.; Li, X.; Xia, D. G. Fiber-like Nanostructured $Ti_4O_7$ Used as Durable Fuel Cell Catalyst Support In Oxygen Reduction Catalysis. *J. Mater. Chem*. **2012**, *22*, 16560-1565.

(169) Bartholomew, R. F.; Frankl, D. R. Electrical Properties of Some Titanium Oxides. *Phys*. *Rev*. **1969**, *187*, 828-833.

(170) Walsh, F. C.; Wills, R. G. The Continuing Development of Magnéli Phase Titanium Sub-Oxides and Ebonex® Electrodes. *A. Electrochim. Acta* **2010**, *55*, 6342-6351.

(171) Chen, G.; Bare S. R.; Mallouk, T. E. Development of Supported Bifunctional Electrocatalysts for Unitized Regenerative Fuel Cells. *J. Electrochem. Soc.* **2002**, *149*, 1092-1099.

(172) Li, W.; Liu, S.; Deng, R.; Wang, J.; Nie, Z.; Zhu, J. A Simple Route to Improve Inorganic Nanoparticles Loading Efficiency in Block Copolymer Micelles. *Macromolecules* **2013**, *46*, 2282-2291.

(173) Halevi, A.; Halivni, S.; Oded, M.; Müller, A. H. E.; Banin, U.; Shenhar, R. Co-Assembly of A-B Diblock Copolymers with B′-type Nanoparticles in Thin Films: Effect of Copolymer Composition and Nanoparticle Shape. *Macromolecules* **2014**, *47*, 3022-3032.

(174) Jang, S. G.; Kramer, E. J.; Hawker, C. J. Controlled Supramolecular Assembly of Micelle-Like Gold Nanoparticles in PS-*b*-P2VP DiBlock Copolymers via Hydrogen Bonding. *J. Am. Chem. Soc.* **2011**, *133*, 16986-16996.

(175) Nie, Z. H.; Petukhova, A.; Kumacheva, E. Properties and Emerging Applications of Self-assembled Structures Made from Inorganic Nanoparticles. *Nat. Nanotechnol.* **2010**, *5*, 15-25.

(176) Liu, K.; Ahmed, A.; Chung, L.; Sugikawa, K.; Wu, G.; Nie, Z. H.; Gordon, G.; Kumacheva, E. In Situ Plasmonic Counter for Polymerization of Chains of Gold Nanorods in Solution. *ACS Nano* **2013**, *7*, 5901-5910.

(177) Warren, S. C.; DiSalvo, F. J.; Wiesner, U. Nanoparticle-tuned Assembly and Disassembly of Mesostructured Silica Hybrid. *Nat. Mater.* **2007**, *6*, 156-161.

(178) Lin, Y.; Daga, V. K.; Anderson, E. R.; Gido, S. P.; Watkins, J. J. Nanoparticle-Driven Assembly of Block Copolymers: A Simple Route to Ordered Hybrid Materials. *J. Am. Chem. Soc.* **2011**, *133*, 6513-6516.

(179) Chen, G.; Wang, Y.; Yang, M.; Xu, J.; Goh, S. J.; Pan, M.; Chen, H. Measuring Ensemble-Averaged Surface-Enhanced Raman Scattering in the Hotspots of Colloidal Nanoparticle Dimers and Trimers. *J. Am. Chem. Soc.* **2010**, *132*, 3644-3645.

(180) Mai, Y.; Eisenberg, A. Controlled Incorporation of Particles into the Central Portion of Vesicle Walls. *J. Am*. *Chem*. *Soc*. **2010**, *132*, 10078-10084.

(181) Yabu, H.; Jinno, T.; Koike, K.; Higuchi, T.; Shimomura, M. Nanoparticle Arrangements in Block Copolymer Particles with Microphase-Separated Structures. *J. Polym. Sci. Pol. Phys.* **2011**, *49*, 1717-1722.

(182) Yabu, H.; Koike, K.; Motoyoshi, K.; Higuchi, T.; Shimomura, M. A Novel Route for Fabricating Metal-Polymer Composite Nanoparticles with Phase-Separated Structures. *Macromol. Rapid Commun*. **2010**, *31*, 1267-1271.

(183) Zhu, J.; Hayward, R. C. Spontaneous Generation of Amphiphilic Block Copolymer Micelles with Multiple Morphologies through Interfacial Instabilities. *J. Am. Chem. Soc.* **2008**, *130*, 7496-7502.

(184) Chen, H. Y.; Abraham, S.; Mendenhall, J.; Delamarre, S. C.; Smith, K.; Kim, I.; Batt, C. A. Encapsulation of Single Small Gold Nanoparticles by Diblock Copolymers. *ChemPhysChem* **2008**, *9*, 388-392.

(185) Li, W.; Liu, S.; Deng, R.; Zhu, J. Encapsulation of Nanoparticles in Block Copolymer Micellar Aggregates by Directed Supramolecular Assembly. *Angew. Chem. Int. Ed*. **2011**, *50*, 5865-5868.

(186) Jang, S. G.; Audus, D. J.; Klinger, D.; Krogstad, D. V.; Kim, B. J.; Cameron, A.; Kim, S. W.; Delaney, K. T.; Hur, S. M.; Killops, K. L.; Fredrickson, G. H.; Kramer, E. J.; Hawker, C. J. Striped, Ellipsoidal Particles by Controlled Assembly of Diblock Copolymers. *J. Am. Chem. Soc.* **2013**, *135*, 6649-6657.

(187) Yabu, H.; Jinno, T.; Koike, K.; Higuchi, T.; Shimomura, M. Three-Dimensional Assembly of Gold Nanoparticles in Spherically Confined Microphase-Separation Structures of Block Copolymers. *Macromolecules* **2011**, *44*, 5868-5873.

(188) Liang, R.; Xu, J.; Deng, R.; Wang, K.; Liu, S.; Li, J.; Zhu, J. Assembly of Polymer-Tethered Gold Nanoparticles under Cylindrical Confinement. *ACS Macro Lett*. **2014**, *3*, 486-490.

(189) Martin, C. R. Membrane-Based Synthesis of Nanomaterials. *Chem. Mater.* **1996**, *8*, 1739-1746.

(190) Feng X. D.; Jin, Z. X. Spontaneous Formation of Nanoscale Polymer Spheres, Capsules, or Rods by Evaporation of Polymer Solutions in Cylindrical Alumina Nanopores. *Macromolecules* **2009**, *42*, 569-572.

(191) Teranishi, T.; Hasegawa, S.; Shimizu, T.; Miyake, M. Heat-Induced Size Evolution of Gold Nanoparticles in the Solid State. *Adv. Mater*. **2001**, *13*, 1699-1701.

(192) Wiley, B.; Sun, Y.; Xia, Y. Synthesis of Silver Nanostructures with Controlled Shapes and Properties. *Acc. Chem. Res*. **2007**, *40*, 1067-1076.

(193) Daniel, M. C.; Astruc, D. Gold Nanoparticles: Assembly, Supramolecular Chemistry, Quantum-Size-Related Properties, and Applications toward Biology, Catalysis, and Nanotechnology. *Chem. Rev*. **2004**, *104*, 293-346.

(194) Cortie, M. B.; McDonagh, A. M. Synthesis and Optical Properties of Hybrid and Alloy Plasmonic Nanoparticles. *Chem. Rev*. **2011**, *111*, 3713-3735.

(195) Kulbaba, K.; MacLachlan, M. J.; Evans, C. E. B.; Manners, I. Organometallic Gels: Characterization and Electrochemical Studies of Swellable, Thermally Crosslinked Poly(ferrocenylsilane)s. Macromol. *Chem. Phys*. **2001**, *202*, 1768-1775.

(196) Barton, Handbook of Solubility Parameters, CRC Press, **1983**.

(197) Jain, P. K.; Huang, W.; El-Sayed, M. A. On the Universal Scaling Behavior of the Distance Decay of Plasmon Coupling in Metal Nanoparticle Pairs: A Plasmon Ruler Equation. *Nano Lett*. **2007**, *7*, 2080-2088.

(198) Lazarides, A. A.; Schatz, G. C. DNA-Linked Metal Nanosphere Materials: Structural Basis for the Optical Properties. *J. Phys. Chem. B* **2000**, *104*, 460-467.

(199) Bhandari, R.; Knecht, M. R. Effects of the Material Structure on the Catalytic Activity of Peptide-Templated Pd Nanomaterials. *ACS Catal*, **2011**, *1*, 89-98.

(200) Behrens, S.; Heyman, A.; Maul, R.; Essig, S.; Steigerwald, S.; Quintilla, A. et al. Constrained Synthesis and Organization of Catalytically Active Metal Nanoparticles by Self-Assembled Protein Templates. *Adv Mater*, **2009**, *21*, 3515-3519.

(201) Esumi, K.; Isono, R.; Yoshimura, T. Preparation of PAMAM− and PPI−Metal (Silver, Platinum, and Palladium) Nanocomposites and Their Catalytic Activities for Reduction of 4-Nitrophenol. *Langmuir*, **2004**, *20*, 237-243.

(202) Kim, S.-W.; Kim, M.; Lee, W. Y.; Hyeon, T. Fabrication of Hollow Palladium Spheres and Their Successful Application to the Recyclable Heterogeneous Catalyst for Suzuki Coupling Reactions. *J. Am. Chem. Soc.* **2002**, *124*, 7642-7643.

(203) Tang, S. H.; Huang, X. Q.; Chen, X. L.; Zheng, N. F. Hollow Mesoporous Zirconia Nanocapsules for Drug Delivery. *Adv. Funct. Mater.* **2010**, *20*, 2442-2447.

(204) Liu, Q. M.; Du, J. Z. Multifunctional Polymer Vesicles for Cancer Stem Cells-Targeted Drug/siRNA Therapy. *Cancer Cell & Microenvironment* **2016**, *3*, 1145.

(205) Gao, C. B.; Zhang, Q.; Lu, Z. D.; Yin, Y. D. Templated Synthesis of Metal Nanorods in Silica Nanotubes. *J. Am.Chem. Soc.* **2011**, *133*, 19706-19709.

(206) Sun, Y. G.; Mayers, B.; Xia, Y. N. Metal Nanostructures with Hollow Interiors. *Adv. Mater.* **2003**, *15*, 641-646.

(207) Goldberger, J.; He, R. R.; Zhang, Y. F.; Lee, S. W.; Yan, H. Q.; Choi, H. J.; Yang, P. D. Single-Crystal Gallium Nitride Nanotubes. *Nature* **2003**, *422*, 599-602.

(208) Lou, X. W.; Archer, L. A.; Yang, Z. C. Hollow Micro-/Nanostructures: Synthesis and Applications. *Adv. Mater.* **2008**, *20*, 3987-4019.

(209) An, K.; Hyeon, T. Synthesis and Biomedical Applications of Hollow Nanostructures. *Nano Today* **2009**, *4*, 359-373.

(210) Yao, Y.; McDowell, M. T.; Ryu, I.; Wu, H.; Liu, N.; Hu, L. B.; Nix, W. D.; Cui, Y. Interconnected Silicon Hollow Nanospheres for Lithium-Ion Battery Anodes with Long Cycle Life. *Nano Lett.* **2011**, *11*, 2949-2954.

(211) Fang, X.; Liu, Z.; Hsieh, M.; Chen, M.; Liu, P.; Chen, C.; Zheng, N. Hollow Mesoporous Aluminosilica Spheres with Perpendicular Pore Channels as Catalytic Nanoreactors. *ACS Nano* **2012**, *6*, 4434-4444.

(212) Zhao, Y.; Sakai, F.; Su, L.; Liu, Y. J.; Wei, K. C.; Chen, G.S.; Jiang, M. Progressive Macromolecular Self-Assembly: From Biomimetic Chemistry to Bio-Inspired Materials. *Adv. Mater.* **2013**, *25*, 5215-5256.

(213) Mohammadnezhad, G.; Akintola, O.; Plass, W.; Schacher, F. H.; Steiniger, F.; Westermann, M. Facile Synthesis of Highly Thermally Stable Nanoporous γ-Aluminas from Aluminum Alkoxide Precursors. *RSC Adv.*, **2015**, *5*, 49493-49499.

(214) Robbins, S. W.; Beaucage, P. A.; Sai, H.; Tan, K. W.; Werner, J. G.; Sethna, J. P.; DiSalvo, F. J.; Gruner, S. M.; Van Dover, R. B.; Wiesner, U. Block Copolymer Self-assembly Directed Synthesis of Mesoporous Gyroidal Superconductors. *Science Advances* **2016**, *2*, 1501119.

(215) Lee, H.; Dellatore, S. M.; Miller, W. M.; Messersmith, P. B. Mussel-Inspired Surface Chemistry for Multifunctional Coatings. *Science* **2007**, *318*, 426-430.

(216) Luo, J.; Zhang, N.; Liu, R.; Liu, X. *In Situ* Green Synthesis of Au Nanoparticles onto Polydopamine-Functionalized Graphene for Catalytic Reduction of Nitrophenol. *RSC Adv.* **2014**, *4*, 64816-64824.

(217) Yu, B.; Wang, D. A.; Ye, Q.; Zhou, F.; Liu, W. M. Robust Polydopamine Nano/Microcapsules and their Loading and Release Behavior. *Chem. Commun.* **2009**, *44*, 6789-6791.

(218) Liu, Q. Z.; Yu, B.; Ye, W. C.; Zhou, F. Highly Selective Uptake and Release of Charged Molecules by pH-Responsive Polydopamine Microcapsules. *Macromol. Biosc.* **2011**, *11*, 1227-1234.

(219) Ai, K. L.; Liu, Y. L.; Ruan, C. P.; Lu, L. H.; Lu, G. Q. Sp2 C-Dominant N-Doped Carbon Sub-Micrometer Spheres with A Tunable Size: A Versatile Platform For Highly Efficient Oxygen-Reduction Catalysts. *Adv. Mater*. **2013**, *25*, 998-1003.

(220) Cui, J.; Wang, Y.; Postma, A.; Hao, J.; Hosta-Rigau, L.; Caruso, Monodisperse Polymer Capsules: Tailoring Size, Shell Thickness, and Hydrophobic Cargo Loading via Emulsion Templating. F. Adv. Funct. Mater. **2010**, 20, 1625-1631.

(221) Zhao, Y.; Jiang, L. Hollow Micro/Nanomaterials with Multilevel Interior Structures. *Adv. Mater.* **2009**, *21*, 3621-3638.

(222) Lou, X. W.; Yuan, C.; Archer, L. A. Double-Walled SnO2 Nano-Cocoons with Movable Magnetic Cores. *Adv. Mater.* **2007**, *19*, 3328-3332.

(223) Tan, L. F.; Chen, D.; Liu, H. Y.; Tang, F. Q. A Silica Nanorattle with a Mesoporous Shell: An Ideal Nanoreactor for the Preparation of Tunable Gold Cores. *Adv. Mater.* **2010**, *22*, 4885-4889.

(224) Park, J. C.; Song, H. Metal@Silica Yolk-Shell Nanostructures as Versatile Bifunctional Nanocatalysts. *Nano Res*. **2011**, *4*, 33-49.

(225) Khlobystov, A. N. Carbon Nanotubes: From Nano Test Tube to Nano-Reactor. *ACS Nano* **2011**, *5*, 9306-9312.

(226) Liu, X. C.; Wang, G. C.; Liang, R. P.; Shi, L.; Qiu, J. D. Environment-Friendly Facile Synthesis of Pt Nanoparticles Supported on Polydopamine Modified carbon Materials. *J. Mater*. *Chem*. A **2013**, *1*, 3945-3953.

(227) Lee, H.; Fho, J.; Messersmith, P. B. Facile Conjugation of Biomolecules onto Surfaces via Mussel Adhesive Protein Inspired Coatings. *Adv. Mater.* **2009**, *21*, 431-434.

(228) Müller, M.; Torger, B.; Bittrich, E.; Kaul, E.; Lonov, L.; Uhlmann, P.; Stamm, M. In-Situ ATR-FTIR for Characterization of Thin Biorelated Polymer Films. *Thin Solid Films* **2014**, *556*, 1-8.

(229) Angioletti-Uberti, S.; Lu, Y.; Ballauff, M.; Dzubiella, J. Theory of Solvation-Controlled Reactions in Stimuli-Responsive Nanoreactors. *J. Phys. Chem. C* **2015**, *119*, 15723-15730.

(230) Gokmen, M. T.; Du Prez, F. E. Porous Polymer Particles—A Comprehensive Guide to Synthesis, Characterization, Functionalization and Applications. *Prog*. *Polym*. *Sci*. **2012**, *37*, 365-405.

(231) Wei, J.; Yue, Q.; Sun, Z.; Deng, Y.; Yhao, D. Synthesis of Dual-Mesoporous Silica Using Non-Ionic DiBlock Copolymer and Cationic Surfactant as Co-Templates. *Angew. Chem. Int. Ed.* **2012**, *51*, 6149-6153.

(232) Hata, H.; Saeki, S.; Kimura, T.; Sugahara, Y.; Kuroda, K. Adsorption of Taxol into Ordered Mesoporous Silicas with Various Pore Diameters. *Chem*. *Mater*. **1999**, *11*, 1110-1119.

(233) Davies, O. R.; Marlow, M.; Stolnik, S. Macroporous surface modified microparticles. *Soft Matter* **2008**, *4*, 1597-1601.

(234) Vanbever, R.; Mintzes, J. D.; Wang, J.; Nice, J.; Chen, D.; Batycky, R.; Langer, R.; Edwards, D. A. Formulation and physical characterization of large porous particles for inhalation. *Pharm*. *Res*. **1999**, *16*, 1735-1742.

(235) Vallet-Regí, M.; Balas, F.; Arcos, D. Mesoporous Materials for Drug Delivery. *Angew*. *Chem*. *Int*. *Ed*. **2007**, *46*, 7548-7558.

(236) Edwards, D. A.; Hanes, J.; Caponetti, G.; Hrkach, J.; Ben-Jebria, A.; Lou Eskew, M.; Mintzes, J.; Deaver, D.; Lotan, N.; Langer, R. Large Porous Particles for Pulmonary Drug Delivery. *Science* **1997**, *276*, 1868-1872.

(237) Xie, K.; Qin, X.; Wang, X.; Wang, Y.; Tao, H.; Wu, Q.; Yang, L.; Hu, Z. Carbon Nanocages as Supercapacitor Electrode Materials. *Adv*. *Mater*. **2012**, *24*, 347-352.

(238) Cho, S.; Shin, K. H.; Jang, J. Enhanced Electrochemical Performance of Highly Porous Supercapacitor Electrodes Based on Solution Processed Polyaniline Thin Films. *ACS Appl. Mater. Interfaces* **2013**, *5*, 9186-9193.

(239) Manthiram, A.; Fu, Y.; Chung, S. H.; Zu, C.; Su, Y. S. Rechargeable Lithium-Sulfur Batteries. *Chem. Rev.* **2014**, *114*, 11751-11787.

(240) Kim, H.; Lee, J.; Ahn, H.; Kim, O.; Park, M. J. Synthesis of Three-Dimensionally Interconnected Sulfur-Rich Polymers for Cathode Materials of High-Rate Lithium-Sulfur Batteries. *Nat. Commun.* **2015**, *6*, 7278.

(241) Cai, Y.; Chen, Y.; Hong, X.; Liu, Z.; Yuan, W. Porous Microsphere and Its Applications. *Int. J. Nanomed*. **2013**, *8*, 1111-1120.

(242) Lim, C. S.; Seok, S.; Im, S. H. Synthesis of Uniform PS-*b*-P2VP Nanoparticles via Reprecipitation and Their Use as Sacrificial Templates for Inorganic Hollow Nanoparticles. *J. Mater. Chem.* **2012**, ***22***, 8772-8774.

(243) Tang, J.; Liu, J.; Li, Y.; Tade, M. O.; Dai, S.; Yamauchi, Y. Synthesis of Nitrogen-Doped Mesoporous Carbon Spheres with Extra-Large Pores Through Assembly Of Diblock Copolymer Micelles. *Angew. Chem. Int. Ed*. **2015**, *54*, 588-593.

(244) Niu, D.; Liu, Z.; Li; Y.; Luo, X.; Zhang, J.; Gong, J.; Shi, J. Monodispersed and Ordered Large-Pore Mesoporous Silica Nanospheres with Tunable Pore Structure for Magnetic Functionalization and Gene Delivery. *Adv*. *Mater*. **2014**, *26*, 4947-4953.

(245) Wei, H.; Rodriguez, E. F.; Best, A. S.; Hollenkamp, A. F.; Chen, D.; Caruso, R. A. Chemical Bonding and Physical Trapping of Sulfur in Mesoporous Magnéli $Ti_4O_7$ Microspheres for High-Performance Li-S Batteries. Adv. Energy Mater. **2017**, *7*, 1601616.

(246) Yao, C. H.; Li, F.; Li, X.; Xia, D. G. Fiber-Like Nanostructured $Ti_4O_7$ Used as Durable Fuel Cell Catalyst Support in Oxygen Reduction Catalysis. *J. Mater. Chem*. **2012**, *22*, 16560-1565.

(247) Bartholomew, R. F.; Frankl, D. R. Electrical Properties of Some Titanium Oxides. *Phys*. *Rev*. **1969**, *187*, 828-833.

(248) Walsh, F. C.; Wills, R. G. The Continuing Development of Magnéli Phase Titanium Sub-Oxides and Ebonex® Electrodes. *A. Electrochim. Acta* **2010**, *55*, 6342-6351.

(249) Xiao, Z. B.; Yang, Z.; Wang, L.; Nie, H. G.; Zhong, M. E.; Lai, Q. Q.; Xu, X. J.; Zhang, L. J.; Huang, S. M. A Lightweight $TiO_2$/Graphene Interlayer, Applied as a Highly Effective Polysulfide Absorbent for Fast, Long-Life Lithium-Sulfur Batteries. *Adv*. *Mater*. **2015**, *27*, 2891-2898.

(250) Ding, B.; Shen, L. F.; Xu, G. Y.; Nie, P.; Zhang, X. G. Encapsulating Sulfur into Mesoporous $TiO_2$ Host as A High Performance Cathode for Lithium-Sulfur Battery. *Electrochim*. *Acta* **2013**, *107*, 78-74.

(251) Zhang, Z.; Li, Q.; Jiang, S. F.; Zhang, K.; Lai, Y. Q.; Li, J. Sulfur Encapsulated in a $TiO_2$-Anchored Hollow Carbon Nanofiber Hybrid Nanostructure for Lithium-Sulfur Batteries. *Chem*.-*a Eur. J.* **2015**, *21*, 1343-1349.

(252) Ioroi, T.; Siroma, Z.; Fujiwara, N.; Yamazaki, S.; Yasuda, K. Sub-Stoichiometric Titanium Oxide-Supported Platinum Electrocatalyst for Polymer Electrolyte Fuel Cells. *Electrochem*. *Commun*. **2005**, *7*, 183-188.

(253) Toyoda, M.; Yano, T.; Tryba, B.; Mozia, S.; Tsumura Y.; Inagaki, M. Preparation of Carbon-Coated Magneli Phases TinO2n−1 and their Photocatalytic Activity under Visible Light. *Appl*. *Catal*. *B* **2009**, *88*, 160-164.

(254) Qian, Q. P.; Huang, X. P.; Zhang, X. Y.; Xie, Z. G.; Wang, Y. P. One-Step Preparation of Macroporous Polymer Particles with Multiple Interconnected Chambers: A Candidate for Trapping Biomacromolecules. *Angew*. *Chem*. *Int*. *Ed*. **2013**, *52*, 10625-10629.

(255) Ma, H.G.; Sone, H.; Omi, S. Preparation of Uniform-Sized Polystyrene−Polyacrylamide Composite Microspheres from A W/O/W Emulsion By Membrane Emulsification Technique and Subsequent Suspension Polymerization. *Macromolicules* **2004**, *37*, 2954-2964.

(256) Li, J.; Wang, Y. H.; Zhang, C. L.; Liang, F. X.; Qu, X. Z.; Li, J. L.; Wang, Q.; Qiu, D.; Yang, Z. Z. Janus Polymeric Cages. *Polymer* **2012**, *53*, 3712-3718.

(257) Yoldas, B. E. Hydrolysis of Titanium Alkoxide and Effects of Hydrolytic Polycondensation Parameters. *J. Mater. Sci*. **1986**, *21*, 1087-1092.

(258) Hague, D. C.; Mayo, M. J. Controlling Crystallinity During Processing of Nanocrystalline Titania. *J. Am. Ceram*. *Soc*. **1994**, *77*, 1957-1960.

(259) Kim, J.; Song, K. C.; Pratsinis, S. E. The Effect of Hydrolysis Temperature On Synthesis of Bimodally Nanostructured Porous Titania. *J. Nanopart. Res*. **2000**, *2*, 419-424.

(260) Song, K. C.; Pratsinis, S. E. Synthesis of Bimodally Porous Titania Powders by Hydrolysis of Titanium Tetraisopropoxide. *J. Mater*. *Res*. **2000**, *15*, 2322-2329.

(261) Cheon, S.E., Kwon, C.W., Kim, D.B., Hong, S.J., Kim, H.T. and Kim, S.W. Effect of Binary Conductive Agents in $LiCoO_2$ Cathode on Performance of Lithium Ion Polymer Battery. *Electrochimica Acta* **2000**, *46*, 599-605.

(262) Zheng, H., Yang, R., Liu, G., Song, X.G. and Battaglia, V.S. Cooperation between Active Material, Polymeric Binder and Conductive Carbon Additive in Lithium Ion Battery Cathode. *The Journal of Physical Chemistry A* **2012**, *116*, 4875-4822.

(263) Yoshio, M., Brodd, R.J. Kozawa, A. Lithium-Ion Batteries Science And Technologies. Springer, New York, **2009**, 183-185.

(264) Lee, G.W., Ryu, J.H., Han, W.J., Ahn, K.H. and Oh, S.M. Effect of Slurry Preparation Process on Electrochemical Performances of $LiC_OO_2$ Composite Electrode. *Journal of Power Sources* **2010**, *195*, 6049-6054.

(265) Kim, K.M., Jeon, W.S., Chun, I.J. and Chang, S.H. Effect of Mixing Sequences on the Electrode Characteristics of Lithium-Ion Rechargeable Batteries. *Journal of Power Sources* **1999**, *83*, 108-113.

(266) Ponrouch, A. and Palacin, M.R. On the Impact of the Slurry Mixing Procedure in the Electrochemical Performance of Composite Electrodes for Li-Ion Batteries: A Case Study for Mesocarbon Microbeads (MCMB) Graphite and Co3O4. *Journal of Power Sources* **2011**, *196*, 9682-9688.

(267) Xiao, Z. B.; Yang, Z.; Wang, L.; Nie, H. G.; Zhong, M. E.; Lai, Q. Q.; Xu, X. J.; Zhang, L. J.; Huang,S. M. A Lightweight $TiO_2$/Graphene Interlayer, Applied as a Highly Effective Polysulfide Absorbent for Fast, Long-Life Lithium-Sulfur Batteries: *Adv*. *Mater*. **2015**, 27, 2891-8.

(268) Zhou, W. D.; Yu, Y. C.; Chen, H. F.; DiSalvo, J.; Abruna, H. D. olk-Shell Structure of Polyaniline-Coated Sulfur for Lithium-Sulfur Batteries. *J. Am. Chem. Soc.* **2013**, *135*, 16736-167434.
(269) Liang, Z.; Zheng, G. Y.; Li, W. Y.; Seh, Z. W.; Yao, H.; Yan, K.; Kong, D.; Cui, Y. Sulfur Cathodes with Hydrogen Reduced Titanium Dioxide Inverse Opal Structure. *ACS Nano* **2014**, *8*, 5249-5256.

# List of Figures

# List of Tables

# List of Abbreviations

| | |
|---|---|
| AAO | Anodic aluminum oxide |
| ALD | Atomic layer deposition |
| BCC | Body-centered cubic |
| BCP | Block copolymer |
| BET | The Brunauer-Emmett-Teller |
| CV | Cyclic voltammetry |
| D | Diameter of the particles |
| DMPO | 5,5-Dimethyl-pyrrdine N-oxide |
| DT-Au | Dodecanethiol-gold |
| EDX | Energy-dispersive X-ray spectroscopy |
| Eqs | Equations |
| ET | Electron tomography |
| FI-IR | Fourier transform infrared spectroscopy |
| FT | Fourier transform |
| IFT | Inverse Fourier transform |
| $L_0$ | The feature spacing of the phase-separated periodic domains |
| Li-S | Lithium-sulphur |
| LiTFSI | Bis(trifluoromethane) sulfonimide lithium salt |
| Nip | 4-Nitrophenol |
| NMP | N-methyl-2-pyrrolidone |
| NPs | Nanoparticles |
| PDA | Polydopamine |

| | |
|---|---|
| PDMS | Poly(dimethylsiloxane) |
| PS-P2VP | Poly(styrene-2-vinylpyridine) |
| PS-PAA | Polystyrene-b-poly(acrylic acid) |
| PS-PB | Polystyrene-b-polybutadiene |
| PS-PEO | Polystyrene-b-poly(ethylene oxide) |
| PS-PEO | Poly(styrene-ethylene oxide) |
| PS-PFMA | Polystyrene-b-poly(perfluorooctylethyl methacrylate) |
| PS-PMMA | Polystyrene-b-4-(perfluorooctylpropyloxy) -styrene |
| PVDF | Polyvinylidene fluoride |
| SDS | Sodium dodecyl sulfate |
| SEM | Scanning electron microscope |
| SERS | Raman scattering |
| SNR | Signal-to-noise ratio |
| SPB | Spherical polyelectrolyte brushes |
| TEM | Transmission electron microscopy |
| TGA | Thermogravimetric analysis |
| THF | Tetrahydrofuran |
| TIP | Titanium isopropoxide |
| UV-vis | Ultraviolet-visible spectroscopy |
| WBP | Weighted Backprojection |
| XRD | X-ray diffraction |
| $M_n$ | The number average molecular weight |
| Tg | Glass transition temperature |

| | |
|---|---|
| $\chi$ | Flory-Huggins interaction parameter |
| $N$ | The total chain length |
| $f$ | The volume fraction of one block |
| $\rho$ | Density |
| $S$ | Surface area |
| $\gamma$ | Surface tension |
| $R$ | Radius of liquid cylinder |
| $b$ | Radius of droplets |
| $\lambda$ | Wavelength |
| $e$ | Thickness of polymer film |
| $\tau_M$ | Characteristic time |
| $\eta$ | Viscosity |
| $\delta$ | Solubility parameter |
| $k_{tot}^{-1}$ | The total catalytic reaction time |
| $k_D^{-1}$ | The time for the reactant to diffuse to the gold nanoparticles |
| $k_S^{-1}$ | The time to get reduced by sodium borohydride $NaBH_4$ |
| $k_{D0}^{-1}$ | The time of diffusion from the bulk to the nanoreactor |
| $k_{Dg}^{-1}$ | The time of diffusion from the outer surface of the PDA shell to the surface of a gold nanoparticle |
| $k_S$ | The surface reaction rate |
| $c_{Nip,g}$ | The 4-nitrophenol concentration in the nanoreactor next to the gold nanoparticles |
| $k_{vol}$ | The fraction per unit time of the 4-nitrophenol molecules that are reduced by $NaBH_4$ |

| | |
|---|---|
| $\Delta V$ | The volume of the shell next to the gold nanoparticle |
| $t_0$ | Induction time |
| $k_{app}$ | Apparent rate constant |
| $S$ | Total surface of all metal nanoparticles |
| $k_1$ | Normalized kinetic constant Hx 4-hydroxylaminophenol Amp 4-aminophenol |
| $k_a$ | Reaction rate of step A |
| $\theta_{Nip}$ | Surface coverage of the particles by Nip |
| $\theta_{BH4}$ | Surface coverage of the nanoparticles by borohydride |
| $c_{Nip}$ | Actual concentrations of Nip |
| $c_{Hx}$ | Actual concentrations of 4-hydroxylaminophenol |
| $c_{BH4}$ | Actual concentrations of brohydride |
| $K$ | Langmuir adsorption constants |
| $k_b$ | Reaction rate of step B NB Nitrobenzene |
| $c_0$ | Concentration of reactant in the bulk solution |

# Publicaton List

(1) **Shilin Mei**, Jie Cao and Yan Lu*, Controllable assembly of two types of metal nanoparticles onto block copolymer nanospheres with ordered spatial distribution, *J. Mater. Chem. A*, **2015**, *3*, 3382-3389.

(2) **Shilin Mei**, Zdravko Kochovski, Rafael Roa, Joachim Dzubiella, Sasa Gu, Mathias Ballauff, Yan Lu*, Block copolymer template directed synthesis of polydopamine@gold nanoreactors with interconnected channel structure, ***to be submited***

(3) **Shilin Mei**, Charl Jafta, Iver Lauermann, Qidi Ran, Mattias Ballauff, Yan Lu*, Porous $Ti_4O_7$ nanoparticles with interconnected channel structure and their application as cathode materials for lithium-sulfur batteries, *Adv. Funct. Mater.* **2017**, accepted.

(4) Jie Cao, **Shilin Mei**, He Jia, Andreas Ott, Matthias Ballauff, and Yan Lu*, In Situ Synthesis of Catalytic Active Au Nanoparticles onto Gibbsite-Polydopamine Core-Shell Nanoplates, *Langmuir*, **2015**, *31*, 9483-9491.

# Acknowledgments

First of all, I would like to thank Prof. Matthias Ballauff and Prof. Yan Lu for their supervision on the whole process of my PhD research and the writing of this dissertation. I may say, without their instructions, advices and revisions, this PhD thesis would not have been finished. I also appreciate the freedom and space they have given to me. I will cherish for my whole life their understanding, support, and encouragement during my stay at the Helmholtz-Zentrum Berlin für Materialien und Energie (HZB). I am indebted to Dr. Zdravko Kochovski for his assistance and cooperation on the structural research done with Electron Tomography (ET). He spent a lot of time on instructing me for the measurment of ET and the reconstruction of my samples.

I have enjoyed a lot by working with all the members of the colloidal group at this institute. I will not forget the cooperation with Prof. Joachim Dzubiella, Dr. Rafael Roa and Dr. Charl Jafta. Many thanks for their great effort on my project.

I am very grateful to many people who help me during my PhD study at HZB. Special thanks from me should be given to the secretary Ms. Estrella Macarro for her constant support in many aspects related to the administration of the institute. I would like to thank my friends Mr. He Jia, Jie Cao, Martin Kärgell, Daniel Boseld, Andreass Ott, Miss Fangfang Chu, Sasa Gu, Qidi Ran, Ting Quan of our institute for the help they offered to me and the funs they have shared with me.

I gratefully acknowledge Prof. Nicola Pinna, Kallol Ray, Oliver Seitz, Emil List-Kratochvil from Humboldt University of Berlin for their reviewing on this dissertation.

Finally, I take this opportunity to thank my parents and my sister in China for their long-term encouragement and supporting me whenever I have difficulties.

# Selbstständigkeitserklärung

Hiermit erkläre ich die vorliegende Arbeit selbst verfasst und nur unter Zuhilfenahme der angegebenen Hilfsmittel angefertigt zu haben.

Ferner erkläre ich, dass ich nicht anderweitig mit oder ohne Erfolg versucht habe, eine Dissertation einzureichen oder mich einer Doktorprüfung zu unterziehen.

Berlin, den 28.11.2016

Shilin Mei